Study of residual stress in a thin platinum layer by means of non-destructive x-ray diffraction

Axel Bollhöfer

Thesis submitted to the Faculty of Science
of the University of Cape Town in fulfilment of the
requirements for the M.Sc. degree in Physics

Department of Physics, University of Cape Town

3 July 1999

Abstract

Resistance thermometers are often made of thin, sputter-deposited platinum layers on a corundum substrate. Since such thermometers are usually exposed to extreme temperatures, residual *stress* is building up at the Pt-Al_2O_3 interface and can possibly damage the layer. Therefore, the stress in the layer is measured by means of non-destructive x-ray diffraction and evaluated by the frequently used "d-$\sin^2\psi$" method. The apparatus for the measurements was an Ω-goniometer with a Bragg-Brentano focussing beam arrangement and a position sensitive detector. X-ray fluorescence scans were also performed on the sample in order to gain information about its composition. Additionally a scanning-electron-microscope was used to investigate its microstructure. The crystallographic texture of the platinum was also examined by x-ray diffraction and displayed in pole figures.

Contents

1 Introduction

Every material can take a characteristic amount of stress, i.e. force per area, before it breaks. Therefore we can say: Stress is the key to failure of materials. It follows from this statement that stress measurements are becoming increasingly more important with the growing demands of technology. However the task of stress research is not only to predict the strength of a given tool or production part, it is also to change the strength of materials. The effective stress is always a superposition of the applied stress and the internal (residual) stress. A production part with an internal compressive stress parallel to an applied tensile stress for example, will not break when the applied stress reaches the tensile strength of the stress-free part. This shows that a controlled development of an internal stress state can alter the behaviour of materials significantly. Treatments for establishing a certain residual stress state are e.g. rolling [PREC88] and shot peening [KUSS87].

1.1 Applied stress and residual stress

To gain a clear idea of what the terms "applied stress" and "residual stress" mean we consider an elastically deformed metal bar in uniform tension. The "applied stress" is simply given by the applied force per unit area of cross section. If the external force is removed, the stress disappears, and the bar regains its initial dimensions. On the other hand there are certain operations performed on a metal part, which will leave it in a stressed condition even after all external forces have been removed. This stress, which persists in the absence of external force, is called "residual stress". Such a condition of residual stress can be produced by welding a cross bar into an open section as shown in Fig. 1.1.

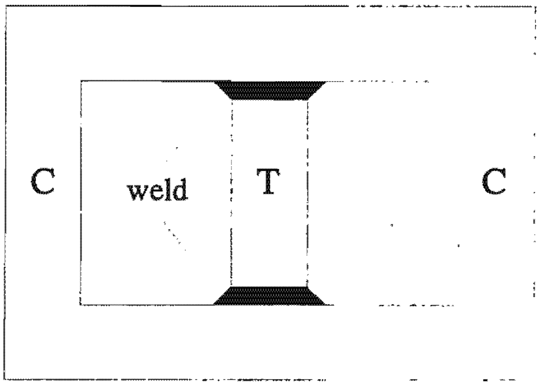

Fig. 1.1: Schematic example of residual stress redulting from temperature gradients during welding [CULL56]. T = tension, C = compression

In this hypothetical case, which does not take material properties into account, we can assume that, at the instant the second weld is completed, a substantial portion of the central bar is hot but that the two side members are far enough from the heated zone to be at a much lower temperature. On cooling, the central bar tries to contract thermally but is restrained by the side members. It does contract partially, but not as much as it would if it were not detached. The end result is that the side members are placed in compression and the central rod in tension when the whole assembly is at room temperature again. Residual stress is quite commonly found in welded structures.

Another mechanism that usually produces residual stress is plastic flow. If a beam is supported at two points and loaded with two equal forces F at its ends as shown in fig.1.2, plastic flow can occur at the top and bottom parts of the beam (shaded regions in fig.1.2). However the stress in the inner region of the beam is still below the elastic limit, and the beam is not plastically strained. Since the plastic flow releases some of the stress in the outer regions of the beam the stress distribution across the beam is no longer linear. After removing the external loads the internal forces try to straighten the beam. But because of its deformed top and bottom regions the beam straightens only partially and puts the top region into compression and the bottom region into tension. The stress distribution across the beam from top to bottom is now as follows: Compressive at the top, gradually changing to tensile in the region below which was not plastically strained, no stress in the middle at the neutral axis, compressive in the lower plastically unstrained region and tensile in the bottom region. The plastic flow in the two outer parts of the beam has changed the stress distribution in the whole. It is worth mentioning here that stress always changes gradually in any given direction. This follows from the stress equilibrium equations of the theory of elasticity [HAHN84] and can easily be seen in this example.

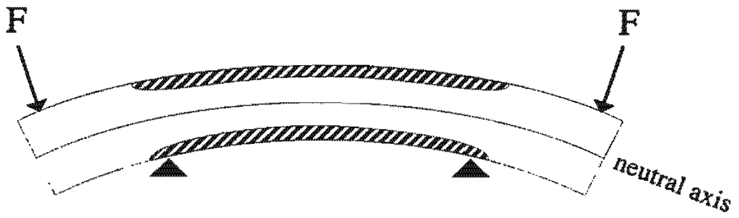

Fig.1.2: Plastic strain in a loaded beam

In a film-substrate system similar to the sample we are investigating here both of the reasons for residual stress mentioned above can occur. In our case we are dealing with a thin platinum film deposited on an aluminium oxide substrate. The system was annealed for 1 hour at 1200 °C. Since the coefficient of thermal expansion for platinum mismatches the coefficient for corundum (Al_2O_3), we expect that heating the sample creates stress. If this thermal stress exceeds the film's yield point, plastic flow will release some of the stress and the sample will remain in a stressed state after cooling down. Fig. 1.3 illustrates the process in greater detail.

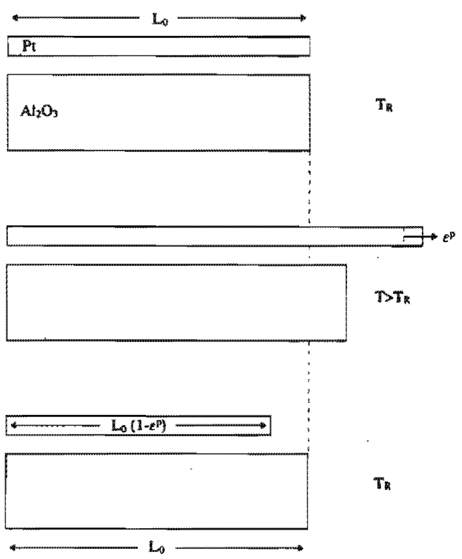

Fig. 1.3: Formation of "extrinsic" residual stress due to thermally induced plastic flow in a bilayer system

If we assume that the deposited Pt film and the substrate are of equal length (L_0) at room temperature (T_R), heating will develop compressive thermal stress in the film. (Because of the larger coefficient of thermal expansion for platinum, the film tries to expand, but is held back by the substrate.) Above a certain temperature this compressive stress in the film will exceed the yield point of the film, resulting in plastic strains (ε^P). If we now decrease the temperature back to the initial temperature, the film will try to attain an unconstrained length that is shorter than L_0 by an amount proportional to the plastic strain ε^P. The substrate, on the other hand, suffers no plastic flow and tries to attain L_0 at T_R. Consequently, at T_R the film will have tensile residual stresses proportional to ε^P. These stresses may also exceed the yield point and cause tensile plastic flow in the film. The final residual stress in the film at T_R will be proportional to the net plastic strain left in the film at the end of the thermal cycle. Nevertheless we can expect the stress to be tensile in the film, if plastic flow occurred during heating. According to [NOYA91] stresses caused by such, or similar, processes are generally called "extrinsic" residual stresses. All film stresses that form during the deposition process itself are classified as "intrinsic". Examples of these are the stresses that arise from epitaxial deposition of a thin, crystalline film on a substrate with a different lattice spacing. Since the x-ray diffraction method cannot distinguish between "extrinsic" and "intrinsic" residual stresses, we only measure the total internal stresses.

1.2 Mathematical description of stress

To describe a body in a certain stress state it is always necessary to deal with two quantities. One is the stress itself and the other one is the strain that is caused by the stress. Since stress is a force, one can not measure it directly. The only thing that can be measured is the effect of the force, i.e. the strain. Let us have a look at the strain first: Strain can be considered as two different types of deformation [NOYA87]. One is a deformation of the shape, called distortion and the other one is a change in dimension without a change in shape, termed dilatation.

However, in both types of deformation, any given point in the body changes its position. In order to obtain a mathematical description of the strain, let us consider the different mechanisms that cause a change in position:

The displacement of a point in a solid due to external loads is a combination of the deformation and rigid body translation and rotation as shown in fig.1.4 for two dimensions.

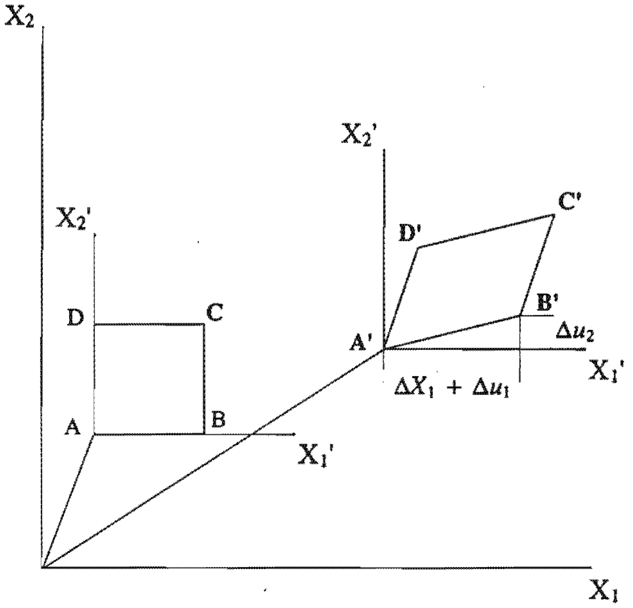

Fig.1.4: Displacement and deformation in two dimensions

The translational displacement can easily be eliminated by defining the local coordinate system X_1' X_2'. The total displacement of e.g. point B' is then given by

$$\Delta u_1 = \frac{\partial u_1}{\partial x_1}\Delta x_1 + \frac{\partial u_1}{\partial x_2}\Delta x_2 \tag{1.1}$$

along X_1' and

$$\Delta u_2 = \frac{\partial u_2}{\partial x_1}\Delta x_1 + \frac{\partial u_2}{\partial x_2}\Delta x_2 \tag{1.2}$$

along X_2'. The derivatives in equation (1.1) and (1.2) describe the variations of the displacement along the coordinate axis'. If we put the equations in matrix notation, it can easily be seen that the derivatives form a second rank tensor:

$$\begin{pmatrix}\Delta u_1\\ \Delta u_2\end{pmatrix} = \begin{pmatrix}\frac{\partial u_1}{\partial x_1} & \frac{\partial u_1}{\partial x_2}\\ \frac{\partial u_2}{\partial x_1} & \frac{\partial u_2}{\partial x_2}\end{pmatrix}\begin{pmatrix}\Delta x_1\\ \Delta x_2\end{pmatrix}$$

$$\begin{pmatrix}e_{11} & e_{12}\\ e_{21} & e_{22}\end{pmatrix} = \begin{pmatrix}\frac{\partial u_1}{\partial x_1} & \frac{\partial u_1}{\partial x_2}\\ \frac{\partial u_2}{\partial x_1} & \frac{\partial u_2}{\partial x_2}\end{pmatrix} \tag{1.3}$$

Unfortunately this definition of a deformation tensor still contains possible rigid body rotations. Considering that the rotational components of e_{ij} are antisymmetric a quantity $(e_{ij} + e_{ji})/2$ can be defined that will only contain components due to distortion since the rotational parts will cancel out. The strain at a particular point can then be written as a symmetric second rank tensor:

$$\varepsilon_{ij} = \begin{pmatrix}\varepsilon_{11} & \varepsilon_{12}\\ \varepsilon_{12} & \varepsilon_{22}\end{pmatrix} = \begin{pmatrix}e_{11} & \frac{1}{2}(e_{12}+e_{21})\\ \frac{1}{2}(e_{12}+e_{21}) & e_{22}\end{pmatrix} \tag{1.4}$$

The strain in three dimensions is obtained by a similar procedure and yields a similar second rank tensor:

$$\varepsilon_{ij} = \begin{pmatrix}\varepsilon_{11} & \varepsilon_{12} & \varepsilon_{13}\\ \varepsilon_{12} & \varepsilon_{22} & \varepsilon_{23}\\ \varepsilon_{13} & \varepsilon_{23} & \varepsilon_{33}\end{pmatrix} = \begin{pmatrix}e_{11} & \frac{1}{2}(e_{12}+e_{21}) & \frac{1}{2}(e_{13}+e_{31})\\ \frac{1}{2}(e_{21}+e_{12}) & e_{22} & \frac{1}{2}(e_{23}+e_{32})\\ \frac{1}{2}(e_{13}+e_{31}) & \frac{1}{2}(e_{23}+e_{32}) & e_{33}\end{pmatrix} \tag{1.5}$$

Or in short form, showing only the independent components:

$$\varepsilon_{ij} = \begin{pmatrix} \varepsilon_{11} & \varepsilon_{12} & \varepsilon_{13} \\ & \varepsilon_{22} & \varepsilon_{23} \\ & & \varepsilon_{33} \end{pmatrix} \tag{1.6}$$

The definition of the stress at a certain point is rather evident. Fig.1.5 shows the possible stress components that can act on the surface of an infinitesimal cube.

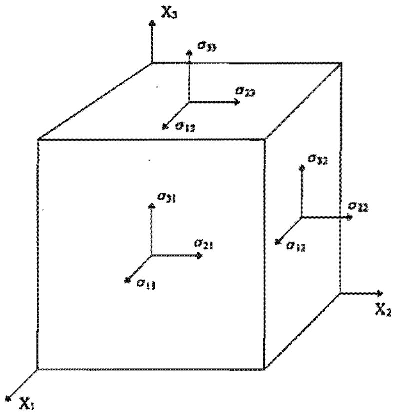

Fig.1.5: Stress components on an infinitesimal cube

Since the body is in static equilibrium, the stresses on mutually parallel surfaces will be equal in magnitude but opposite in sign. Thus the stress components on three faces of the cube are sufficient to describe the stress. Considering that the stress can be split in three components on each face we obtain nine different components:

$$\sigma_{ij} = \begin{pmatrix} \sigma_{11} & \sigma_{12} & \sigma_{13} \\ \sigma_{21} & \sigma_{22} & \sigma_{23} \\ \sigma_{31} & \sigma_{32} & \sigma_{33} \end{pmatrix} \tag{1.7}$$

Stress components with mixed indices are usually referred to as shear stresses and components with equal indices are called normal stresses. By convention the first index indicates the direction of the stress and the second index indicates on which face of the cube the component acts. Here the index of the face is given by its intersection with an axis of the reference system, i.e. the face that is parallel to the plane of the X_1 and X_2 axes, and intersects the X_3 axis, is face number three.

The theory of elasticity [HAHN84] derives equations from the static equilibrium of a body which show that the stress tensor is symmetric. Therefore only six components of the stress tensor are independent. We obtain, similar to the strain tensor:

$$\sigma_{ij} = \begin{pmatrix} \sigma_{11} & \sigma_{12} & \sigma_{13} \\ & \sigma_{22} & \sigma_{23} \\ & & \sigma_{33} \end{pmatrix} \tag{1.8}$$

The two second rank tensors are related by Hooke's law:

$$\varepsilon_{ij} = s_{ijkl}\,\sigma_{kl} \tag{1.9}$$

The s_{ijkl} are the elastic compliances of the crystal under consideration. They form a fourth rank tensor and describe the mechanical properties of the material. Its 81 components are not all independent, with the number of independent components decreasing with increasing crystal symmetry [Nye57]. For example they reduce to 3 independent components for a cubic crystal structure. Table 1.1 gives an overview of the number of independent components for different Bravais lattices. Very often polycrystalline solids can be regarded as isotropic if the crystallites are small compared to the examined volume. In this case the material can be characterized by only two mechanical quantities: Young's modulus E and Poisson's ratio ν.

Bravais lattice	**Number of independent elastic compliances**
triclinic	21
monoclinic	13
orthorhombic	9
tetragonal	6 or 7
trigonal	6 or 7
hexagonal	5
cubic	3
isotropic	2

Tab. 1.1: Overview of independent elastic components for various Bravais lattices [NYE57]

1.3 Measurement of residual stress by x-ray diffraction

When a polycrystalline piece of metal is deformed elastically in such a manner that the strain is uniform over relatively large distances, the lattice plane spacings in the grains change from their initial stress-free value to some new value corresponding to the magnitude of the applied stress. It is this strain of the lattice spacing that is measured by x-ray or neutron diffraction, in order to obtain the stress inside the material. Since neutrons have a large penetration depth compared to x-rays, neutron diffraction measurements are more suitable for the determination of stress deep inside the material, while x-ray diffraction is only capable of measuring stress close to the surface. This appears to be a disadvantage of the x-ray method, but it is in fact an advantage: Failure of a material is often caused by cracks that start at the surface and continue into the bulk of the material. Therefore the surface of a body is the more important part when it comes to the strengthening of materials. Furthermore, treatments such as rolling and shot peening create stress mainly in the outer parts of a solid and can leave the bulk in a stress free condition.

Polycrystalline materials can contain three different types of residual stresses [WOLF76a]. The first type is called "macrostress" and represents an average value of the local stresses in a volume that comprises many crystallites but is still small compared to the overall dimensions of the body (σ_I in Fig.1.6). The second and third types are usually combined in the term "microstress" due to their occurrence in much smaller regions. The second type (σ_{II} in Fig.1.6) is uniform inside one crystallite and given by its difference from the macrostress. In single phase materials its average over many grains must be zero [HOUT93]. The third type (σ_{III}) is a very small stress variation around lattice defects such as dislocations and point defects.

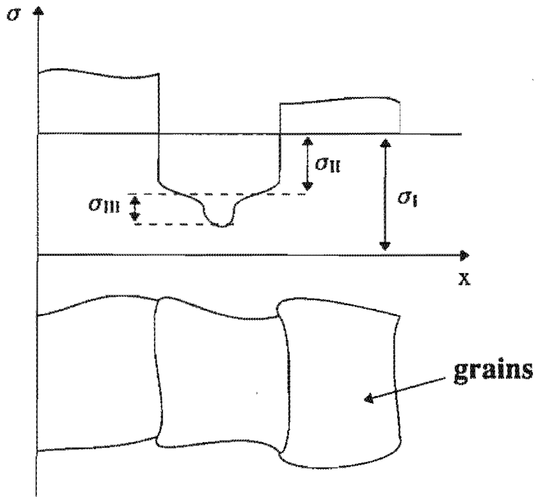

Fig.1.6: Different types of internal stress in a polycrystalline material

Microstresses and macrostresses influence the x-ray diffraction pattern in different ways. This can easily be seen from the basic law of x-ray diffraction; the Bragg-equation:

$$\lambda = 2d_{hkl} \cdot \sin\theta_{hkl} \tag{1.10}$$

λ stands for the wavelength of the x-rays, d_{hkl} is the spacing of the diffracting lattice planes given by their Miller indices (hkl) and θ_{hkl} is the corresponding angle under which constructive interference will occur. If e.g. a single crystal is under tensile stress all lattice planes with a perpendicular stress component will alter their spacings and become larger. Hence the Bragg-angle θ_{hkl} will become smaller for a given x-ray wavelength. In a polycrystalline material all grains diffracting x-rays in a certain direction have the same lattice plane orientation and therefore the same position with respect to the direction of the macrostress. Hence a similar effect can be observed: The diffraction peak is shifted to another Bragg-angle.

Microstresses on the other hand cause a broadening of the diffraction peak rather than a shift, because the stress varies from grain to grain. Therefore every grain or even part of a grain diffracts in a slightly different direction around the mean value of the Bragg-angle, resulting in a broader diffraction peak. We will not consider microstresses any further and will only deal with macrostresses in the following.

For the determination of the complete macro stress state, with all its components, it is necessary to measure the lattice plane spacings of grains with various crystallographic directions. In order to do that, the sample must take different orientations with respect to the incident x-ray beam. The orientation of the sample in the laboratory system can be described sufficiently by the angles ψ and φ as shown in Fig.1.7.

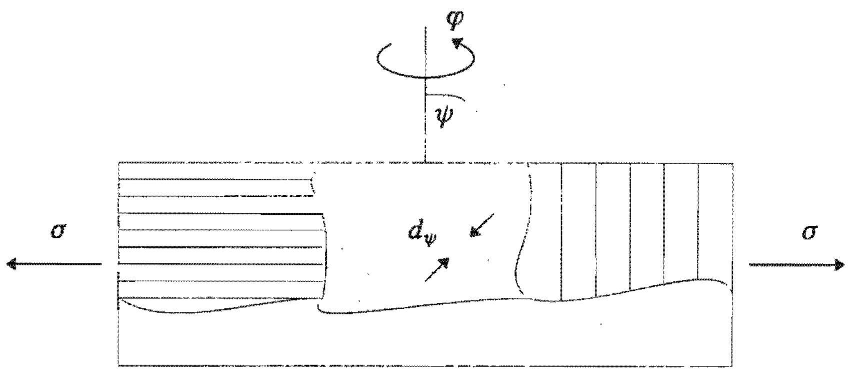

Fig.1.7: The angles ψ and φ describing the sample's grain and lattice plane orientation in diffracting position

These angles are actually the angles of rotation of the sample's reference system $\underline{S}_i$ relative to the reference system of the beam $\underline{L}_i$ as shown in fig.1.8.

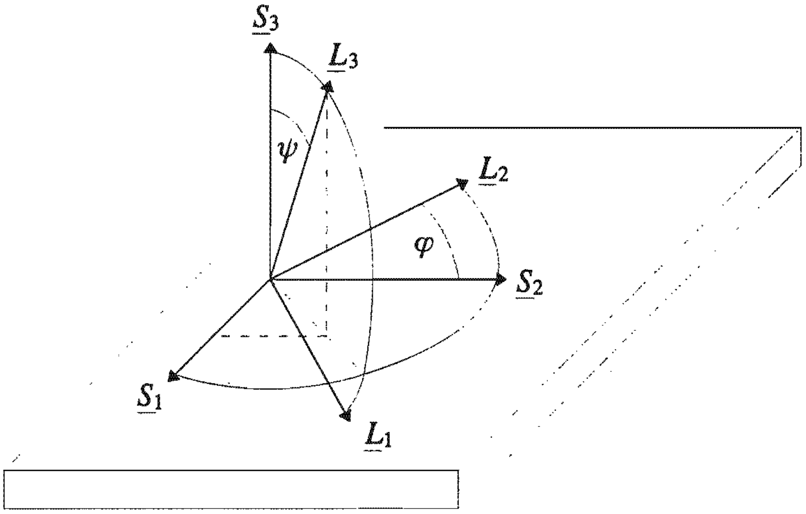

Fig.1.8: Definition of the angles φ and ψ and orientation of the laboratory system $\underline{L}_i$ with respect to the sample system $\underline{S}_i$

The sample reference system is defined by $\underline{S}_3$ normal to the sample's surface and $\underline{S}_1$ pointing in any direction, chosen according to the sample's shape or texture. The beam reference system is defined by the incident and diffracted beam in the $\underline{L}_1$-$\underline{L}_3$ plane with $\underline{L}_3$ parallel to the bisector between the two beams. Therefore $\underline{L}_3$ is also the normal to the diffracting {hkl} plane. ψ is then defined as the angle between $\underline{S}_3$ and $\underline{L}_3$ and describes the tilt of the sample while $\underline{S}_2$ and $\underline{L}_2$ include the angle φ which describes its rotation. By convention the $\underline{L}_2$ direction is always the axis of the ψ-tilt, so that it always remains in the $\underline{S}_1$-$\underline{S}_2$ plane.

The basic procedure for stress determination is to vary the angle ψ in a range $-\psi_{max} \ldots \psi_{max}$ and record the measured peak shifts along the θ-axis. By convention a negative ψ-tilt indicates a smaller inclination angle of the incident beam. The angle φ is kept constant for this series of measurements but further series may be measured at various φ angles. The lattice spacing d_{hkl} can then be calculated from the peak shifts by Bragg's law and the strain along $\underline{L}_3$ is obtained from the formula

$$\varepsilon_{33}^{L} = \frac{d_{hkl}(\psi, \varphi) - d_0}{d_0} \qquad (1.11)$$

where d_0 stands for the stress free lattice plane spacing. The superscript L indicates the laboratory reference system L_1, L_2, L_3. It should be mentioned here that the measured strain is not the elastic strain of a particular crystallite in the L_3 direction, but the average over many grains as seen by the x-rays.

The strain component ε_{33}^{L} can be expressed in terms of the strains ε_{kl}^{S} in the sample reference system by the tensor transformation

$$\varepsilon_{33}^{L} = a_{3k}\, a_{3l}\, \varepsilon_{kl}^{S} \tag{1.12}$$

where a_{3k} and a_{3l} are the direction cosines between L_3 and S_k, S_l respectively. The transformation matrix for this case is

$$a_{ij} = \begin{pmatrix} cos\varphi\, cos\psi & sin\varphi\, cos\psi & -sin\psi \\ -sin\varphi & cos\varphi & 0 \\ cos\varphi\, sin\psi & sin\varphi\, sin\psi & cos\psi \end{pmatrix} \tag{1.13}$$

Substitution of a_{3k} and a_{3l} in (1.12) yields

$$\begin{aligned} \varepsilon_{33}^{L} = {} & \varepsilon_{11}^{S}\, cos^2\varphi\, sin^2\psi + \varepsilon_{22}^{S}\, sin^2\varphi\, sin^2\psi + \varepsilon_{33}^{S}\, cos^2\psi \\ & + \frac{1}{2}\, \varepsilon_{12}^{S}\, sin2\varphi\, sin^2\psi + \frac{1}{2}\, \varepsilon_{13}^{S}\, cos\varphi\, sin2\psi + \frac{1}{2}\, \varepsilon_{23}^{S}\, sin\varphi\, sin2\psi \end{aligned} \tag{1.14}$$

We obtain an equation that puts the measured strains ε_{33}^{L} into relation with the elastic strain components in the sample's reference system. Since we are interested in the sample's internal stress, we need Hooke's law to link the measured data to the residual stress:

$$\varepsilon_{ij} = s_{ijkl}\, \sigma_{kl} \tag{1.9}$$

Unfortunately (1.9) can not directly be substituted in (1.14), because the elastic compliances s_{ijkl} are usually given in the reference system of the crystal's unit cell rather than the sample reference system. Therefore, it is necessary to perform a fourth rank tensor transformation for which we just show the ε_{11}^{S} component as an example :

$$\varepsilon_{11}^{S} = b_{1m}\, b_{1n}\, b_{ko}\, b_{lp}\, S_{mnop}\, \sigma_{kl}^{S} \tag{1.15}$$

The S_{mnop} are given in the coordinate system of the unit cell and the b_{ij} are the direction cosines between the unit cell axes of the measured grains and the sample reference system.

Substituting (1.15) in (1.14) makes equation (1.14) very unwieldy, but fortunately, if the solid under consideration is isotropic, Hooke's law becomes much more simple [DÖLL76, DIET73]:

$$\varepsilon_{ij} = \frac{1}{2} S_2(hkl)\, \sigma_{ij} + \delta_{ij} S_1(hkl)\, \sigma_{kk} \qquad (1.16)$$

The subscript k is a dummy index and implies summation over all k, and δ_{ij} is Kronecker's delta, which is defined as:

$$\delta_{ij} = \begin{cases} 1, & i = j \\ 0, & i \neq j \end{cases}$$

$S_1(hkl)$ and $\frac{1}{2} S_2(hkl)$ are the x-ray elastic constants. The reason why the x-ray elastic constants still depend on the lattice plane *hkl* although the body is considered as isotropic, is because the x-ray diffraction method is a microscopic method. This means that the x-rays are scattered at many crystallites in a favourable orientation for diffraction, but the properties of these crystallites are those of single crystals.

The value of $S_1(hkl)$ and $\frac{1}{2} S_2(hkl)$ for a given material can be determined in two ways: Experimentally, by x-ray measurements on a sample under varying applied stress [MACH58], or theoretically according to different models [HOUT93]. The experimental method needs a sophisticated diffractometer and a specially prepared test sample [MARI76]. The theoretical approach tries to calculate the x-ray elastic constants from the single crystal elastic compliances. In order to do this, it is necessary to make some assumptions that simplify the stress or strain distributions in the polycrystalline solid. The following assumptions are frequently used:

Reuss model [REUS29]:

σ_{ij} is homogeneous throughout the polycrystal. As a consequence, ε_{ij} is different in each grain because each crystallite has a different orientation with respect to the stress direction and therefore a different elastic behaviour according to the elastic compliances.

Voigt model [VOIG28]:

ε_{ij} is homogeneous throughout the polycrystal. σ_{ij} will now be heterogeneous, but the average stress can be defined as the macrostress.

Kröner model [KRÖN58]:

The Kröner model assumes that the stress and strain distributions are uniform inside every crystallite. For their calculation some further assumptions are necessary: Firstly, the crystallite under consideration is assumed to be spherical or ellipsoidal, and secondly all other grains are treated as if they were melted together in a "matrix" having homogeneous properties.

All these models give a more or less accurate result for the isotropic case, but fail to describe an anisotropic polycrystal, i.e. a material with crystallographic texture. In a heavyly textured material, equation (1.16) is still valid, but the x-ray elastic constants are functions of the angles φ and ψ. In this case an anisotropic elastic model should be used with a complete set of elastic constants which can either be measured on each test piece separately or calculated from the orientation distribution function (ODF) [BUNG89]. The ODF itself can be derived from various pole figures that show one characteristic feature of the texture at a time. The pole figures can be measured by means of x-ray diffraction, but it is a very time consuming task, because each figure is made up of numerous measured points.

The effect of a crystallographic texture can easily be seen if the standard method of processing x-ray data is used. This method is based on the following equation, obtained by substituting (1.16) and (1.11) in (1.14):

$$\begin{aligned}
\varepsilon_{33}^{L} = \frac{d_{hkl}(\psi,\varphi) - d_0}{d_0} &= \frac{1}{2} S_2(hkl)\ \{\sigma_{11}^{S} \cos^2\varphi + \frac{1}{2}\sigma_{12}^{S} \sin 2\varphi + \sigma_{22}^{S} \sin^2\varphi - \sigma_{33}^{S}\}\ \sin^2\psi \\
&+ \frac{1}{2} S_2(hkl)\ \sigma_{33}^{S} + S_1(hkl)\ \{\sigma_{11}^{S} + \sigma_{22}^{S} + \sigma_{33}^{S}\} \\
&+ \frac{1}{2} S_2(hkl)\ \{\frac{1}{2}\sigma_{13}^{S} \cos\varphi + \frac{1}{2}\sigma_{23}^{S} \sin\varphi\}\ \sin 2\psi \qquad (1.17)
\end{aligned}$$

Since the x-ray diffraction method only examines a very thin region close to the surface, the stress is usually assumed to be biaxial, i.e. all σ_{i3} components are zero. This is a reasonable assumption since a non-zero stress component in the $\underset{\sim}{S}_3$ direction at the surface would violate the stress equilibrium equations. Thus equation (1.17) reduces to

$$d_{hkl}(\psi,\varphi) = \frac{1}{2} S_2(hkl)\, d_0 \sigma^S_\varphi \sin^2\psi + S_1(hkl)\, d_0 \{\sigma^S_{11} + \sigma^S_{22}\} + d_0 \tag{1.18}$$

with

$$\sigma^S_\varphi = \sigma^S_{11} \cos^2\varphi + \sigma^S_{12} \sin 2\varphi + \sigma^S_{22} \sin^2\varphi \tag{1.19}$$

If $d_{hkl}(\psi)$ is plotted against $sin^2\psi$ a straight line with the slope $\frac{1}{2} S_2(hkl)\, d_0 \sigma^S_\varphi$ and intercept $d_0 \left[S_1(hkl)\{\sigma^S_{11} + \sigma^S_{22}\} + 1\right]$ should be obtained, provided that $\frac{1}{2} S_2(hkl)$ and σ^S_φ are constant. If several σ^S_φ were acquired from the slopes of different $d\text{-}sin^2\psi$ plots, say σ^S_φ, $\sigma^S_{\varphi+45°}$ and $\sigma^S_{\varphi+90°}$, the stress components σ^S_{11}, σ^S_{12} and σ^S_{22} can be calculated from (1.19). This is the classical "$d\text{-}sin^2\psi$" method as introduced by Macherauch and Müller [MACH61].

The problem that arises with this method is, that various effects can influence the linear behaviour of the $d\text{-}sin^2\psi$ plot. We have seen above, that the x-ray elastic constants can vary with φ and ψ in textured materials. The $d\text{-}sin^2\psi$ plot usually shows an oscillatory behaviour in this case, and the "$d\text{-}sin^2\psi$" method cannot be used anymore to calculate the internal stress components.

Another problem results from the penetration depth of the x-rays. Since a fair amount of the x-rays is not scattered at the sample's surface, but in the region below it, the diffracted x-rays always carry some information from a region where the stress is not necessarily biaxial. So the measured d_{hkl} is always the average of many lattice plane spacings within the penetration depth. If we look at equation (1.17), we can see that a non-zero σ_{33} component does not change much in the calculation. We still expect a linear behaviour for the $d\text{-}sin^2\psi$ plot, but the slope and intercept contain an additional σ_{33} term. Thus equation (1.19) changes to

$$\sigma^S_\varphi = \sigma^S_{11} \cos^2\varphi + \sigma^S_{12} \sin 2\varphi + \sigma^S_{22} \sin^2\varphi + \sigma^S_{33} \tag{1.20}$$

If σ^S_φ is measured for a sufficient number of φ-angles, σ^S_{11}, σ^S_{12}, σ^S_{22} and σ^S_{33} can still be calculated from (1.20). However, because the ψ-tilt changes the angle between the sample's surface and the incident beam the penetration depth of the x-rays varies with the ψ-tilt. The larger the beam-surface-angle, the larger the penetration depth. Therefore the diffracted beam for different ψ-angles does not contain information from identical regions. This can influence the linear behaviour of the $d\text{-}sin^2\psi$ plot, if the stress components are changing with depth. Fig.1.9c shows e.g. a $d\text{-}sin^2\psi$ plot with a negative σ^S_{33} gradient and a positive σ^S_{11} gradient. Especially the σ^S_{33} component is very likely to change from zero to a non-zero value in a short distance under the sample's surface. If the stress gradients are very small the $d\text{-}sin^2\psi$ plot might still show a straight line and their influence may be neglected, but if the graph shows a significant curvature, one should try to take the stress gradients into account. One approach is to describe the average stress components by their value at the surface and adding a term that describes their change with the depth z [DÖLL79]:

$$\langle\sigma_{ij}\rangle \cong \sigma_{ij}(z = 0) + \int_0^D e^{-\frac{z}{\tau}} g_{ij}(z)\, dz \tag{1.21}$$

D is the thickness of the sample and $g_{ij}(z)$ are the stress gradients with respect to the depth:

$$g_{ij}(z) = \frac{d}{dz}\sigma_{ij}(z) \tag{1.22}$$

The parameter τ stands for the penetration depth and therefore depends on the Bragg-angle θ, the ψ-tilt and the absorption coefficient μ of the material. For an Ω-goniometer τ becomes [EIGE95]:

$$\tau = \frac{sin^2\theta - sin^2\psi}{2\mu\, sin\theta\, cos\psi} \tag{1.23}$$

If we consider the stress components in (1.17) as the average values over the penetration depth, and measure the strain at $\varphi = 0$ with the assumption σ^S_{13}, $\sigma^S_{23} = 0$, we obtain

$$\begin{aligned}\langle\varepsilon^L_{33}\rangle = {} & \frac{1}{2}S_2(hkl)\ \{\langle\sigma^S_{11}\rangle + \langle\sigma^S_{33}\rangle\}\ sin^2\psi \\ & + \frac{1}{2}S_2(hkl)\ \langle\sigma^S_{33}\rangle + S_1(hkl)\ \{\langle\sigma^S_{11}\rangle + \langle\sigma^S_{22}\rangle + \langle\sigma^S_{33}\rangle\}\end{aligned} \tag{1.24}$$

This equation contains only the three normal stresses and one can try to guess functions which describe their general behaviour with the depth. After substituting (1.21) in (1.24) the parameters of these functions can then be varied to fit the measured strains.

So far all methods have assumed the shear components σ_{13}^S and σ_{23}^S to be zero in order to obtain a linear *d-sin²ψ* plot. If we look at equation (1.17) we can see, that in case of non-zero σ_{X3}^S shear components, the antisymmetric *sin2ψ*-term is non-vanishing. This causes a different behaviour for negative and positive values of the ψ-angle, an effect called "Ψ-splitting" (fig. 1.9d). Therefore the *d-sin²ψ* plot can not be used to determine the stress components. It is however possible to obtain two linear plots by adding and subtracting the measured strains for the positive and negative ψ-values as given by equation (1.17):

$$\begin{aligned}\varepsilon^+ &= \frac{1}{2}\left(\varepsilon_{33}^L(\psi^+) + \varepsilon_{33}^L(\psi^-)\right) = \frac{d_{hkl}(\psi^+,\varphi) + d_{hkl}(\psi^-,\varphi)}{2d_0} - 1 \\ &= \frac{1}{2}S_2(hkl)\ \{\sigma_{11}^S\cos^2\varphi + \sigma_{12}^S\sin 2\varphi + \sigma_{22}^S\sin^2\varphi + \sigma_{33}^S\}\ \sin^2\psi \\ &\quad + \frac{1}{2}S_2(hkl)\ \sigma_{33}^S + S_1(hkl)\ \{\sigma_{11}^S + \sigma_{22}^S + \sigma_{33}^S\} \qquad (1.25)\end{aligned}$$

$$\begin{aligned}\varepsilon^- &= \frac{1}{2}\left(\varepsilon_{33}^L(\psi^+) - \varepsilon_{33}^L(\psi^-)\right) = \frac{d_{hkl}(\psi^+,\varphi) - d_{hkl}(\psi^-,\varphi)}{2d_0} \\ &= \frac{1}{2}S_2(hkl)\ \{\sigma_{13}^S\cos\varphi + \sigma_{23}^S\sin\varphi\}\ \sin|2\psi| \qquad (1.26)\end{aligned}$$

The slope and intercept of a ε^+-*sin²ψ* plot yield the σ_{11}^S, σ_{22}^S, σ_{33}^S and σ_{12}^S stress components and the shear stresses σ_{13}^S and σ_{23}^S can be obtained from the slope of a ε^--*sin|2ψ|* plot.

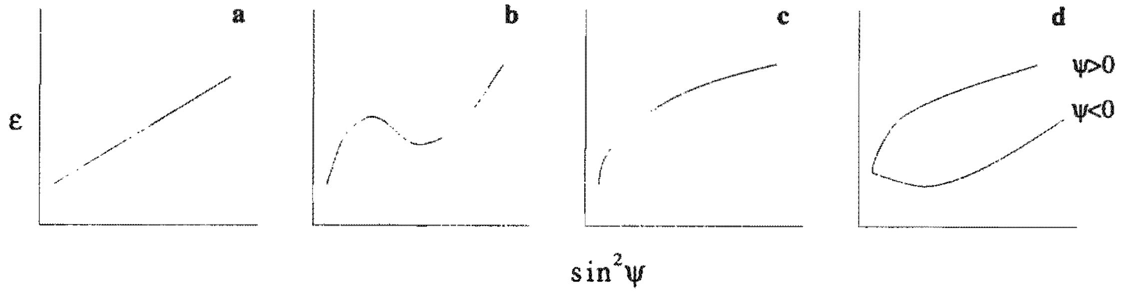

Fig.1.9: Types of *d-sin²ψ* plots commonly encountered in residual stress analysis from polycrystalline materials.
a) normal *d-sin²ψ* plot
b) textured sample
c) stress gradient within the penetration depth
d) ψ-splitting

In addition to the determination of internal stress with x-rays as described above there are two other methods for stress measurements which work on different principles [MACH87]:

Mechanical methods, i.e. measuring the dimensional changes that take place when parts of the material are removed, and methods which measure some physical property that depends on the internal stress (e.g. ultrasonic sound velocity). Each method has its own difficulties and are not discussed any further in the following.

2 Construction of the diffractometer

To detect the strains of lattice plains in different grains of a polycrystal under the same Bragg-angle, the sample must take various orientations with regard to the incident and reflected beams. This means that the tilt angle ψ between the normal component of the sample and the normal component of the reflecting plane must be changed. Furthermore, it is necessary to change the azimuthal φ angle of the sample in order to determine all components of the stress tensor. In the case of a fixed x-ray tube this means that at least a two circle goniometer is required even if the azimuth angle φ is not varied. One circle is needed for rotating the sample, and the other to position the detector. In general there are two different types of goniometer for x-ray stress measurements depending on the axis of the ψ tilt. In the case of the Ω-goniometer [FANI76] the axis of the ψ-tilt is parallel to the axis of rotation for the detector (fig. 2.1a). The other possibility is to rotate the sample around an axis perpendicular to the detector axis. Such a construction is called a Ψ-goniometer [WOLF76b] (fig. 2.1b).

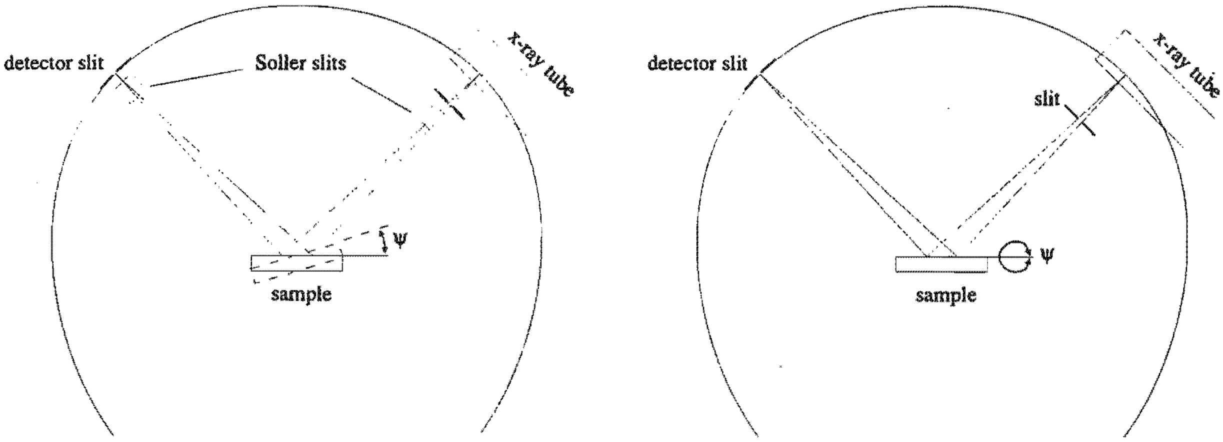

a) Ω-goniometer b) Ψ-goniometer

Fig. 2.1: The two basic types of stress diffractometers

The diffractometer unit used for this experiment is built in a more complicated way than necessary for this specific type of measurement. The reason for this is the use of the diffractometer for energy dispersive measurements and the determination of residual stress with depth resolution. Because of this multi purpose design the Ω-goniometer was chosen. The main disadvantage of this type of goniometer is that the angle ψ is limited by the Bragg-angle θ. Theoretically the highest ψ-angle is equal to the Bragg-angle with a tangential inclination between the x-ray beam and sample surface.

2.1 Path of the x-ray beam

The path of the x-ray beam is constructed according to the usual Bragg-Brentano principle [CULL56] with two focus points (Fig 2.2). In order to obtain a diffraction peak with a small width, it is necessary to place the detector at the second focus. Since the sample is the reflector and acts similar to a mirror in many ways, the focussing condition can be achieved by keeping equal distances between the sample and the detector and the sample and slit (4) which is positioned at the first focus. This distances were kept at 15 cm for all measurements taken. For detecting the diffracted x-rays a position sensitive detector was chosen which has the advantage of a relatively simple beampath. The usual method of taking stress measurements with a proportional counter would require a geometry with another slit system in the secondary beam path.

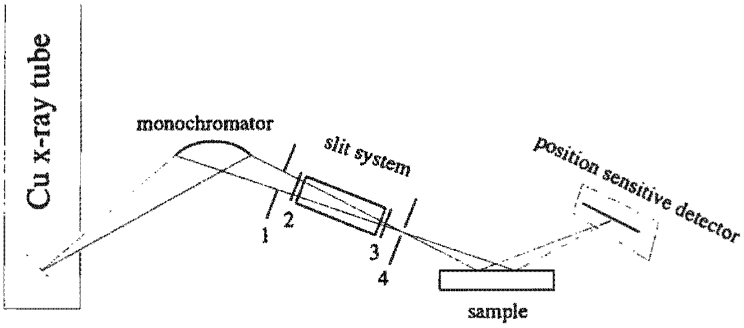

Fig. 2.2: Beam path of the parafocussing arrangement

The x-ray tube generates a line-shaped beam which leaves the tube housing with an angle of 6° between the beam and the normal of the tube housing. It enters the monochromator via an entrance slit that limits the horizontal divergence to 2° and is reflected at the para-focussing SiO_2 monochromator crystal. A second slit at the exit ensures that only the Kα radiation leaves the monochromator housing. The integrated slit system consists of a soller slit with two additional slits at each end to limit the vertical and horizontal divergence. The soller slit is 58 mm long and the distance between its vertically arranged sheets is 1 mm. Slits (2) and (3) limit the height of the beam to 8 mm and slits (1) and (4) confine the horizontal divergence of the beam. Slit (4) is adjusted to be at the focus point and is therefore closed to 0.15 mm. Slit (1) is kept open at 2 mm in order to maintain a high intensity. The shaped x-ray beam is then scattered at the sample and detected at the second focus point. All slit-shutters are made of tungsten and provide sufficient absorption for Cu Kα radiation.

2.2 Mechanical construction

The schematic construction of the diffractometer is shown in fig. 2.3. The heart of the apparatus is a two circle goniometer (1) that consists of two "Huber 410" single circle goniometers. The carrier for the sample is mounted onto the inner circle of the goniometer and consists of various parts: The x-y-table (2) on top of the inner circle provides a precise adjustment of the sample's surface into the axis of the goniometer. The z-stage (3) on top of the x-y-table adjusts the horizontal axis of the φ-goniometer (4) to the height of the x-ray beam. The sample itself is fixed onto another x-y-table (5) which is mounted onto the φ-goniometer. This x-y-table allows measurements to be made on different areas of the sample surface. All the above mentioned components are moved in the selection of the Bragg- and ψ-angles. For the possible use of the diffractometer for high resolution measurements a 150 cm long detector arm (6) is mounted onto the outer circle of the goniometer. At a distance of about 15 cm from the sample, the position sensitive detector (7) is fixed on the arm. All goniometers, x-y-tables and the z-stage are driven by stepper motors, controlled by a Huber SMC 9000 stepper motor control unit.

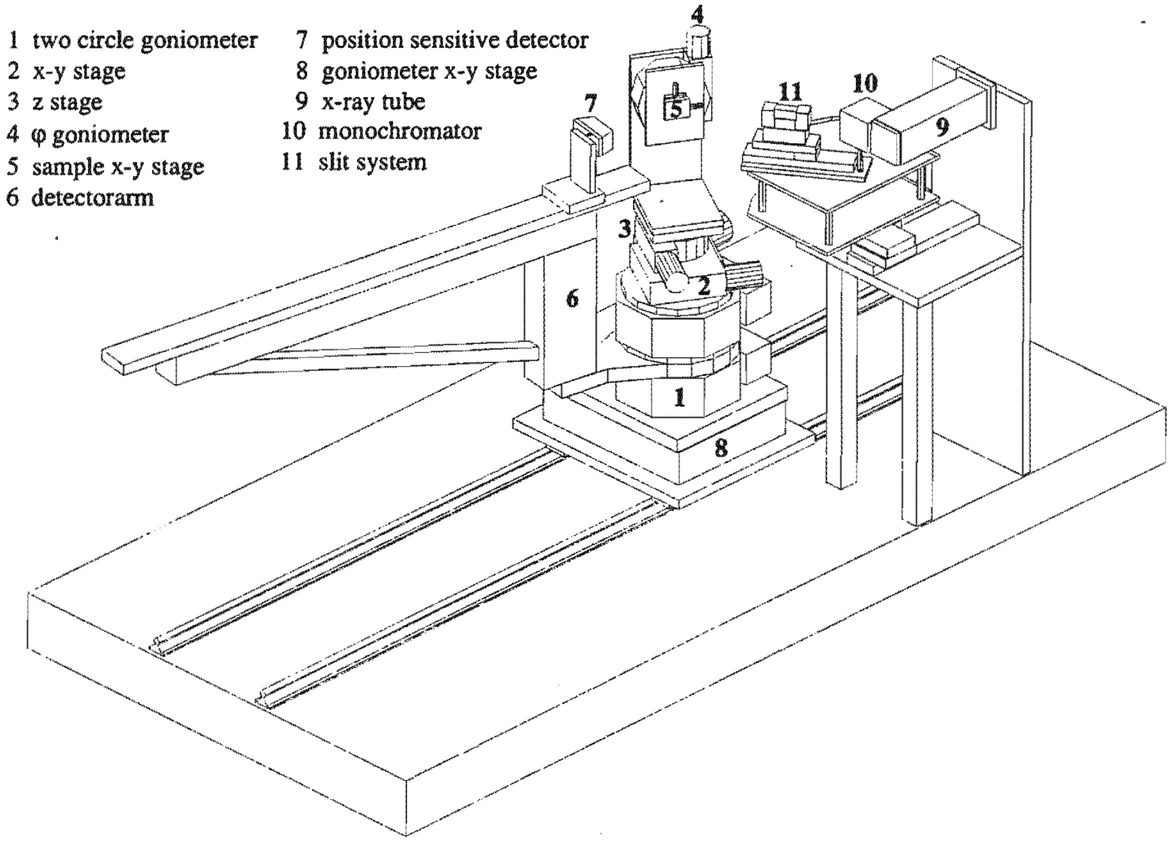

Fig. 2.3: Construction of the diffractometer

The whole goniometer assembly is mounted onto an x-y-table (8) in order to position the sample into the beam generated by the x-ray tube (9). With this x-y-table, it is also possible to vary the distance between the x-ray tube and the sample. To obtain a monochromatic beam, a focussing monochromator (10) is fitted onto the x-ray tube-housing. The concept of the diffractometer includes the possibility of taking measurements with a "white" x-ray-beam and an energy dispersive detector. In both cases a slit system (11) in the primary beam is necessary.

The carrier of the slit system is fixed to the the x-ray tube carrier and has numerous movable parts (fig. 2.4): The y-rail (1) carries the slit system (2) and provides the possibility to position the rear vertical slit into the focus of the monochromator. Because of reflection at the monochromator the monochromatic beam changes its direction with respect to the incoming "white" beam. For this reason the y-rail is mounted onto metal plate (3) and revolvable around an axis (4). If the axis (4) is adjusted precisely under the monochromator, one can easily turn the monochromatic beam into a "white" beam by removing the monochromator and turning the y-rail, with the slit system, into the new beam direction. To position the axis under the monochromator, the whole slit carrier assembly is situated on a x-y-table (5) which is built of crossed y-rails. For the vertical adjustment of the slits the metal plate (3) is based on four pillars (6) which allow the height of each corner to be altered individually. Both, goniometer and primary beam construction are mounted onto an optical bench and are placed in a shielded room.

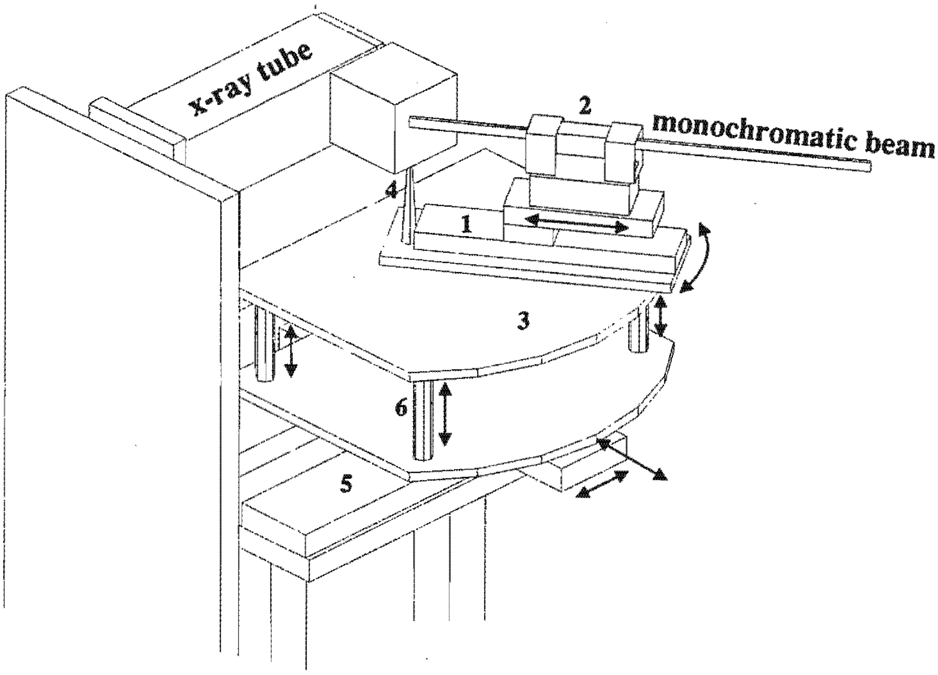

Fig. 2.4: Carrier for the x-ray tube and the primary slit system

2.3 Generation of the x-rays

The high voltage for the x-ray tube is generated by a Seifert ISO-DEBYFLEX 3000 generator. Fig. 2.5 shows the schematic of the x-ray generation system. The generator (1) supplies the x-ray tube with a maximum power of 3500 W. The voltage and current can be selected from the control panel (2) in a range up to 60 kV, in steps of 1 kV, and 80 mA, in steps of 1 mA, respectively. The copper x-ray tube (3) has various filters (V-, Mn-, Fe-, Ni-, Zr-filter and one sector open) and is connected to the control unit of the generator to operate the shutter. The output of the generator is connected to the x-ray tube by the high voltage cable (4). The cooling system is controlled by the control system (6), and the pipes (5) supply the high voltage generator and the x-ray tube housing with cooling water.

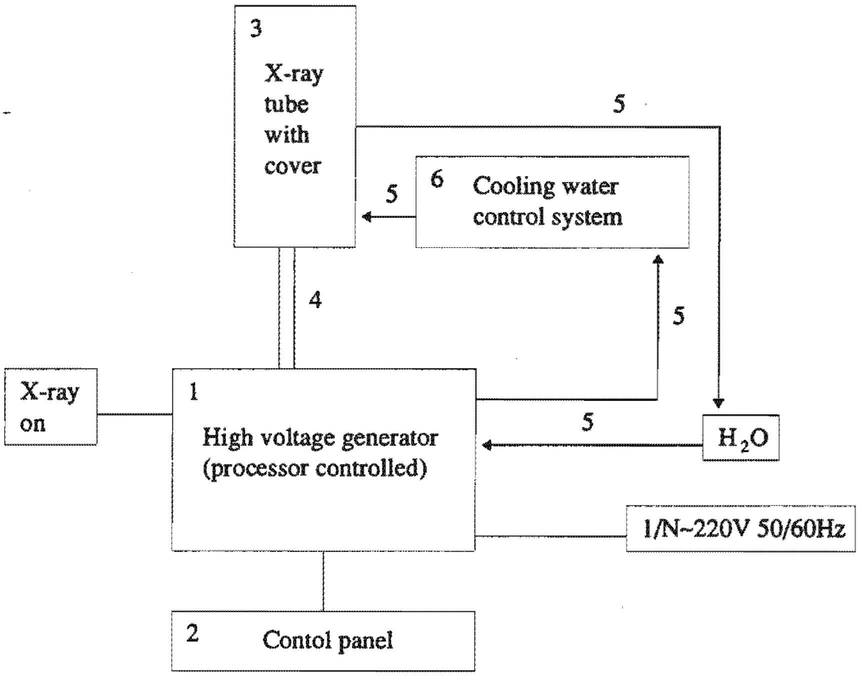

Fig. 2.5: schematic image of the x-ray generation system

2.4 Position sensitive detector

The scattered x-ray photons are measured with a position sensitive detector (PSD) made by Braun [BRAU]. In principle the PSD works like a classical proportional counter, except for the use of a wire (∅ 25.4 μm) with a high resistance (8 $k\Omega$/mm) as an anode. Because of the high resistance, the generated signals are not identical at the ends of the wire and information about the location of the ionizing photon can be obtained. Furthermore the PSD operates under high pressure (10-15 bar) to increase the probability of interaction between a photon and a gas molecule. The result is a higher resolution in the determination of the position. This position information is obtained by measuring and comparing the temporal delayed signals at the ends of the wire. Sophisticated electronic equipment is needed for such a purpose. Fig. 2.6 shows the construction diagram of the PSD including an integrated circuit diagram.

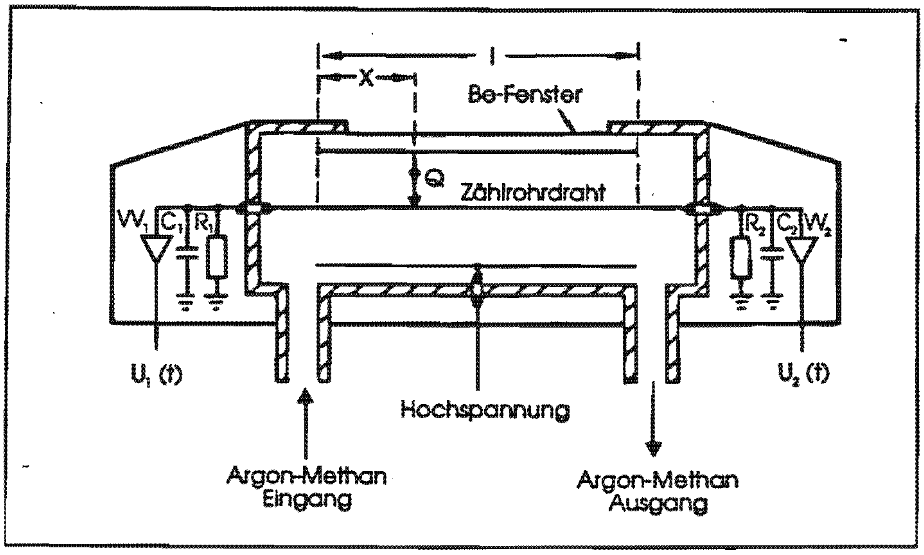

Fig. 2.6: Construction and circuit diagram of the PSD

An ionizing photon at position x generates a charge which flows evenly to both ends of the wire and loads the capacitors C_1 and C_2 ($U_c \sim 1 - e^{-(\tau_c/RC)}$). However the capacitor with the shorter distance to x will be charged earlier, because of the constant velocity of the charge carriers in the wire. Since the time difference is proportional to the position x the location information can easily be extracted. A current via the Resistors R_1 and R_2 discharges the capacitors afterwards ($U_d \sim e^{-(\tau_d/RC)}$, with $\tau_c < \tau_d$) and hence voltage peaks are generated. Both peaks are amplified by the built-in preamplifiers VV1 and VV2 and are further evaluated by the outer electronics according to fig. 2.7.

The amplifiers V1 and V2 have two functions. Obviously they further amplify the signals, but they also convert the peaks into zero crossing signals by derivation of the original peak-shape. The following dynamic compressors (DK) convert the weak zero crossings into a sharp edged signals to get a better time resolution and hence a higher position resolution. The newly shaped signals are then detected by the two zero crossing detectors (CK) which generate a fast logic pulse at the instant of the signals' zero crossing. Afterwards, the time-to-amplitude-converter (TAC) converts the time interval *dt* between the two pulses into an analogous voltage signal in the range from 0 to 10 Volts. Since the signal from the left branch t_l is always the start signal for the TAC, it is necessary to delay the signal from the right branch t_2 in order to prevent negative time intervals $dt = t_2 - t_1$ if the photon hits at the right half of the detector wire. Therefore the delay device (DELAY) adds a time t_v to t_2 $(t'_2 = t_2 + t_v)$ which is long enough to ensure that the signal from the left side reaches the TAC earlier. In order to obtain a digital value which can be processed by the multi channel analyser (MCA), an analogue to digital converter (ADC) finally converts the signal from the TAC into a value between 0 and 4096. The MCA stores the information in the appropriate channel from where a personal computer (PC) can read it.

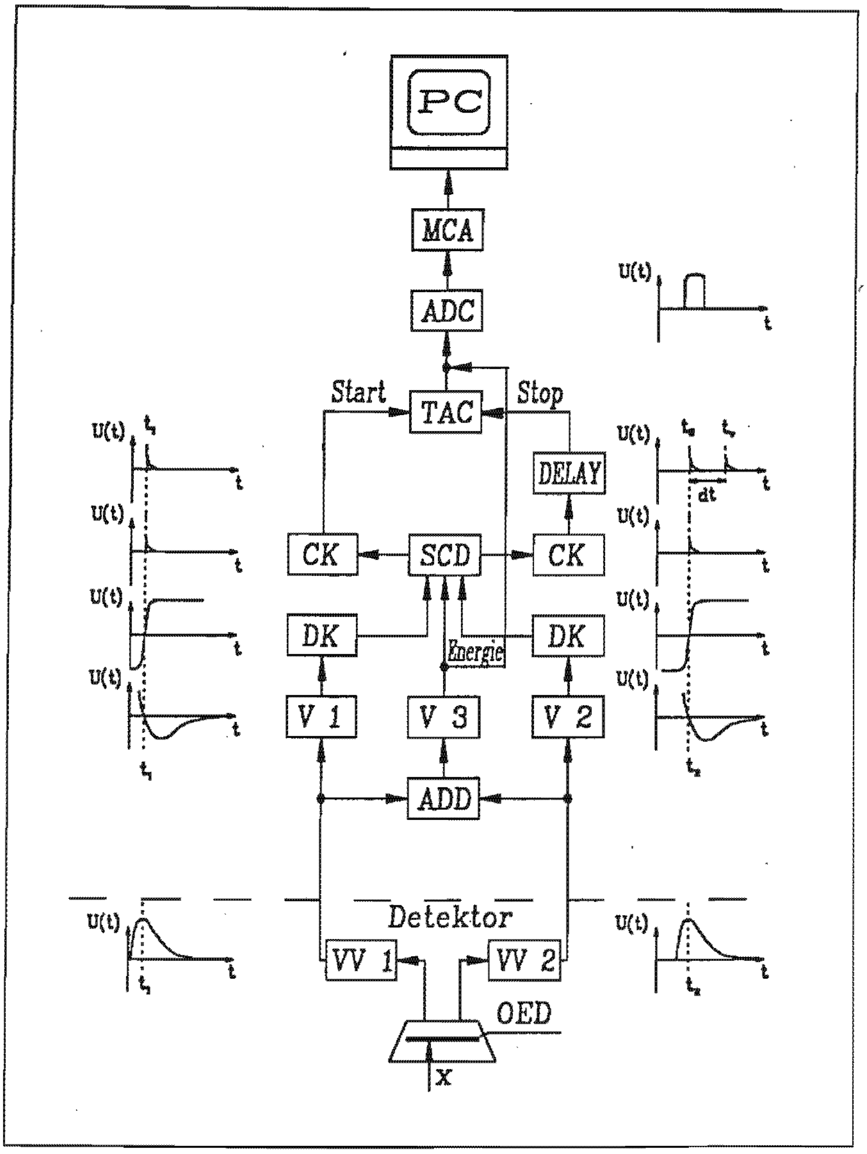

Fig. 2.7: Schematic image of the signal information processing

Besides the above described branches, providing position information, a third branch in the electronics deals with the energy of the incident photon. The two signals from the ends of the detector wire are added together (ADD) and the new signal is amplified afterwards by V3. Since this signal is directly proportional to the energy of the photon, it can be converted with the ADC and stored in the MCA if needed. The energy signal is also used for noise reduction in the position processing branches. The single-channel-discriminator (SCD) uses it as an input and sets a window for all incoming pulses. Pulses that are not in the required energy range are suppressed by a controlling signal from the SCD to the zero crossing detectors (CK) which do not generate a pulse at all without the appropriate signal from the SCD.

3 Adjustment

The precise adjustment of a stress diffractometer is very important. Measurements taken with a poorly adjusted diffractometer can cause systematic errors and imaginary stress states [FANI76,DOIG81]. For a complete adjustment, numerous adjustment steps are necessary. Tab. 3.1 lists all the steps and gives the aim of each step.

Adjustment step	Aim
Attaching and marking the sample	The mark on the sample's surface is used later to adjust the marked spot into the axis of the goniometer
Adjustment into the axis of the goniometer	1. Adjusting the mark into the horizontal φ-axis 2. Adjusting the mark into the vertical axis of the goniometer
Adjusting the monochromator	Maximum intensity and selection of the Cu-Kα radiation
Adjustment of the slit system	Shaping of the x-ray beam
Adjusting the sample into the x-ray beam	1. Sample's mark in the centre of the x-ray beam 2. Setting the zero position of the Bragg-angle circle (Sample's surface parallel to x-ray beam)
Adjusting the position sensitive detector	1. Equal distances between focus point and sample surface and detector-wire and sample surface 2. Calibrating the detectors zero position with respect to the multi channel analyser's mid position 3. Calibrating the detector's 2θ range with respect to the related channel number

Tab. 3.1: Adjustment steps and their aims

Before the adjustment steps are described in detail, a brief overview of the goniometer's adjustment facilities and their ranges is given.

3.1 The goniometer's adjustment facilities

The goniometer and the sample carrier have numerous possibilities for adjustments (chapter 2). Fig. 3.1 shows the schematic arrangement of all possible rotations and translations including their directions. With the two linear tables (1) and (2), the region of interest on the sample's surface can be adjusted into the horizontal axis of the φ-rotation. Therefore it is possible to measure any region on a flat sample without any further adjustments of the diffractometer. The x-y-table (4) is necessary to adjust the sample's surface into the axis of the goniometer. With the z-stage (3) the horizontal φ-axis can be adjusted to the primary beam-height. The whole goniometer-assembly, including the two-circle-goniometer (5), is mounted onto two linear-tables (6) and (7). These provide the possibilities of adjusting the sample surface into the primary beam and the variation of the distance between the surface and the slit system.

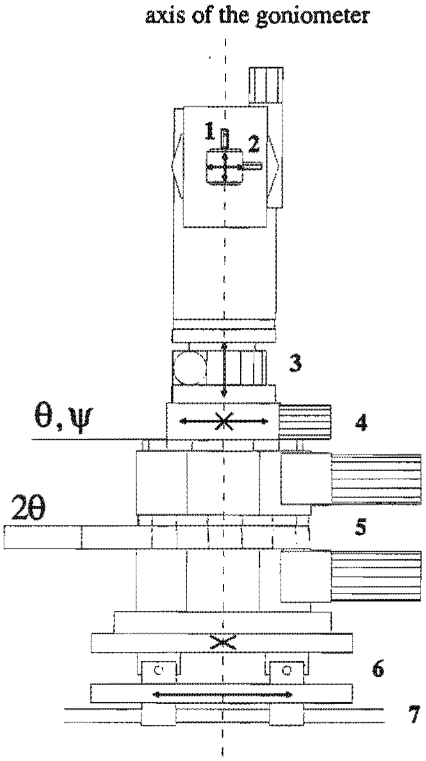

1 linear table (up-down)
2 linear table (left-right)
3 z-stage
4 x-y stage
5 two circle goniometer
6 linear table (front-back)
7 linear table (left-right)

Fig. 3.1: Schematic arrangement of all possible rotations and translations of the goniometer

The linear-tables (1) and (2) operate in a range of 20 mm with a precision of 0.01 mm. The z-stage (3) has a range of 40 mm and moves in steps of 0.005 mm. The x-y-table (4) operates in a range of 40 mm in both directions. The x-displacement ("left-right" movement with respect to the sample's surface) is carried out in steps of 0.005 mm, and a step in the y-direction ("front-back" movement) measures 0.001 mm. The two circles of the goniometer (5) are able to rotate 360° in steps of 0.0005°. The maximum displacement of table (6) is 16 cm and of table (7) 150 cm. Table (7) is driven by a rod with a thread and moves in steps of 0.005 mm. The precision of linear-table (6) is about 0.1 mm. All translations and rotations are controlled by stepper-motors except for tables (1), (2) and (6) which are operated manually.

3.2 Attaching the sample

Before the sample is attached to the linear table on top of the goniometer a mark (usually a cross) is drawn on the surface. This cross is used for adjusting exactly one spot on the sample's surface into the axis of the goniometer. Since drawn lines are too thick for a precise adjustment, the edges of the two crossed lines are used as a reference point as shown in fig. 3.2.

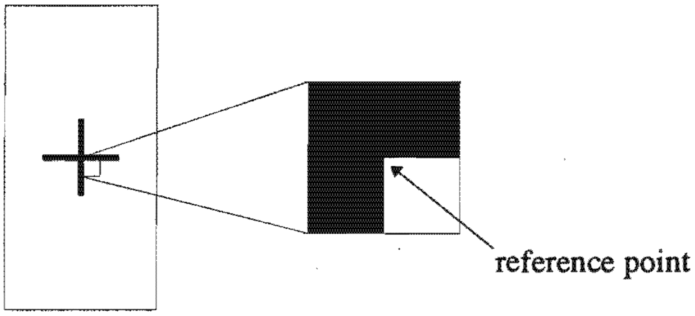

Fig. 3.2: Reference point on the sample's surface

3.3 Adjustment into the axis of the goniometer

The mark, or more precisely the mark's reference point, must be adjusted into the horizontal axis (φ-axis) and the vertical axis of rotation (goniometer axis). In order to do this, the mark is observed with a fixed microscope while rotating. The microscope has a crosshair which allows it to be aimed precisely at the reference point on the sample's surface. While rotating around the two axes any movement of the mark relative to the microscope's crosshair indicates a misalignment. It is possible to see displacements of 0.01 mm in the microscope which is more than sufficient for these alignments.

Alignment of the horizontal (φ) axis

If the sample is rotated around the φ-axis a displacement with respect to the crosshair can be seen if the mark is not exactly in the axis of rotation. With the help of linear tables (1) and (2) the mark is moved into the φ-axis until no displacement can be recognized during a 360° turn.

Alignment of the goniometer-axis

As described below a poor adjustment of the mark into the axis of the goniometer has a strong influence on the results [CONV92]. Hence this alignment should be carried out as precisely as possible. Because of the vertical axis of rotation the alignment of the mark with the goniometer axis is more difficult than the φ-axis-alignment. However, the same method used to adjust the φ-axis is still applicable. The sample is rotated ± 70° around the goniometer axis and the movements of the mark are observed in the microscope. There are two basic types of misalignment that can take effect (fig. 3.3) :

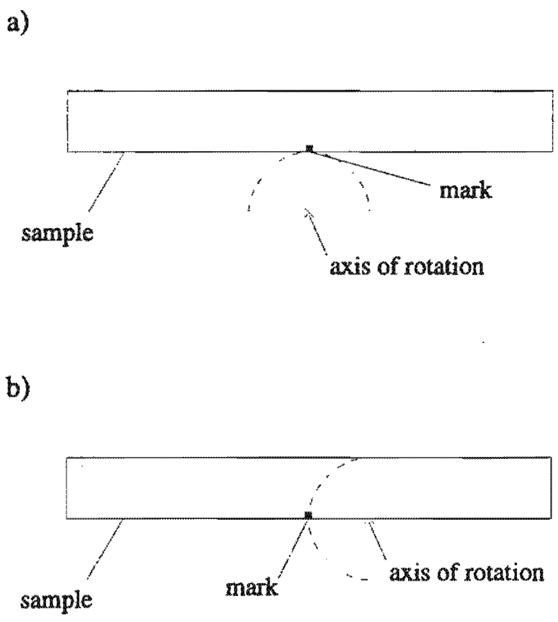

a) axis of rotation in front (behind) the mark on the sample's surface
b) axis of rotation to the side of the mark on the sample's surface

Fig. 3.3: Possible misalignments with respect to the axis of the goniometer

Tab. 3.2 lists all possible misalignment situations and their effect on the observed movements of the mark. The adjustment into the axis of the goniometer is carried out with the x-y-table (4) and according to tab. 3.2. The alignment is considered to be complete if no movement of the mark is observed during ± 70° turns. Because of the microscope's resolution of 0.01 mm the maximum misalignment of the mark with respect to the axis of the goniometer is 0.0152 mm.

Situation		Rotation	Movement of the mark
Surface behind the axis		↻ ↺	right left
Surface in front of axis		↻ ↺	left right
Mark on the right of axis		↻ ↺	left left
Mark on the left of axis		↻ ↺	right right

✦ Goniometer axis ▨ sample with mark

Tab. 3.2: Possible misalignments and their effects

This method of adjusting the diffractometer is related to the one described in [HÄRT95], i.e. the sample surface is directly adjusted into the axis of the goniometer.

A more common method of adjusting the sample into the axis of the goniometer is the semi-mechanical method [SERR88,MARI75]: A stress-free sample is used to measure the misalignment and to adjust the diffractometer. The adjustment is complete if the Bragg-angles of the stress-free sample differ less than 0.01° [HAUK82] from their theoretical values for various ψ-angles. Afterwards a reference rod is moved towards the sample until it touches the surface and the stress-free sample is replaced by the sample with the undetermined stress-state according to the position given by the reference rod.

3.4 Adjusting the monochromator

The adjustment of the monochromator is carried out according to the manufacturer's handbook [HUBE92]. Since this alignment has to be done only once it is not described in detail here.

3.5 Adjustment of the slit system

The aim of the slit system's adjustment is a shaped primary x-ray beam with maximum intensity. The adjustment is a consecutive method of closing the slits and correcting the slits' positions: At the beginning all slits are kept open while the y-rail (1) in fig. 2.4 is rotated around the rod (4), which is located under the monochromator crystal's centre, until an intense beam can be observed with a fluorescent screen behind the slit system. The vertical slits are then closed incrementally with the slit system being readjusted with the help of another possibility for fine tuning under the slit system. These steps are repeated until the second slit at the focus is closed to 0.15 mm and the first slit is closed to 1 mm. After the adjustment of the vertical slits the complete slit system is moved back and forth on the y-rail until the focus spot lies in the centre of the second slit. The horizontal slits are kept open at 8 mm.

3.6 Adjusting the axis of the goniometer into the x-ray beam

The method of adjusting the mark into the centre of the x-ray beam has some similarities to the principle described in [KLUG79]: The sample is rotated around the goniometer axis until it is approximately parallel to the x-ray beam. Then the linear-table (7) in fig. 3.1 moves the sample into the beam until the intensity measured with the position sensitive detector (which is also positioned in the primary beam-path) is half of the intensity without the sample in the beam-path. Afterwards, the sample is rotated slightly to positive and negative angles until the maximum intensity is reached. The sample's surface is now parallel to the primary beam. Next the sample is again moved into the beam until the measured intensity is only half of the value without the sample in the beampath. Now the sample is rotated 180° around the axis of the goniometer and the intensity measurement is repeated. An overlay of these two curves gives precise information about the goniometer's axis position with respect to the primary beam centre. Fig. 3.4 shows the three possible positions schematically and fig. 3.5 shows a measured curve of the misaligned and aligned sample. The linear table (7) is used to move the goniometer until its axis is exactly at the beam centre and we finally obtain a plot similar to the second picture in fig. 3.5.

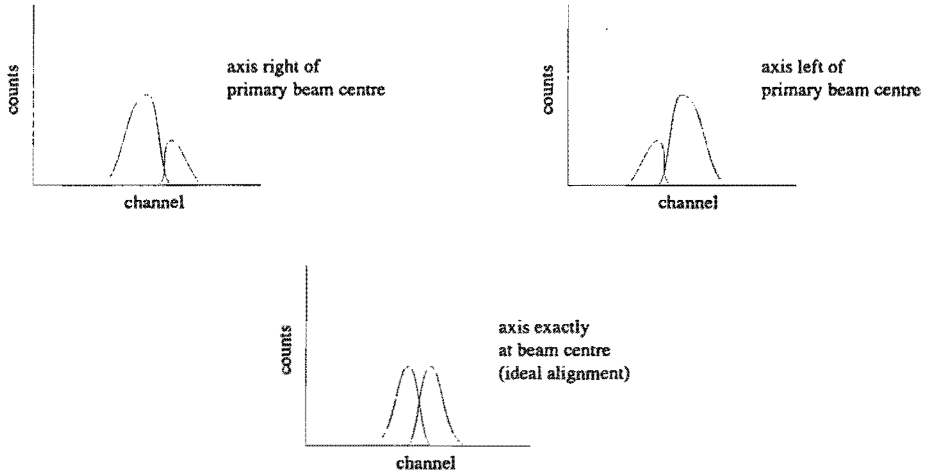

Fig. 3.4: Effects of misalignment of the goniometer-axis with respect to the primary beam as seen by the detector for 0° and 180° rotation

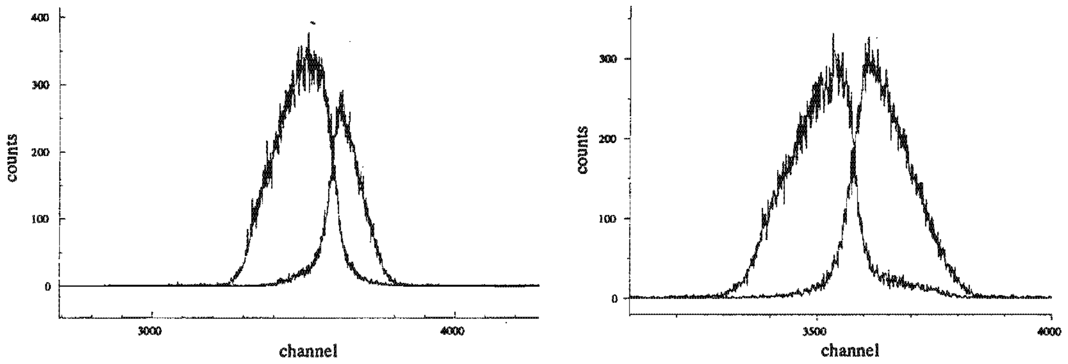

Fig. 3.5: Measured alignment curves of misaligned and adjusted goniometer-axis

3.7 Adjusting the position sensitive detector

The adjustment of the Position-Sensitive-Detector (PSD) requires three steps:

- First the distance from the detector to the sample's mark must be adjusted to the distance of the second slit (focus point) and the sample's mark: The distance between the focus point and the sample's mark is measured while the sample's surface is parallel to the beam path. Then the detector is brought in line with the sample and the beam path and a y-rail on top of the detector arm is used to move the PSD radially until it has the required distance to the sample's mark.
- Second the zero setting for the goniometer's 2θ scale must be related to a channel of the Multi-Channel-Analyzer (MCA). The crossing lines in fig. 3.5 are used to set the zero position: The detector is moved on the outer goniometer circle (2θ-circle) until the crossing point coincides with channel no. 4000. In this position the 2θ-circle is set to 0°.
- Finally the detector's 2θ-range must be related to the MCA's channel number. In order to do this, the position of a sharp diffraction peak is measured at different 2θ settings of the detector's position. Fig. 3.6 shows a graph of the goniometer's 2θ settings versus the peak position's channel number. The straight line in the plot is the best linear fit. Obviously there is some deviation from a perfect linear relationship. One reason for the deviations could be caused by a nonlinearity over the detector's range, but it is more likely that the goniometer's 2θ positioning is not precise enough. In any case the deviation is not really important, since the absolute peak-position is not crucial. For stress measurements we are only interested in the change of the peak-position for various ψ-tilts. The 2θ setting is therefore only changed if we switch to another peak. And concerning the

nonlinearity of the detector we can say, that the changes in the peak-position according to the ψ-tilts are small enough to assume a perfect linearity of the detector in this small range. From the slope of the best fit line, we can derive that one channel assimilates 0.001865°. Hence, to obtain the 2θ-angle from the channel number the channel-number-difference with respect to the zero channel (channel 4000) must be multiplied by 0.001865° and added or subtracted from the preselected 2θ-angle on the outer goniometer circle.

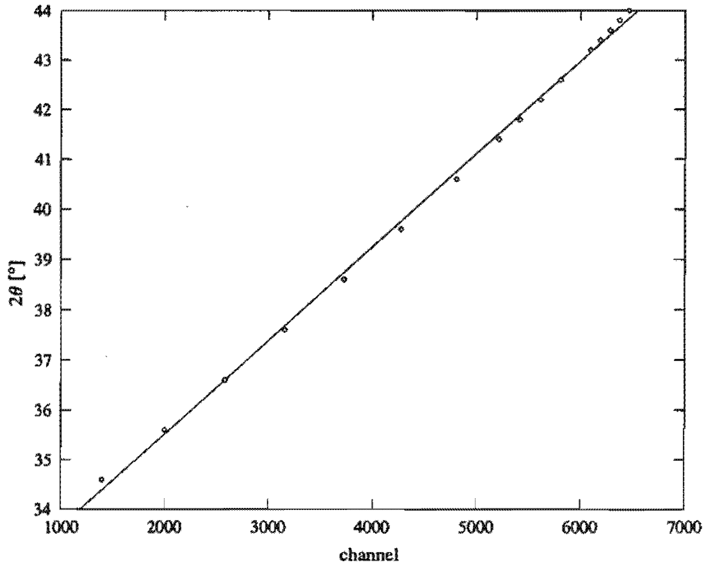

Fig. 3.6: Selected 2θ settings of the outer goniometer circle versus the peak-position's channel number. (The (111) peak was used for this calibration)

After all the above mentioned steps have been carried out, the diffractometer is fully adjusted. Analysis of misalignments shows that the misalignment of the sample's surface with respect to the axis of the goniometer and the misalignment of the axis with respect to the x-ray beam contribute most to a wrong determination of the peak position. The formula for calculating the deviation in the Bragg-angle caused by misalignment is given in [SERR88]:

$$\Delta\theta = \frac{\sin(\theta - \psi)\, e + \sin(2\theta)\, z}{2R \sin(\theta + \psi)} \tag{3.1}$$

θ is the Bragg-angle, ψ the tilting of the sample and R the distance between the detector and the axis of the goniometer. The parameter z is the displacement of the sample's surface with respect to the axis. A positive value of z indicates that the axis is located below the sample's surface. The other parameter e stands for the distance between the x-ray beam and the axis of the goniometer. Fig. 3.7 shows the definition of the two misalignment parameters.

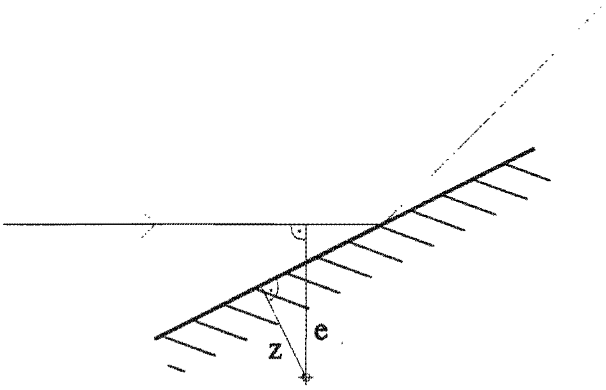

Fig. 3.7: Definition of the misalignment parameters e and z

The adjustment of the diffractometer is considered to be sufficient if $\Delta\theta$ obtained from equation (3.1) is smaller than the resolution for determining the peak-position. Otherwise the diffractometer must be adjusted again to avoid a wrong interpretation of the results.

4 Application of thin platinum layers

The main applications of thin platinum layers are in resistance thermometers. The physical principle of measuring temperature with thin metal layers is based on the change of the metal's electrical resistance with temperature. This method of measuring the temperature has the advantage of good accuracy over a wide temperature range. The most common metals used in resistance thermometers are platinum, copper and nickel, but platinum is superior to all other metals because of some advantages in its properties: E.g. the high melting point of platinum (2041.3 K [BEDF96]) provides a temperature range of -200°C to 1000°C for a typical device. For some metals this is very close to their melting point and it would therefore be difficult to build reliable thermometers for high temperatures with them. Another point is the very good linear behaviour of the electrical resistance within the required range of temperature which makes a conversion of the measured resistance into the actual temperature very simple. Furthermore the increase in resistance with temperature is better than for most metals which gives platinum thermometers a higher accuracy. Fig. 4.1 shows the electrical resistivity of some metals versus temperature.

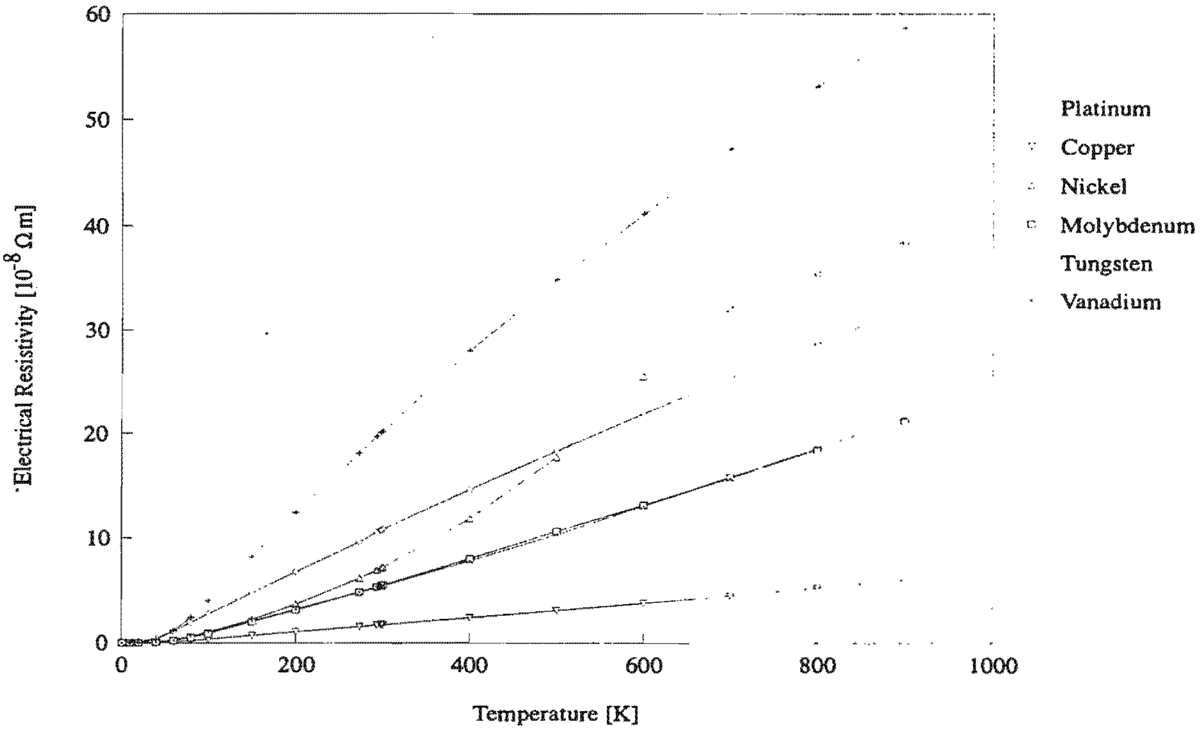

Fig. 4.1: The electrical resistivity of some metals versus temperature. (Data from [HAND94])

One can see that copper has the most linear behaviour, but the slope of roughly $5 \cdot 10^{-8}$ Ωm/ 700°K makes it difficult to obtain a high precision in temperature measurements. In this respect nickel has a much better slope, but its linearity is poor. Resistance thermometers based on nickel are only used up to 200°C. Vanadium provides the highest increase in resistance with temperature, but its linearity over a wide temperature range is also not good. So platinum with its very good linearity and its adequate slope is the optimal choice.

For most metals the relationship between the resistance R_T and the temperature T is very precisely described by

$$R_T = R_0(1 + \alpha T + \beta T^2). \tag{4.1}$$

R_0 is the resistance of the metal at 0°C. For platinum the constant β is sufficiently small to be neglected in the given temperature range for most purposes. The temperature coefficient α is defined by

$$\alpha = \frac{R_{100} - R_0}{R_0 \cdot 100°C} \tag{4.2}$$

with R_{100} as the resistance at 100°C. α is standardized in industrial norms and has a value of 0.003850/°C for the IEC 751 norm, and a value of 0.003916/°C for the Japanese JIS C 1604 norm.

For power saving reasons, and to keep self-heating errors as small as possible, the current through the resistance thermometer should be small. Hence, the resistance of the thermometer at a fixed temperature should be as high as possible. One can now see, that a thin sputtered platinum track has an advantage over a drawn wire. The smaller the cross section of the conducting material, the higher the resistance. This means that the conducting track can be much shorter than a wire with a larger cross section and therefore the device can be built in a more compact way. Fig. 4.2 shows the assembly of a platinum layer resistance thermometer. The sandwich-like structure provides a very good insensitivity to shocks and makes the manufacturing process very easy and cheap. The actual conducting platinum track is etched out of the platinum layer using lithographic methods. The use of lithography for making platinum tracks allows very fine tracks which can be arranged very densely. Hence a very long conducting track with a high resistance can be accommodated within a very small area. This compact and closed assembly allows another advantage of platinum thermometers to show: Their stability over a long period of time. Because of temperature shocks and constant use, the reproduction of the sensor-signals can suffer. Since platinum is chemically inert, and very pure platinum is used for resistance thermometers, it is the most stable temperature sensor. The typical deviation after 5 years is less then 0.04% at 200°C.

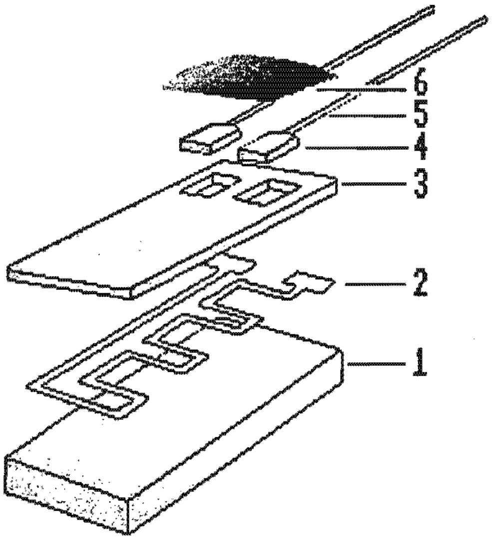

1 Al_2O_3 substrate
2 lithography structured platinum layer
3 covering glass layer
4 connecting pads
5 connecting wires
6 sealing ceramics

Fig. 4.2: Assembly of a platinum resistance thermometer

In order to measure a temperature with a resistance thermometer, one must apply the device in an electric circuit in which the resistance causes a potential difference that can be measured. There are basically two possibilities for this (fig. 4.3). In the first case a constant current flows through the resistance thermometer and the potential difference is measured directly along the device. The resistance is then easily obtained from the equation $V=R_T I_{const}$. The disadvantage of this method is the need of a constant current source. Much simpler is the use of a source with a constant voltage and a fixed resistor in series. The potential difference is still measured along the thermometer device, but the resistance is now calculated with $V=\frac{R_T}{R_T+R_{fix}} V_{const}$. The problem with this method is that the fixed resistor R_{fix} must not vary with the temperature and that its value must be known accurately. Therefore R_{fix} should always be kept at the same temperature.

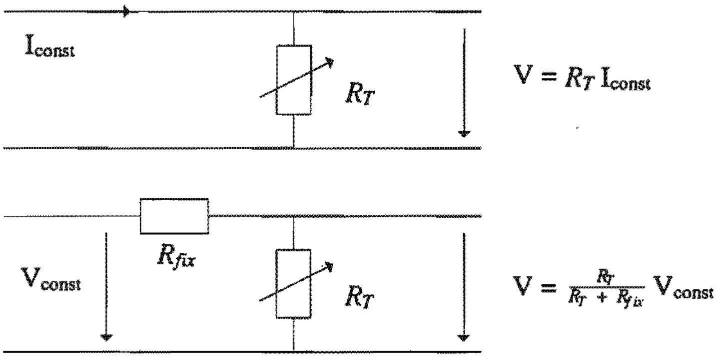

Fig. 4.3: Circuit diagrams for resistance thermometers

5 Characterization of the Pt-Al_2O_3 sample

The examined sample consists of a high purity platinum layer sputter-deposited on a 0.5 mm polycrystalline alumina substrate and subsequently annealed at elevated temperatures. As with all layered composites, in which the partners have vastly different physical and themal properties, the development of internal stresses during the processing is an important factor which affects the properties and stability of the system. Before commencing with the determination of the residual stress and texture in the Pt-layer, a characterizationof the sample is essential. Both, the platinum layer as well as the aluminum oxide have been characterized in terms of their composition (using XRF) and their microstructure (using SEM).

5.1 Platinum

Table 5.1 lists some of the physical properties of pure platinum. To be able to use these quantities for x-ray diffraction and stress analysis one must be sure that the platinum is indeed of high purity. Therefore an X-Ray-Fluorescence- (XRF-) scan was carried out in order to determine all the elements in the sample. Fig. 5.1-3 show three scans for different energy ranges.

Crystal structure	fcc
Lattice constant at 20 °C	3.9236 Å
Density at 20 °C	21460 kg/m^3
Elastic compliances:	
s_{11}	$7.53 \cdot 10^{-12}$ m^2/N
s_{44}	$13.1 \cdot 10^{-12}$ m^2/N
s_{12}	$-3.08 \cdot 10^{-12}$ m^2/N
Tensile strength of platinum wire	330 - 370 MPa
Young's modulus	$16.8 \cdot 10^{10}$ N/m^2
Poisson's ratio	0.377
Electrical resistivity at 20 °C	$10.5 \cdot 10^{-8}$ Ωm
Temperature coefficient of electrical resistance	0.003850 K^{-1}
Coefficient of linear expansion at 20 °C	$8.93 \cdot 10^{-6}$ K^{-1}
Melting point	1768.4 °C
Normal boiling point (at 1013.25 hPa)	3825 °C

Tab. 5.1: Physical properties of pure platinum
Data from [ARBL97], [HAND94] and [KAYE66]

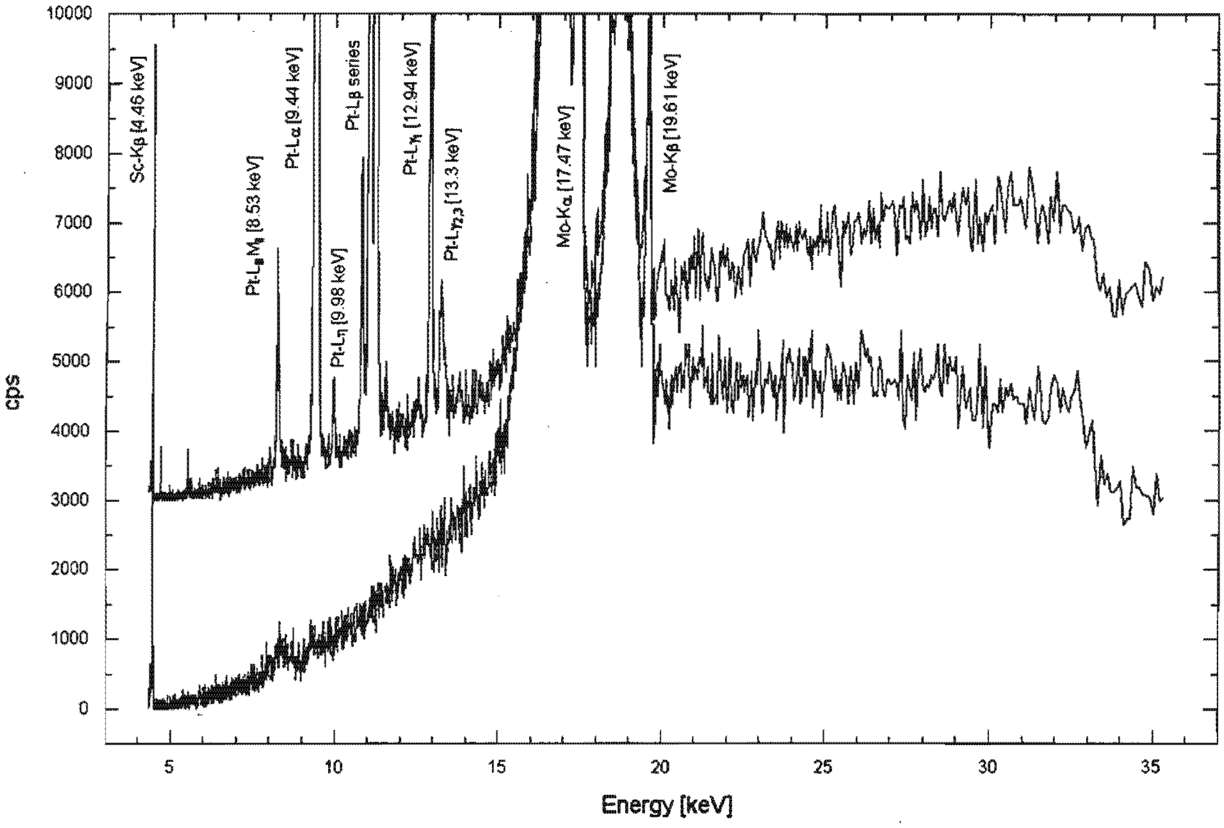

Fig. 5.1: XRF-scan of the platinum layer from 4 keV to 35 keV (upper graph shifted to 3000 cps for comparison)

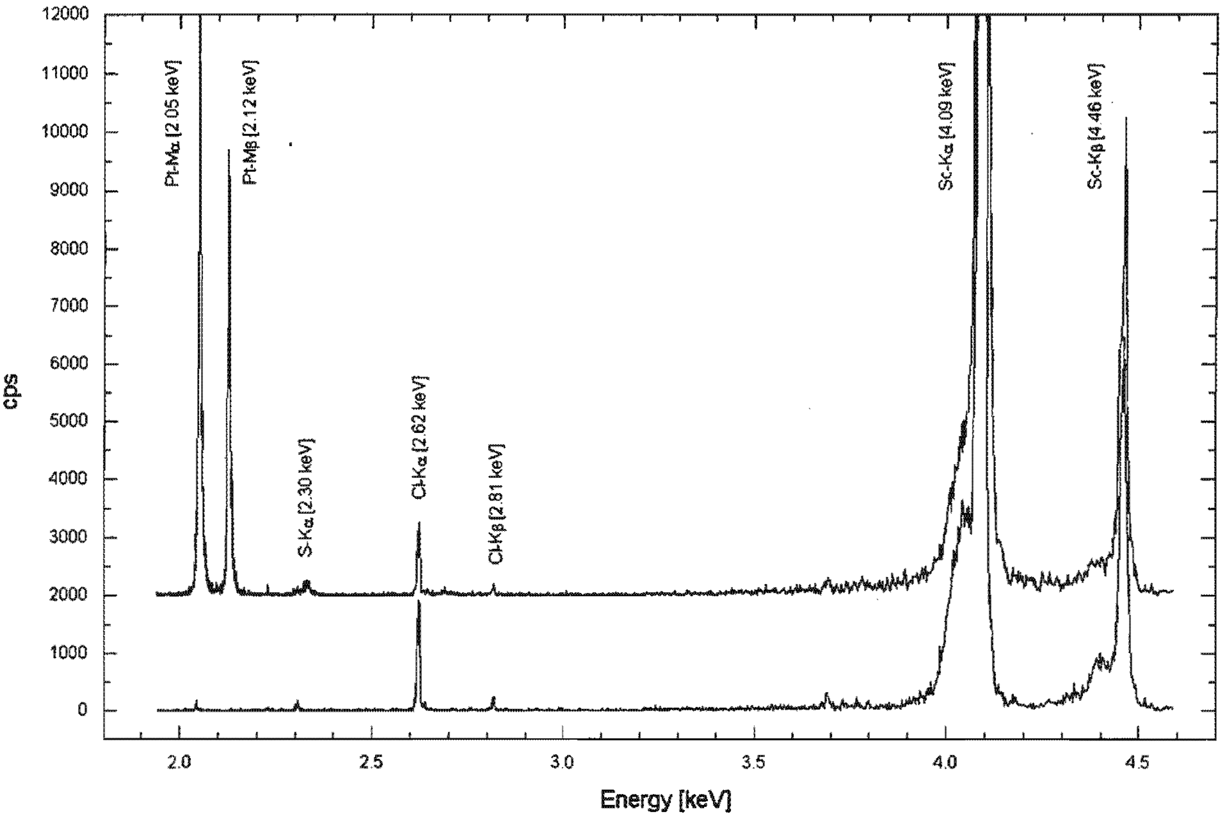

Fig. 5.2: XRF-scan of the platinum layer from 1.9 keV to 4.6 keV (upper graph shifted to 2000 cps for comparison)

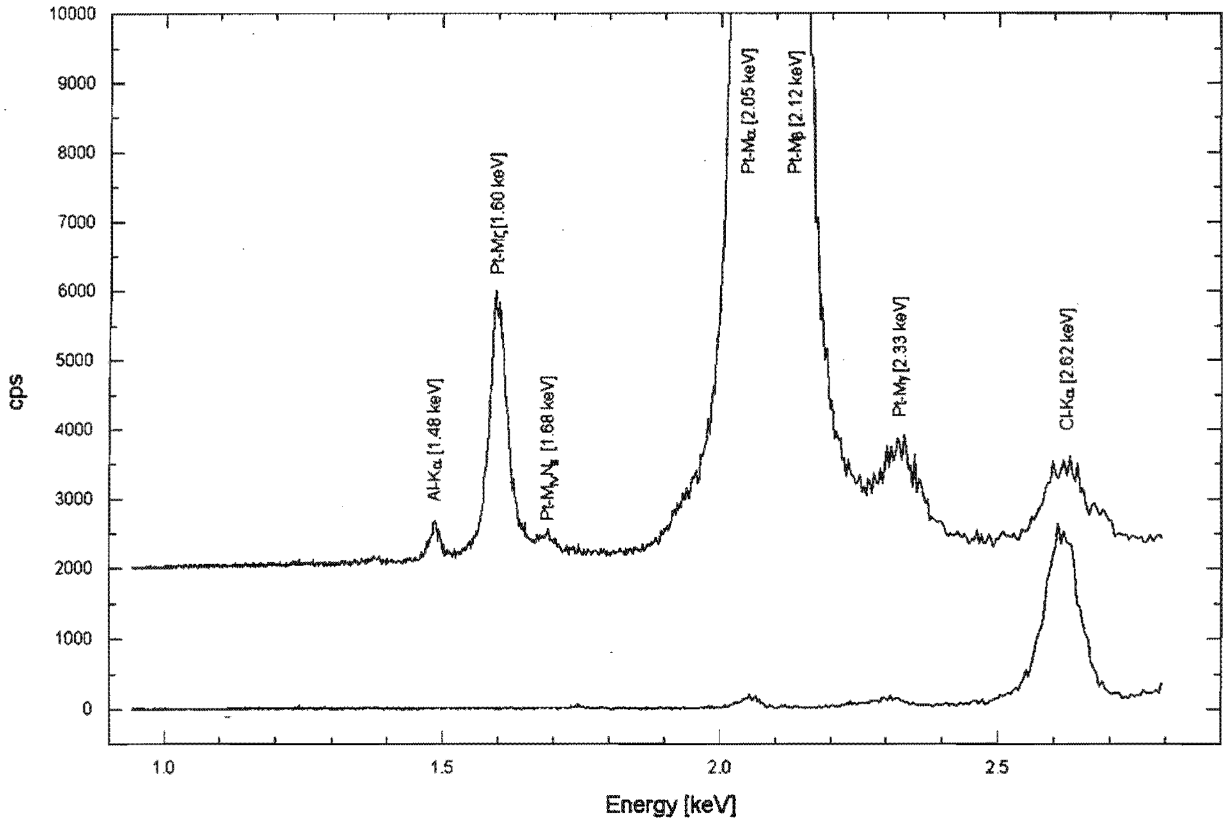

Fig. 5.3: XRF-scan from 1 keV to 2.7 keV (upper graph shifted to 2000 cps for comparison)

Each of the above plots contains two graphs. The upper graph corresponds to an XRF-scan of the platinum layer and the lower one to a reference scan of the sample holder. The second scan was necessary because the platinum sample was embedded in an epoxy resin for the measurement, and therefore the scans show some peaks that are not caused by the sample itself. For example the graphs show traces of chlorine and sulfur in fig. 5.2 and 5.3; two components of epoxy resin. Furthermore the x-ray-tube's target consisted of scandium and molybdenum which explains the rather strong scandium and molybdenum peaks in fig. 5.1 and 5.2. In addition, there is a small Kα aluminum peak at 1.48 keV in fig 5.3. This is probably aluminum radiation from the substrate passing through the platinum layer.

All other peaks in the graphs correspond to various platinum series. This shows clearly that the platinum in this layer is indeed of very high purity.

To gain some more information about the physical state of the platinum layer, the sample was studied with a scanning electron microscope (SEM). The aim was to determine the grain size and layer thickness.

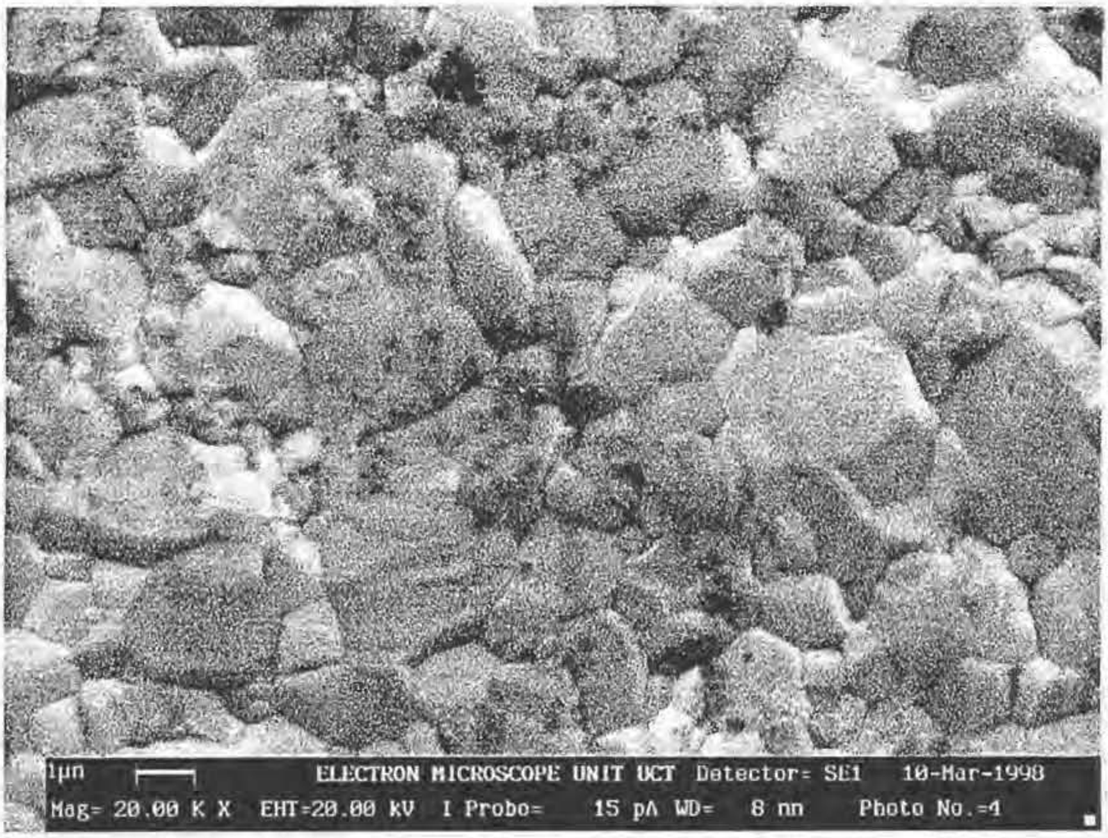

Fig. 5.4: SEM picture of the platinum surface (Magnification: 20000)

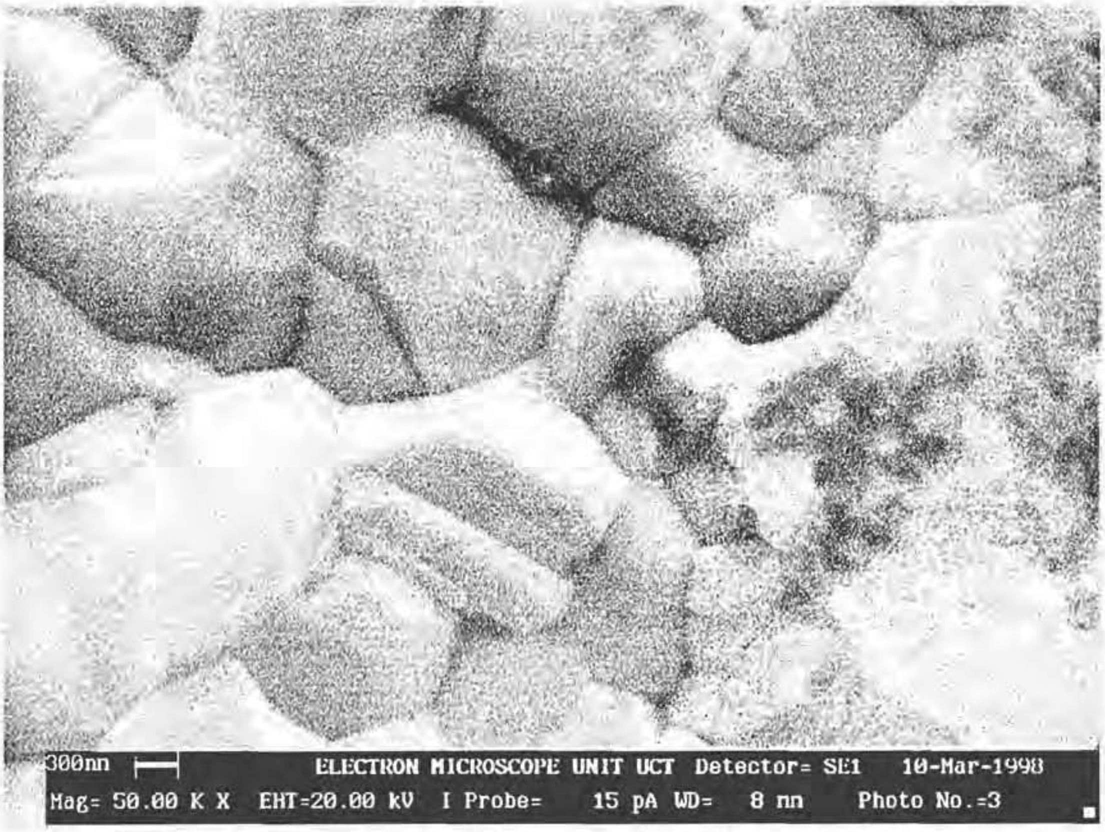

Fig. 5.5: SEM picture of the platinum surface (Magnification: 50000)

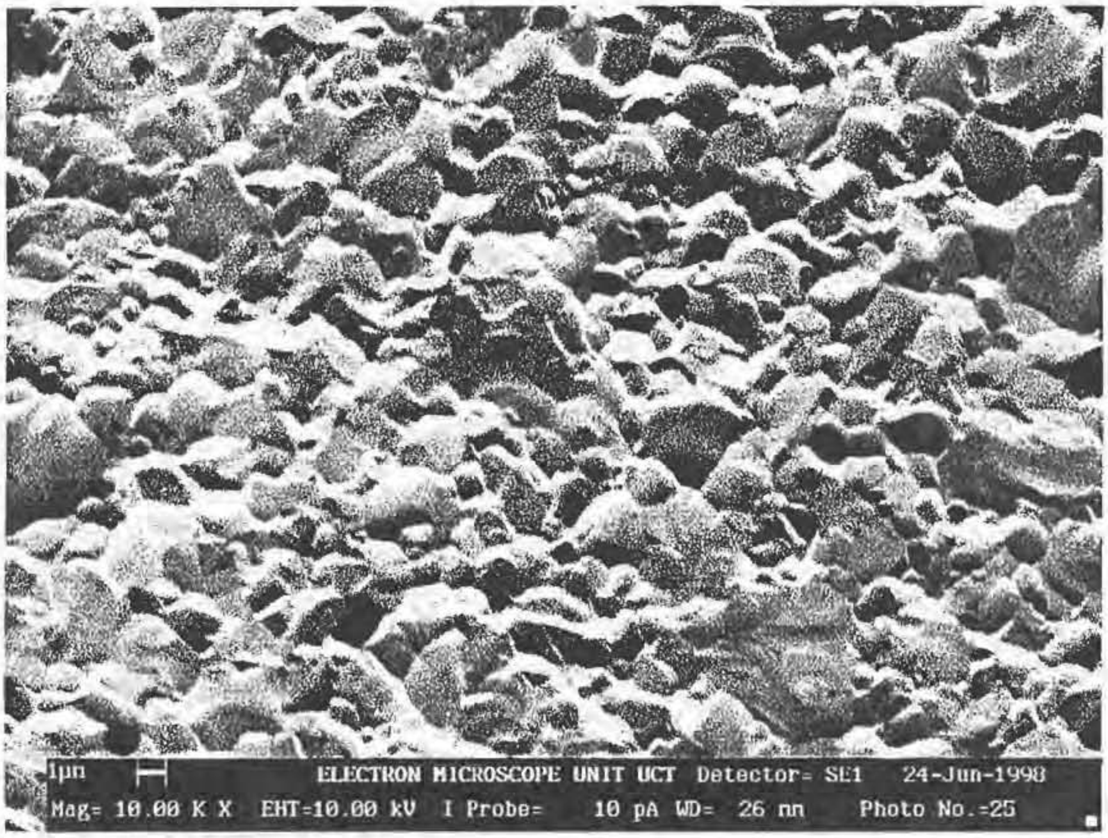

Fig. 5.6: SEM picture of the platinum layer under a viewing angle of approximately 45° (Magnification: 10000)

Fig. 5.7: SEM picture of the Pt-Al_2O_3 sample's cross-section (Magnification: 20000)

Fig. 5.4 and 5.5 show a top view of the platinum surface at two different magnifications. It can be seen, that the grain size varies over a wide range from approximately 0.5 µm to 5 µm. By counting all the grains in an area of 400 µm^2, the average length and width of a grain was found to be 1.7 µm. In a similar way the number of grains that are exposed to the shaped x-ray beam was calculated. With the settings of the slit system and the distances of focus point and sample-surface as given in chapter 3, the number of exposed grains was found to be approximately 4 million.

Fig. 5.6 shows a picture taken at about 45° relative to the sample's surface. At this inclination angle the topography of the surface can be observed. It appears to be remarkably rough with many grain edges and corners sticking out of the surface.

Finally fig. 5.7 shows an edge view of the sample. The bright platinum layer on top of the alumina bulk is easy to recognize. This picture shows, that the layer thickness varies only slightly about a mean value of approximately 1 µm. This is slightly more than the thickness given by the manufacturer, who measured the thickness according to the resistance of the layer. All data from the manufacturer about the examined sample are given in the following table:

Thickness of the Pt layer:	0.84 µm
Resistance:	104.0 m · Ohm
Sputtertime:	4 min 47 sec
Sputtervoltage:	3137 V
Sputtergas:	Xe/O_2
Annealing temperature:	1200° C
Annealing time:	1 h

Tab. 5.2: Manufacturer's data for the Pt-Al_2O_3 sample

5.2 Aluminium oxide

In order to obtain a complete characterization of the sample, an XRF-scan was performed on the alumina substrate as well. However, the scan was taken from the back of the Pt-Al_2O_3 sample and we must therefore be cautious about transferring the results to the front, where the platinum layer is covering the substrate. Not knowing the history of the alumina, we can only assume that it is homogeneous and that the back was not treated differently in any way from the coated surface. On the other hand such an assumption seems legitimate because the Al_2O_3 just serves as a substrate here.

As previously in section 5.1 we first give some physical properties of Al_2O_3 in table 5.2. The following figures (5.8-10) show the XRF-scans for the same energy ranges as the Pt-scans.

Crystal structure	rhombohedral
Axial angle	55° 17.36'
Lattice constant:	5.12863 Å
X-ray density	3986.9 kg/m^3
Elastic compliances:	
s_{11}	$2.90 \cdot 10^{-12}$ m^2/N
s_{33}	$1.94 \cdot 10^{-12}$ m^2/N
s_{44}	$5.78 \cdot 10^{-12}$ m^2/N
s_{12}	$-1.05 \cdot 10^{-12}$ m^2/N
s_{13}	$-0.38 \cdot 10^{-12}$ m^2/N
s_{14}	$-1.71 \cdot 10^{-12}$ m^2/N
Coefficient of linear expansion at 20 °C	$5.0\text{-}5.6 \cdot 10^{-6}$ K^{-1}
Melting point	2015 °C

Tab. 5.2: Physical properties of aluminum oxide

Data from [HAND94], [AMER72] and [KAYE66]

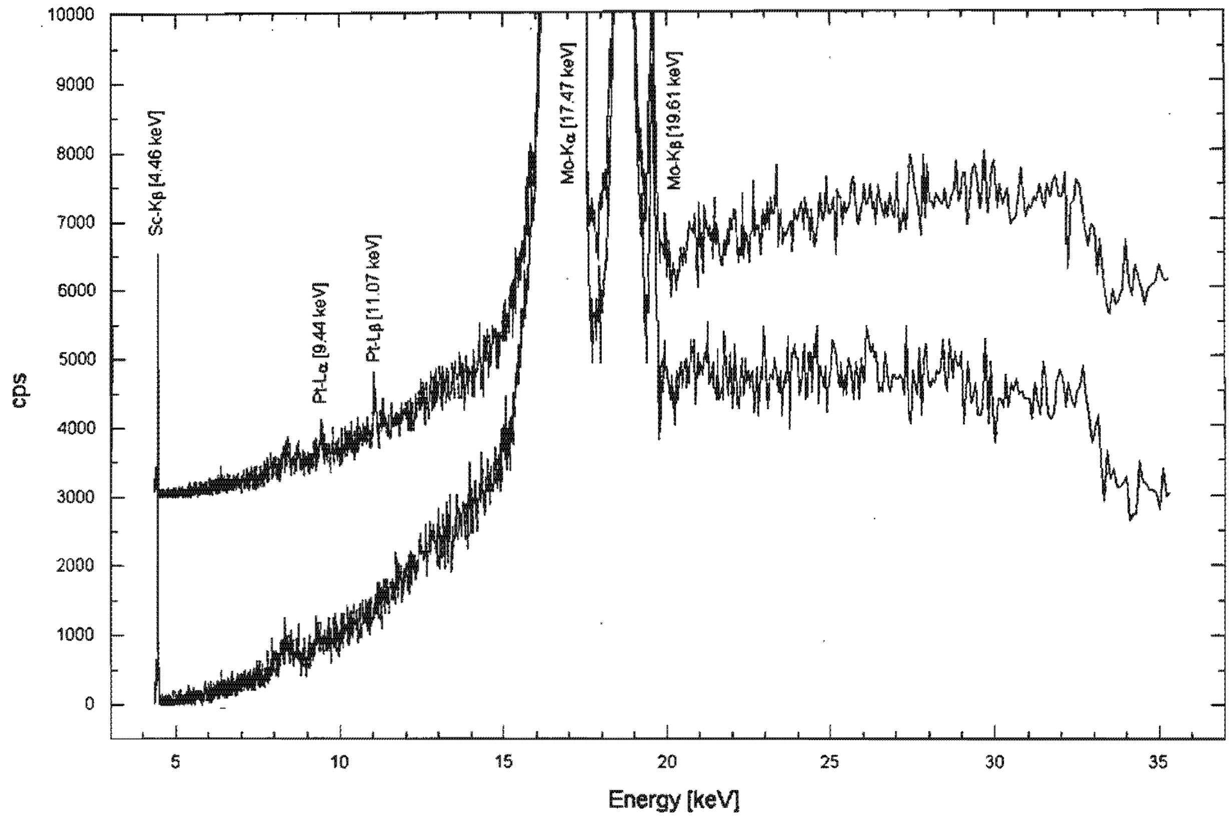

Fig. 5.8: XRF-scan of the alumina substrate from 4 keV to 35 keV (upper graph shifted to 3000 cps for comparison)

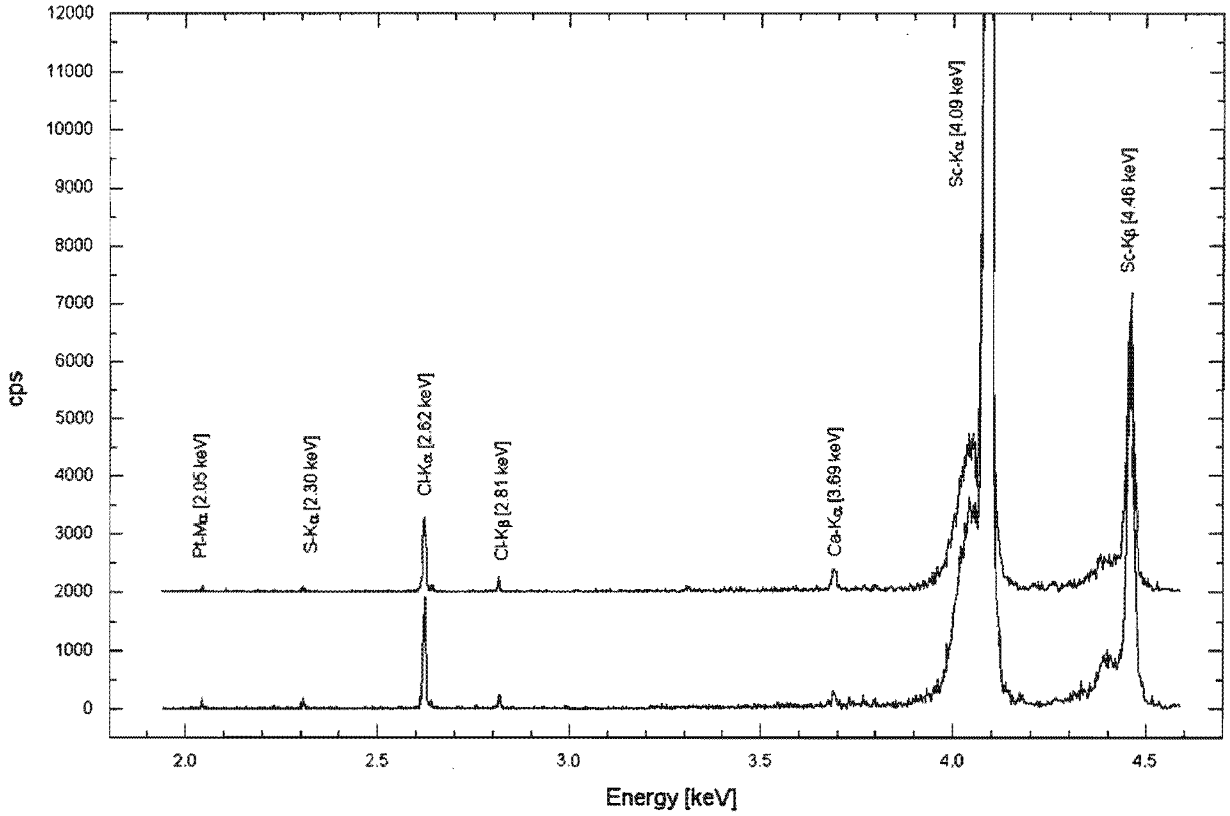

Fig. 5.9: XRF-scan of the alumina substrate from 1.9 keV to 4.6 keV (upper graph shifted to 2000 cps for comparison)

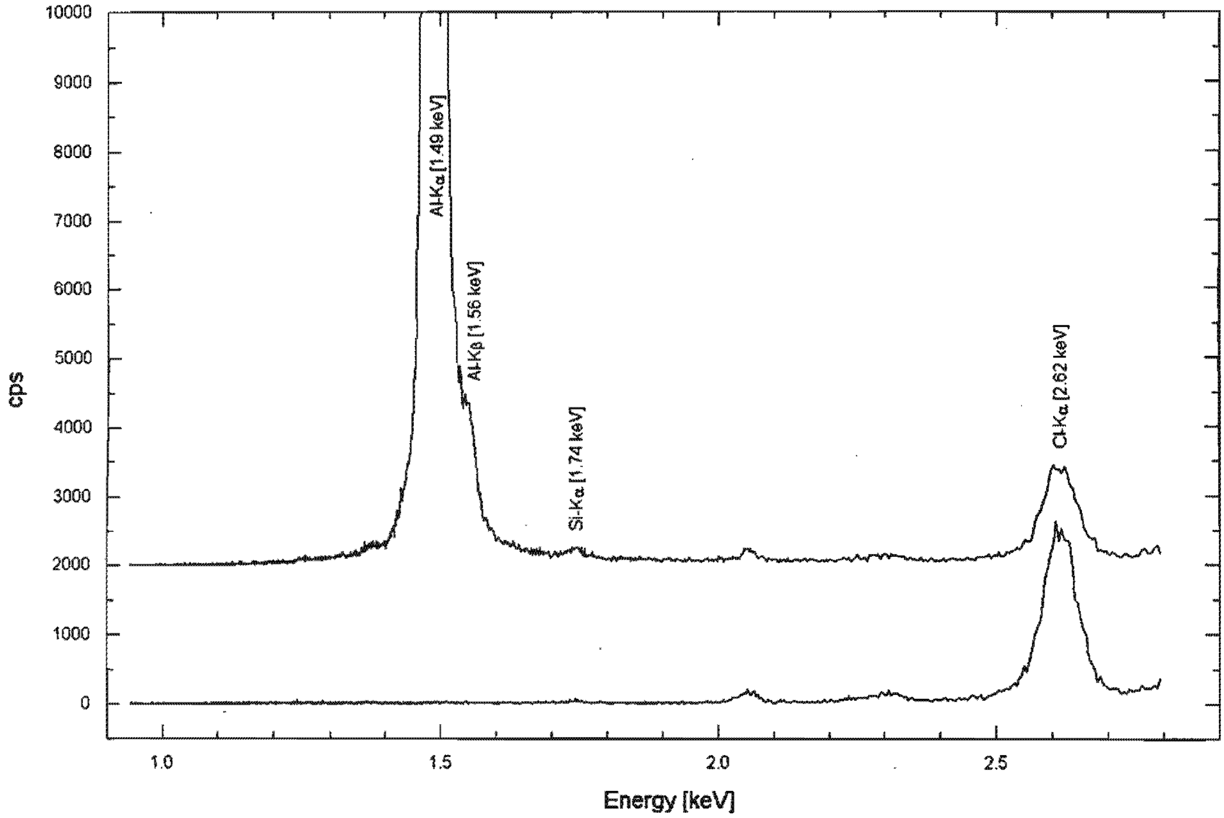

Fig. 5.10: XRF-scan of the alumina substrate from 1 keV to 2.7 keV (upper graph shifted to 2000 cps for comparison)

The XRF-scans in Figures 5.8-10 are very similar to the XRF-scans of the platinum coated surface. Again the lower graphs show the reference scans of the sample holder and as before all the characteristic lines for the x-ray target and the epoxy resin can be found. In fig. 5.10 the aluminum peak is clearly visible, but the oxygen fluorescence radiation, at an energy of 0.52 keV, is not within the recorded range. The Al_2O_3 seems to be of high purity as well except for some traces of calcium in fig. 5.9 and silicon in fig. 5.10.

In the preceding sections we have seen that both the platinum and aluminum oxide are of high purity. The polycristalline platinum layer is about 1 µm thick and its grains have an average size of 1.7 µm × 1.7 µm. Furthermore, by comparing the theoretical values, we can see that the coefficient of linear expansion of platinum is considerably larger than that of aluminum oxide. It is therefore justified to assume that some residual stress may have been introduced during the production and processing of the layer. In subsequent chapters this will be investigated.

6 Measurements

6.1 Measured reflections

Because of the limitations of the diffractometer and of the peak intensities not all of the available Bragg reflections were measured. Table 6.1 lists all reflections with a Bragg angle smaller than 75° and the measured peaks are marked with a star (*). The first column in the table gives the Miller index (hkl) of the diffracting lattice plane, the second column its spacing (d) and the following two the corresponding Bragg angle (θ) and the doubled angle respectively. The last column gives the theoretical peak intensity relative to the reflection of the (111) lattice plane.

hkl	d [Å]	θ [°]	2θ [°]	Intensity [%]
111	2.2650	19.882	39.763	100
200	1.9616	23.121	46.243	53
220 *	1.3873	33.727	67.454	31
311 *	1.1826	40.643	81.286	33
222 *	1.1325	42.856	85.712	12
400	0.9808	51.754	103.508	6
331 *	0.9000	58.856	117.711	22
420 *	0.8773	61.404	122.807	20
422	0.8008	74.131	148.262	29

Tab. 6.1: Bragg reflections of Pt for Cu-Kα_1 radiation with Bragg angles smaller than 75°. (Data from [JCPD97])

In order to choose the right reflections for a meaningful measurement many factors have to be taken into account.

Firstly we must remember that the apparatus used in our measurements is an Ω-goniometer as decribed in chapter 2. Hence the ψ-tilt is limited to the Bragg-angle θ. However, if we want to apply the "*d-sin*$^2\psi$"-method as described in chapter 1, a wide range of ψ-angles must be covered in order to obtain a meaningful curve. Considering this, we see that the two strongest reflections (111) and (200) are useless, because their maximum ψ-tilt is about 20°. In fact, even the reflections up to a Bragg-angle of 50° are hardly useful. In general we can say, the higher the Bragg-angle the better.

Unfortunately it was also not possible to measure the (422) reflection with the largest Bragg-angle, again because of instrumental difficulties. As we have seen in chapter 2, the goniometer's 2θ circle is equipped with a long detector arm for high resolution x-ray diffraction. For 2θ angles greater than 134°, the detector arm touches the x-ray-tube-carrier, resulting in severe misalignments and finally knocking over the whole carrier including the assembly for the slit system (see fig. 2.3). Hence, the (422) reflection with a 2θ angle of 148° is out of the measurement range.

In addition to the above mentioned limits for peak detection and ψ-tilting, there is another restriction on the measurements. Caused by the strong fibre texture of the platinum film, the peak intensities vary tremendously over a relatively small ψ range. In order to understand this phenomenon we must first look at the crystal structure of platinum. Platinum usually crystallizes in a face-centered cubic structure as shown in fig. 6.1.

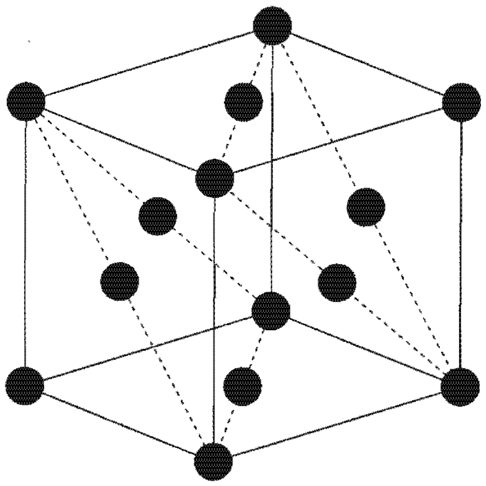

Fig. 6.1: Crystal structure of platinum. The dashed lines indicate the cubic-close-packed (111) planes.

It is a special characteristic of the fcc crystal that the (111) lattice planes are arranged in the cubic-close-packed structure ABCABC... . Therefore it is very likely that the atomic layers of a platinum film are organized in this structure if the film is grown on a smooth surface. Since there is no restriction on rotation around the [111] axis for a single grain, most crytallites are arranged with a set of (111) planes parallel to the surface but otherwise completely at random. This results in a typical fibre texture.

The substrate can also influence the texture of a growing film. In some cases it can even enforce (100) or (110) textures on fcc structures, but in most cases a (111) texture is found in platinum films [GMEL74].

We can therefore assume that we are dealing with a (111) fibre texture and the measurements will confirm this later. The important consideration at this stage, however, is the effect of the fibre texture on the intensity of the reflection. Since most of the grains are orientated with a (111) plane parallel to the surface we expect a very strong peak if we measure the (111) reflection without a ψ-tilt, i.e. $\psi = 0°$. On the other hand it will be extremely difficult to measure the same reflection at a high ψ angle, because of the fact that only a few grains are then in a favourable orientation for diffraction. The same argument holds for other lattice planes, except that their intensity maximum is shifted to a ψ angle equal to the angle between the diffracting plane and the (111) plane. At this ψ angle we always measure at the abundant grains that contribute to the fibre texture.

The angle between the (400) and (111) plane e.g., is about 54.7°. If we compare this angle with the Bragg angle of 51.8°, we can see, that the maximum intensity occurs beyond the maximum ψ-tilt. This, and the fact that the (400) reflection, with its 6% relative intensity, is very weak anyway, is the reason why it was not possible to measure the corresponding (400) peak.

In order to visualize the positions of the measured lattice planes relative to the (111) plane, fig. 6.2 shows their arrangement in a unit cube and gives their angles to the (111) plane.

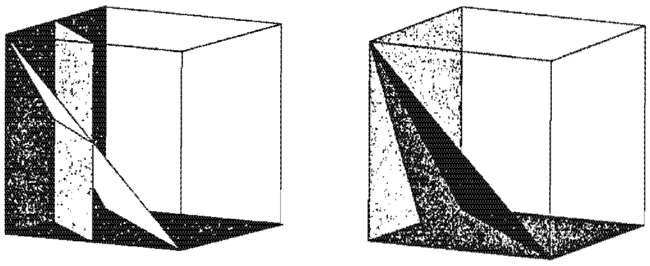

(111) and (220) plane
angle: 35.26°

(111) and (311) plane
angle: 22.00°

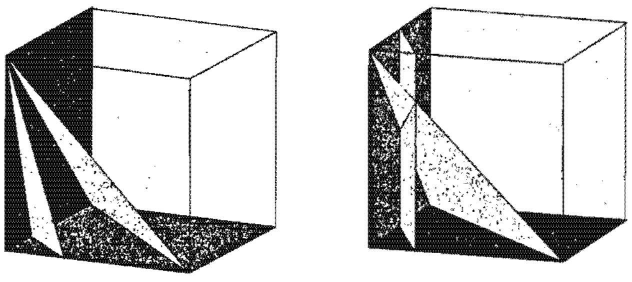

(111) and (331) plane
angle: 29.50°

(111) and (420) plane
angle: 39.23°

Fig. 6.2: Arrangement of various lattice planes with respect to the (111) plane

6.2 Measured Peaks

For all the reflections marked with a star (*) in table 6.1 the corresponding peaks were measured with the position sensitive detector and displayed as a number-of-counts versus channel-number plot. After rescaling the x-axis as described in chapter 3, we obtain an intensity versus 2θ-angle plot, from which the peak position can be derived directly. In order to determine the position as precisely as possible, a Lorentz-curve was fitted to the data representing the peak (fig. 6.3). The fitting was done with the built-in function of Microcal's program "Origin", in which the Lorentz-curve is given by the equation

$$y = y_0 + \frac{\frac{2A\sigma}{\pi}}{\sigma^2 + 4(x - x_c)^2} \tag{6.1}$$

The parameter A represents the peak's integrated area and σ the Full-Width-at-Half-Maximum (FWHM) value. x_c gives the position of the peak's centre and is therefore the parameter we are looking for. y_0 finally represents the background noise, which is considered to be constant over the fitted range. All parameters are varied in the fitting process in order to obtain the best curve. Fig. 6.3a shows the plot of the very strong (222) peak, measured at its intensity maximum ($\psi = 0°$). The elapsed measuring time was only 1 h but the peak still reaches about 7000 counts in height. The two overlapping peaks make it necessary to perform a multiple peak fit, where two single curves are added and the result is fitted to the actual data points. The dashed lines in fig. 6.3a represent the single curves that are added in order to obtain the solid line graph. The data points itself are not connected, but are so dense in some areas that they appear as a line graph. We can see that the fit in fig. 6.3a is a very good fit with very little deviations from the data points' curvature. Fig. 6.3b on the other hand shows the very weak (420) peak at a ψ-tilt far from the intensity maximum. The deviations of the data points from the fitted graph appear to be larger here, but we must consider that the signal-to-noise ratio is very bad. The variations of the data points are actually of the same magnitude as the variations in fig. 6.3a. Since we are only interested in the peak's position, the influence of a bad signal-to-noise ratio is not that important as long as the peak is not completely lost in the noise. Hence the data collected from weak peaks like the one in fig. 6.3b are still accurate and the error in the peak position is hardly different to that from strong peaks. The reason for this is the Full-Width-at-Half-Maximum (FWHM) value, which we chose as an estimation for the error of the peak position. The statistical error which was calculated with the fitting function in the "Origin" program often had problems with peaks with a small signal-to-noise ratio. Sometimes the error was as large as several degrees although the peak position could be determined to ± 0.1° with the naked eye. We therefore decided that a quarter of the FWHM value is a good and safe estimation for the error in peak position.

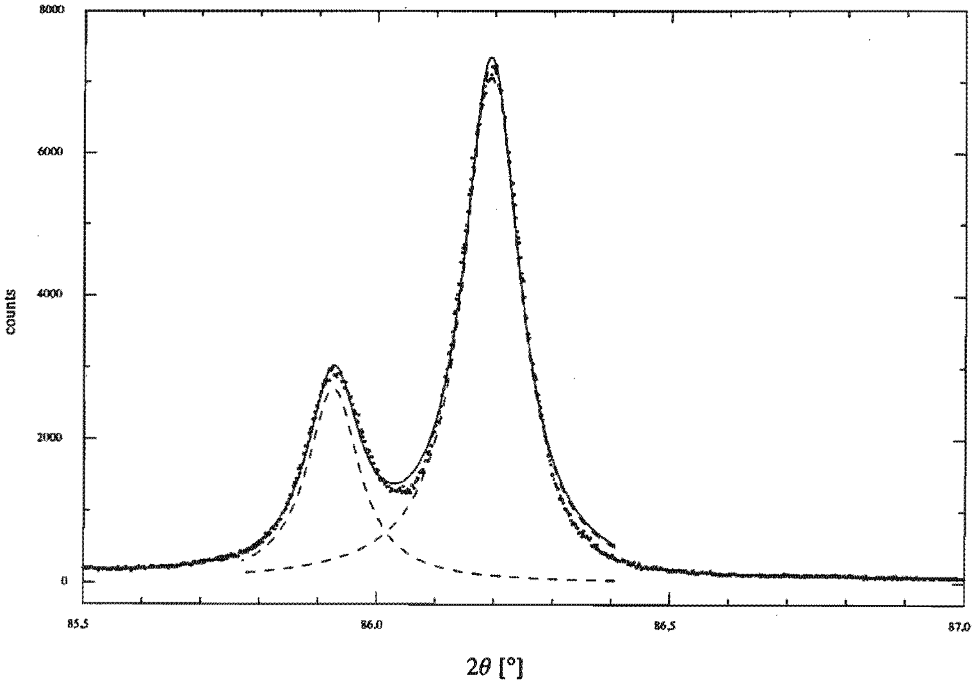

Fig. 6.3a: Lorentz-Fit for the (222) Kα_1 and Kα_2 peaks at $\psi = 0°$

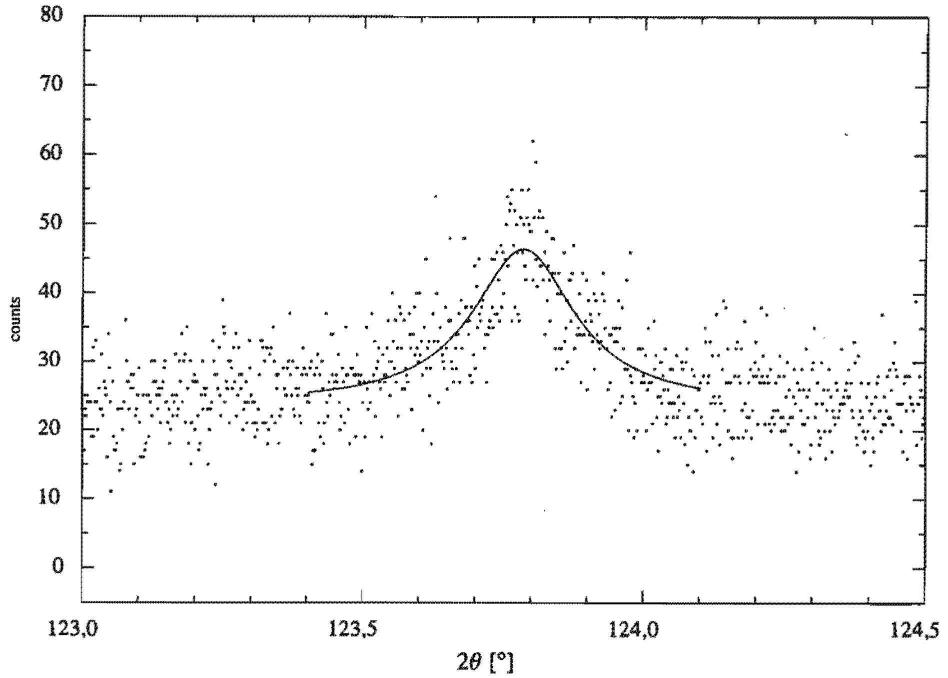

Fig. 6.3b: Lorentz-Fit for the (420) Kα_2 peak at $\psi = 5°$

In order to get a good overview of the measurements, several intensity versus 2*θ*-graphs of the same reflection were put together in one plot (fig. 6.4 a-d). The various graphs correspond to different *ψ*-angles, with consecutive graphs shifted to higher values in order to be able to distinguish the single measurements. Additionally all graphs were normalized to 1 h of elapsed measuring time. This allows a direct comparison of the peak intensities. The disadvantage of this display method is the loss of small peaks in the large scale of the peaks' intensity maximum. Most peaks that are no longer visible in fig. 6.4 a-d were in fact still measurable. A detailed summary of all measured peaks including their position, FWHM value and elapsed measuring time is given in the appendix.

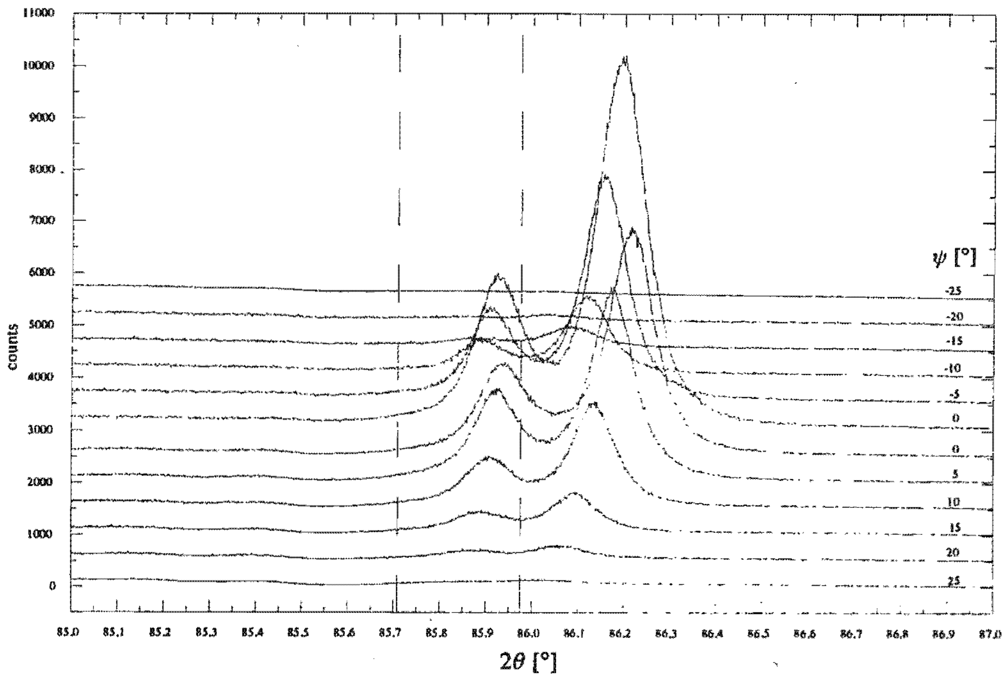

Fig. 6.4a: (222) peak at various *ψ*-tilts, normalized to 1h elapsed measuring time

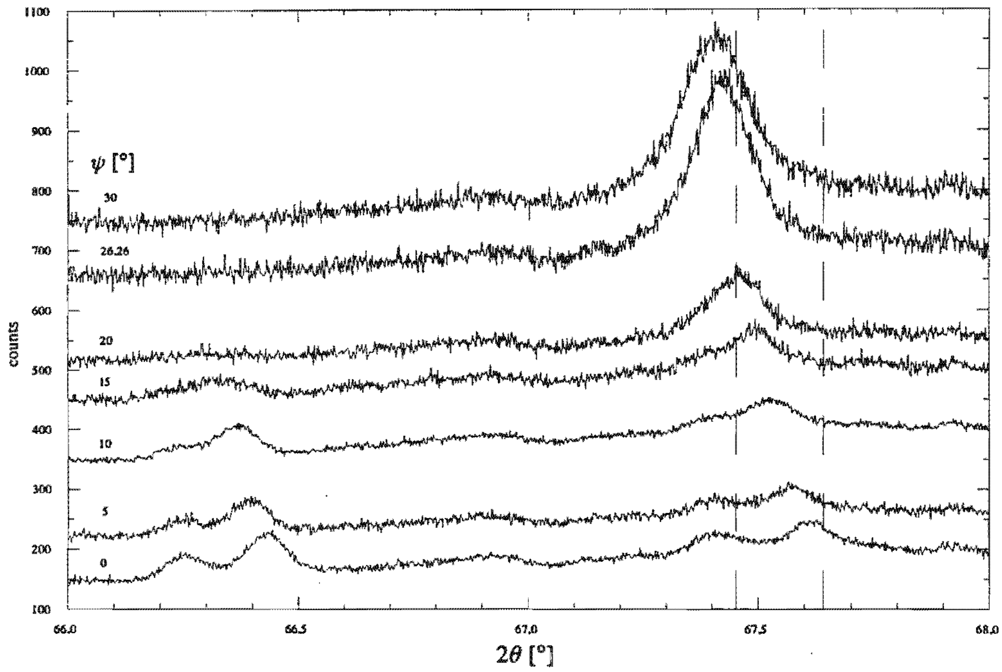

Fig. 6.4b: (220) peak at various ψ-tilts, normalized to 1h elapsed measuring time

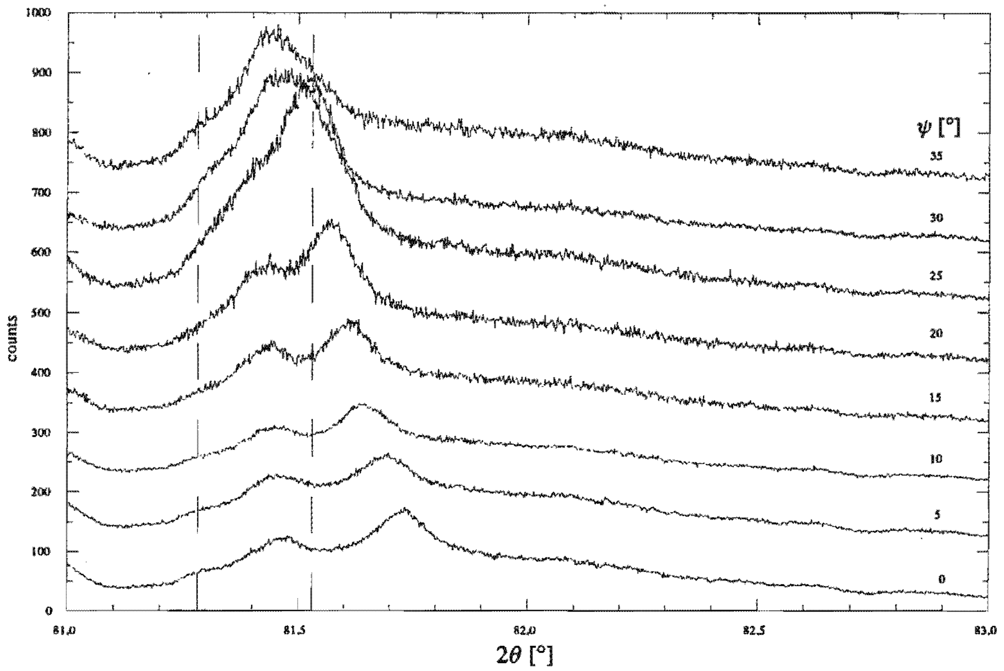

Fig. 6.4c: (311) peak at various ψ-tilts, normalized to 1h elapsed measuring time

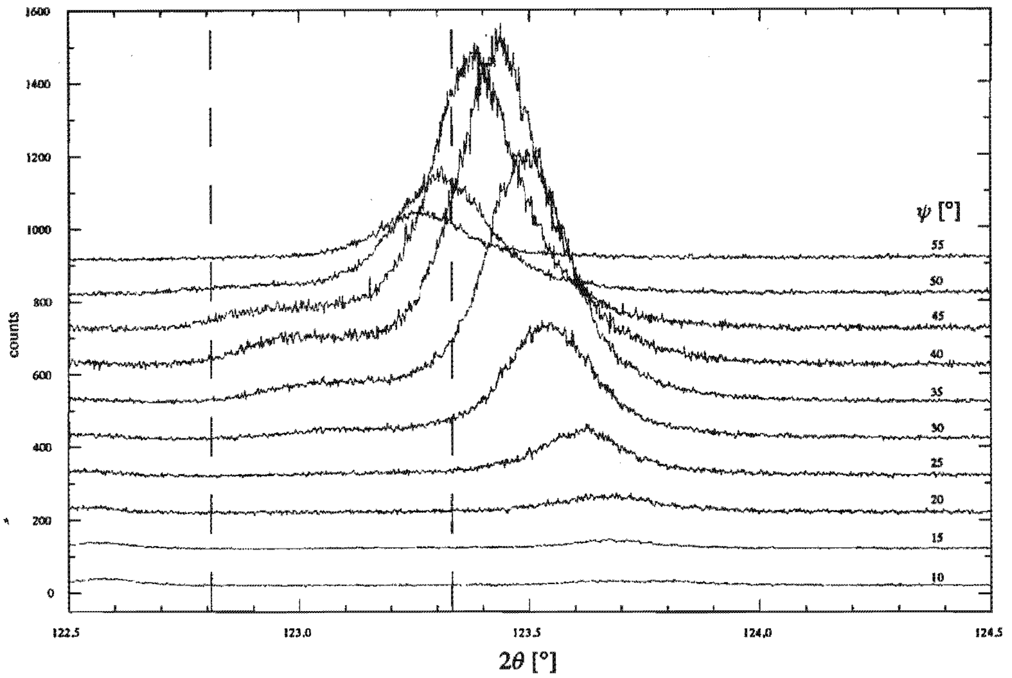

Fig. 6.4d: (420) peak at various ψ-tilts, normalized to 1h elapsed measuring time

Comparing the figures 6.4 a to d, we can see that all reflections occur as a double-peak. This effect is caused by the monochromator which can not be adjusted to filter Kα_2 radiation. Hence the incident x-ray beam is not really monochromatic, but a mixture of Kα_1 and Kα_2 radiation. The two characteristic peaks of the two primary radiations can of course be seen in the reflected beam, causing a double-peak.

Since the Kα_1 radiation has a higher intensity than the Kα_2 radiation, one would expect a double peak with different heights. This is indeed the case, but according to the wavelengths of Kα_1 and Kα_2 radiation the stronger Kα_1 peak has a smaller Bragg-angle and should appear on the left side of the plot. Unfortunately all the plots show a weaker peak at a smaller Bragg-angle and a strong peak at a higher angle. The reason for this contradiction is again the monochromator. As some tests after the measurements showed, some of the integrated slit systems in the monochromator were adjusted in a way that they blocked most of the intensity from the Kα_1 radiation, but almost nothing from the Kα_2 radiation. By opening the slits the normal intensity distribution was observed, but the background noise also became very strong, because the beam was no longer monochromatic. Hence the reflection caused by the Kα_2 radiation was used for determining the peak positions.

In order to compare the peak positions with the literature value on the 2θ-scale, each plot contains two dashed, vertical lines: The left line indicates the literature value of 2θ-angle for the Kα_1 peak and the right one for the Kα_2 peak. Unfortunately deviations of 0.1° to 0.2°

from the literature value can be found in fig. 6.4a. The other reflections show deviations too, but not as strongly. One reason for these deviations could be an improper positioning of the detector. In other words: The 2θ-calibration and the outer goniometer circle itself is lacking precision. But there is also the effect of a stressed lattice spacing at $\psi = 0°$. This will be discussed in greater detail in the following chapter, but we can already see that the (220) double peak with the smallest Bragg-angle (fig. 6.4b) is still left of the dashed lines of the theoretical 2θ-value and that the peaks are more and more shifting towards the right with increasing Bragg-angle. Since we are only interested in the shifts of the peaks at various ψ-tilts and the detector is not moved during such a measurement series these deviations are usually not important for our measurements. The dashed lines just confirm that the measured peaks are really the expected platinum diffraction peaks.

Fig. 6.4a shows the double-peak graphs of the (222) reflection. The displayed 2θ range is of course just a small part of the 7° detector range. The corresponding ψ-angle of each graph given in the plot does not indicate a negative ψ-tilt as one would expect. Because of the greater misalignment effects at negative ψ-angles, which can easily be seen in equation 3.1, measurements were only taken for positive ψ-tilts. The negative values were obtained by measuring at positive ψ-tilts and a φ-rotation of 180°. Because the same (hkl) planes are in a favourable condition for diffraction then, this arrangement is equivalent to a negative ψ-tilt. Only the directions of the incoming and reflected beam are reversed.

The negative ψ-angles of the (222) reflection are shown in fig. 6.4a, in order to make the influence of the strong fibre texture more clear. As we have mentioned above, the intensity maximum of the (222) peak occurs at $\psi = 0°$. Indeed, the plot shows an impressive growth of intensity coming from negative ψ-angles towards the maximum at $\psi = 0°$. Going further to positive ψ-angles, the peaks are fading at the same rate, so that at $\psi = +25°$ and $\psi = -25°$ the peaks vanish completely.

All the other measured peaks show the same behaviour, but of course at different ψ-angles. Negative values for ψ are not shown in fig. 6.4b-d, in order to keep a clear overall view. Nevertheless each peak was measured at $\varphi = 0°,45°,90°$ and 180°. In fig. 6.4 only the plots for $\varphi = 0°$ are shown, because the plots for the other φ-angles are so similar that one can hardly see any difference.

In fig. 6.4 b and c we can see another problem of our measurements: At small ψ-angles the $K\alpha_1$ and the $K\alpha_2$ peaks are well separated, but at increasing ψ-tilts they overlap more until at a ψ-angle of 20° or 25° only a single peak is visible. This means, that we must be careful with the peak positions measured at high ψ-angles, because it is not clear how much the stronger Kα_2 peak is influenced by the Kα_1 peak. The reason for this melting together of the two peaks is decribed in [FANI76]: The Ω-goniometer's Bragg-Brentano focussing arrangement causes a peak broadening with increasing ψ-tilts.

This effect is especially disturbing when the Kα_1 and Kα_2 peaks are not well separated as in fig. 6.4 b or c. According to Bragg's law a small change in the wavelength requires a rather large change in the Bragg-angle, if we measure at a high Bragg-angle. This can be seen in fig. 6.4d at the (420) peak, where the Kα_1 and Kα_2 peaks are much further separated than in fig. 6.4b or c. An overlap, even at ψ-tilts of 45°, does not occur anymore.

So far the (420) reflection is the only one which promises a meaningful "d-$sin^2\psi$" plot, but we have not yet considered the (331) reflection. Fig. 6.5 shows the (331) double peak series at $\varphi = 0°$ in a ψ range from 0° to 55°. Because of the fibre texture the (331) peak shows the characteristic intensity maximum just like all the other peaks. The remarkable thing, however, is, that even far away from the maximum the intensity does not drop to nearly zero. Rather it drops to a constant value with a peak height of approximately 100 counts per hour. Only at a ψ-tilt of 55°, very close to the Bragg-angle of almost 59°, the inclination angle of the incident x-ray beam becomes too small and the peak vanishes.

In order to find the reason for this constant peak intensity we should examine the 10° ψ-tilt. The Kα_2 peak on the right shows a step at the top of the peak. Although this might be pure coincidence it puts us on the right track: The peak seems to be a strongly overlapping double peak. By comparing the double Bragg-angles of platinum and corundum, we find that the (331) platinum reflection with a 2θ of 118.18° (Kα_2) is very close to the (420) corundum reflection with a 2θ of 118.25° (Kα_2). The difference of 0.07° is surely too small to expect seperated peaks. Although we cannot prove it, it is very likely that scattered x-rays from the corundum substrate pass through the platinum layer and spoil the measurements. We therefore abandoned any further measurements of the (331) peak and did not consider applying the "d-$sin^2\psi$" method.

After all, it is really only the (420) reflection which is suitable for meaningful "d-$sin^2\psi$" plots.

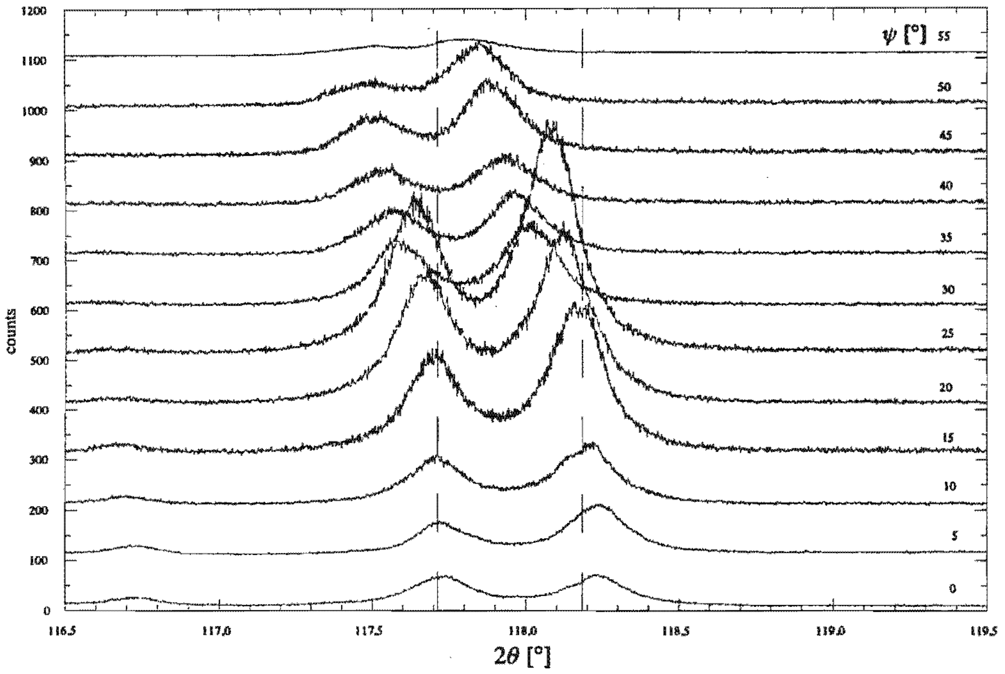

Fig. 6.5: (331) peak at various ψ-tilts, normalized to 1h elapsed measuring time

6.3 Pole figures

So far we have seen many arguments for a strong fibre texture in the platinum layer. In order to verify these arguments an attempt was made to measure a complete pole figure. A pole figure shows the intensities of a diffraction peak over the maximum ψ- and φ-range, which means measurements at ψ-angles up to 90° and at φ-rotations of 360°, both in steps of at most 5°. From a set of such pole figures the orientation distribution function (ODF) can be derived, which in turn can be used to calculate the x-ray elastic constants (see chapter 1).

The problem with the measurement of pole figures is, that it is extremely time consuming. Depending on the measuring time of a single peak-intensity a complete pole figure can take days or even weeks. For this reason we started to measure a pole figure, in steps of 5°, for a φ-rotation of 90° rather than a full circle. In order to be able to see the intensity rise and fall within the possible ψ-range, the (311) peak was chosen for the measurements. With a Bragg-angle of approximately 40° and a theoretical intensity maximum at 22° ψ-tilt, the fibre texture should be clearly visible in the pole figure. Furthermore the (311) reflection with a relative intensity of 33% allows the single measurement time to be shorter than a measurement of most other peaks. Nevertheless, to obtain a reproductible measurement, a measuring time of 30 minutes for a single intensity measurement was necessary. For a complete φ-rotation of 360° and ψ-tilts of 35° both in steps of 5° this adds up to 576 single measurements, which would mean a pure measuring time of 288 hours.

Unfortunately even then the pole figure would be incomplete, because the ψ-tilt is very limited. To measure over the full ψ-range of 90° a Ψ-goniometer is necessary. Furthermore the intensities at high ψ-angles cannot be determined in reflection, because of the beam-inclination-angle becoming too small. It is therefore necessary to measure in transmission. For all these reasons the pole figure is incomplete and hence insufficient for the calculation of the ODF. However, if the small part of our pole figure shows the expected fibre texture, it is possible to assume that the measured intensities at high ψ-tilts are constant and that the pole figure is symmetrical for any φ-rotation.

The measurement itself was conducted in much the same way as the measurements of stress. However, since we are not interested in the peak position the data points were not fitted, but integrated over a range of 600 channels in order to obtain the overall peak-intensity. The interval of 600 channels had a fixed position on the 2θ-scale and was chosen to be wide enough to allow the peak to shift without leaving the interval. Fig. 6.6 shows the measured intensities arranged in a 3 dimesional wireframe diagram, with the φ- and ψ-angles on the linear horizontal axes and the intensity on the vertical axis. With regard to a better judgement of the rotational symmetry some measurements were taken beyond the φ-range of 90°.

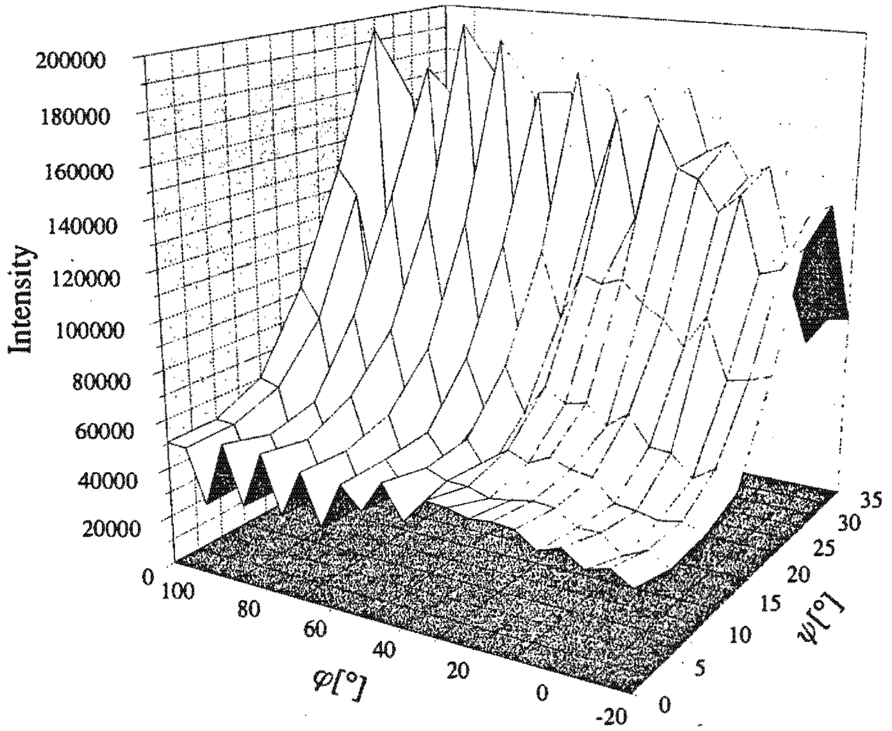

Fig. 6.6: 3D wireframe pole figure for the (311) reflection

The pole figure in fig. 6.6 indeed shows the general features of a fibre texture: The intensities of the peaks are growing with the ψ-angle towards a maximum. Beyond the maximum they decline with higher ψ-tilts.

The diagram is not smooth, there is a considerable difference in consecutive φ-angles, which is best seen from 40° to 110° on the φ-axis, causing a ripple in the graph. In order to understand this phenomenon we must consider the order in which the measurements were made. The first series of measurements started at $\varphi = -20°$ and continued in steps of 10°. For each φ-angle, the ψ-tilts were measured from $\psi = 0°$ to 35° before the φ-angle was increased. After that a second series of measurements was performed, this time starting at $\varphi = 5°$ but with the same increase in the φ-angle. Fig. 6.6 a and b show the different measurement series in separated diagrams.

The two diagrams are remarkably different. The first diagram shows a very uneven distribution of intensity. The intensity maxima differ by 100% in the extremes and it is even worse at the minima at $\psi = 0°$. The second diagram is in sharp contrast to that: Although there is a continuous rise in the intensities with increasing φ-angle, the graph is remarkably smooth and shows an almost perfect behaviour for a fibre texture. The fact that the measurements at the even φ-angles are in no way special compared to the measurements at odd φ-angles, implies that it is not the sample which causes the strange behaviour in fig. 6.6a. Considering the order in which the measurements were taken, it seems that the diffractometer system was not working in a sufficiently stable way during the first series of measurements. If this was caused by fluctuations in the primary beam-intensity, uneven background radiation, flaws in the detector or its electronics or anything else, we could not determine. Although the pole figure is not suitable for calculating the ODF, fig. 6.6b verifys the strong fibre texture.

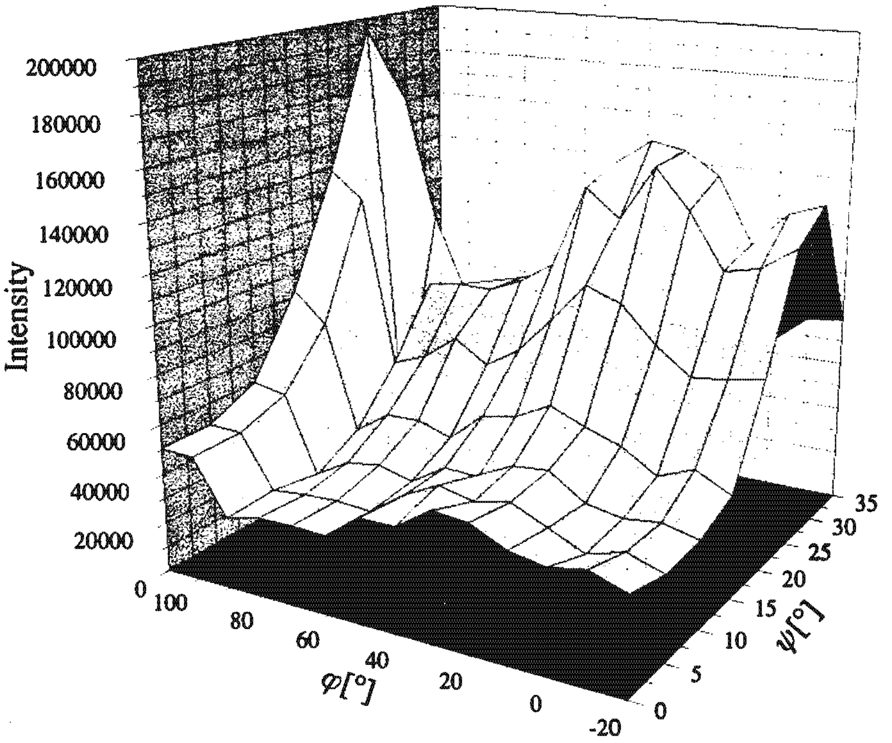

Fig. 6.6a: 3D wireframe pole figure for even φ-angles

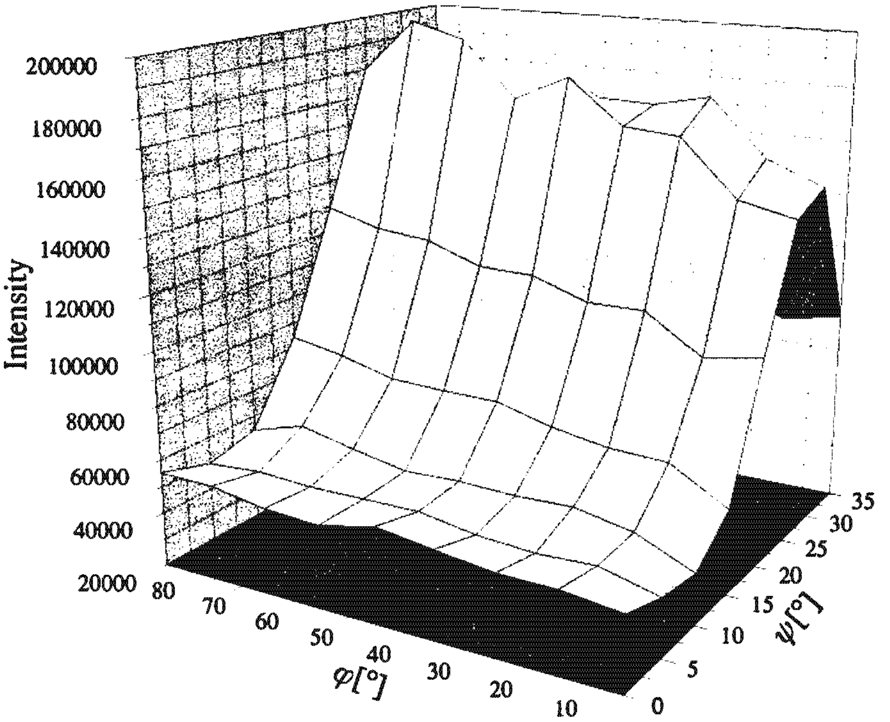

Fig. 6.6b: 3D wireframe pole figure for odd φ-angles

To make sure that the effects causing the flaws in fig. 6.6a are instrumental artefacts, pole figures were also measured with a commercial Philips Ψ-goniometer. Unfortunately, the pole figure for the (311) reflection was not measured so a direct comparison of the pole figures is not possible. On the other hand all the pole figures measured with the Ψ-goniometer show such a perfect fibre texture that a direct comparison is not necessary.

The diagrams are similar to the ones in fig. 6.6 with the φ- and ψ-angle in the horizontal plane and the intensity on the vertical axis. However, the φ-angle is not arranged in a straight line but a circle, which gives a better overview of the complete pole figure. We can see the pole figures for the (111), (200) and (220) reflection in fig. 6.7, with the full ψ-range of 90°. The theoretical ψ-angle for the intensity maximum is also given for each pole figure and we can see that they are in perfect agreement with the pole figures. One must know for a comparison however, that the grid in the graphs has a division of 90° for the φ-angle (which is rather obvious) and a devision of 30° for the ψ-angle. Since the measurements were performed with a ψ-goniometer the pole figures are complete and the outer rim represents a ψ-angle of 90°.

These pole figures show very clearly that the platinum layer has an almost perfect (111) fibre texture.

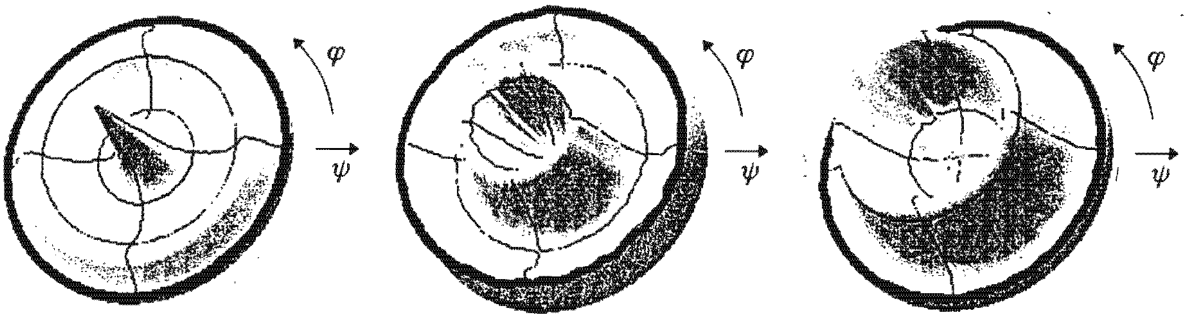

(111) pole figure
theo. intensity maximum
at $\psi = 0°$

(220) pole figure
theo. intensity maximum
at $\psi = 35.3°$

(200) pole figure
theo. intensity maximum
at $\psi = 54.7°$

Fig. 6.7: Pole figures for various reflections measured with a Ψ-goniometer

7 Results

7.1 "d-$sin^2\psi$" graphs

With the help of Bragg's law and the measured peak positions given in the appendix, the corresponding lattice spacings d were calculated and presented in a d versus $sin^2\psi$ graph (fig. 7.1). For a direct comparison of the "d-$sin^2\psi$" graphs the x- and y-scales are identical for all plots.

One can see immediately that the measured ψ-range is too small for most of the peaks. The development of the graphs at high ψ-angles can only be infered and therefore it would be incautious to assume a straight line. As already mentioned in the previous chapter, the (220), (222) and (311) reflections are not suitable for determining the stress, because of this limitation. Only the (420) reflection (fig. 7.1d) covers a sufficient ψ-range and additionally shows a very good linear behaviour.

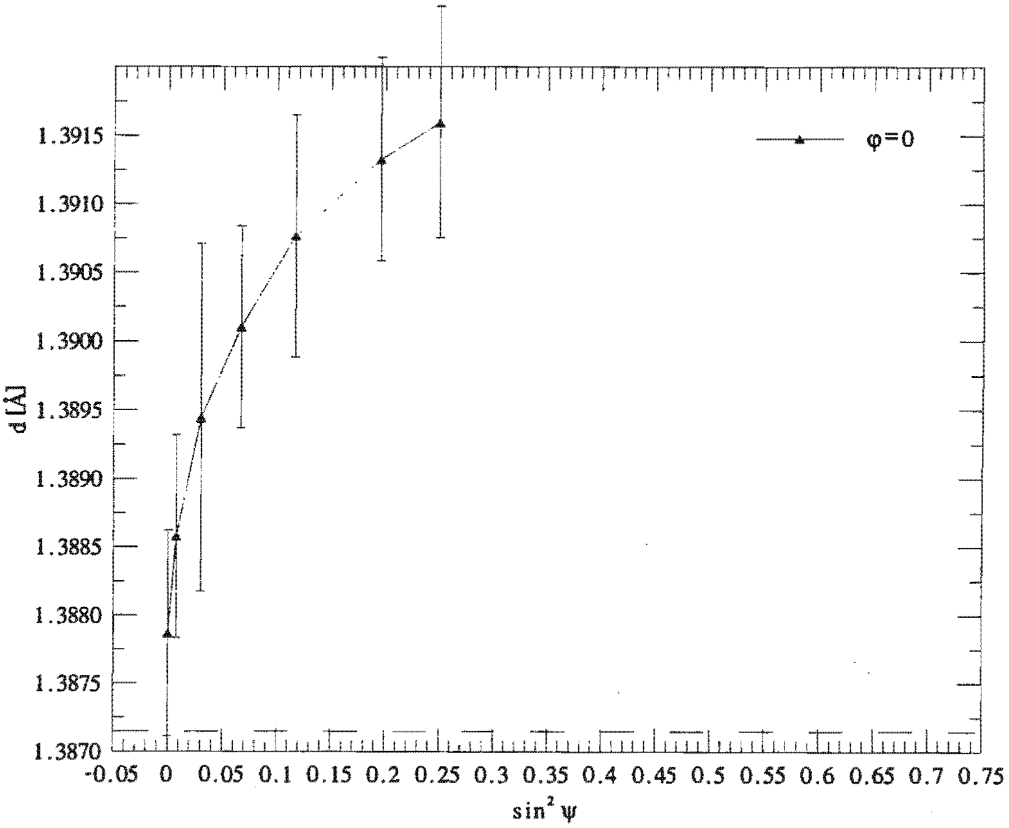

Fig. 7.1a: "d-$sin^2\psi$" graph of the (220) reflection

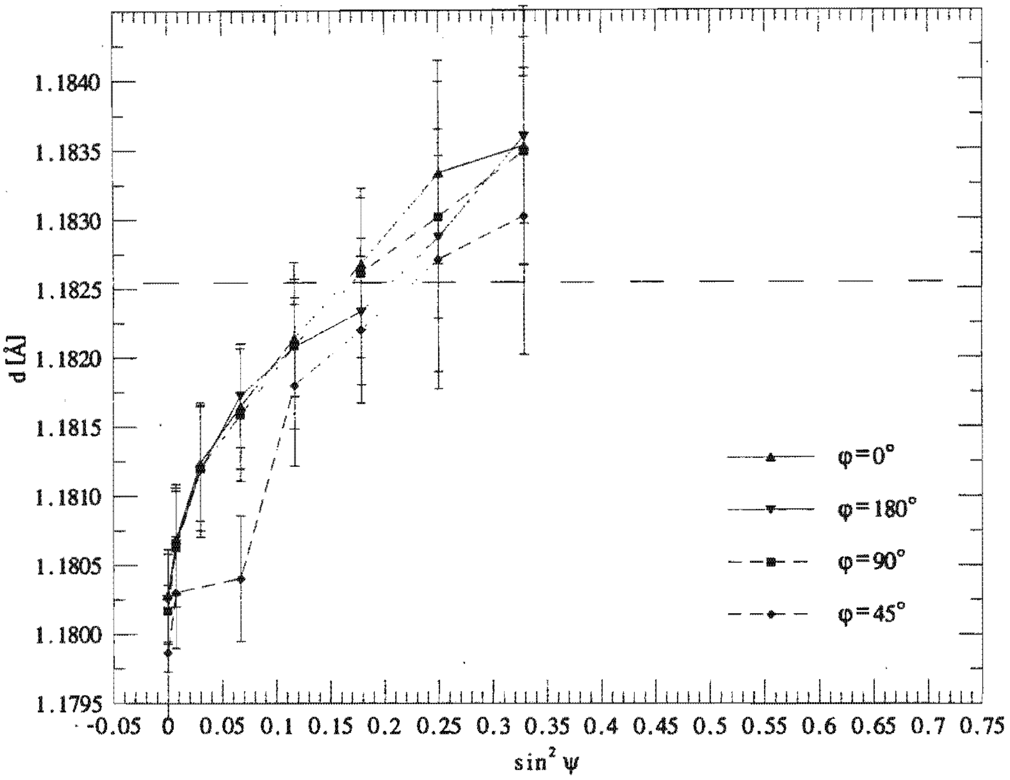

Fig. 7.1b: "d-$\sin^2\psi$" graph of the (311) reflection

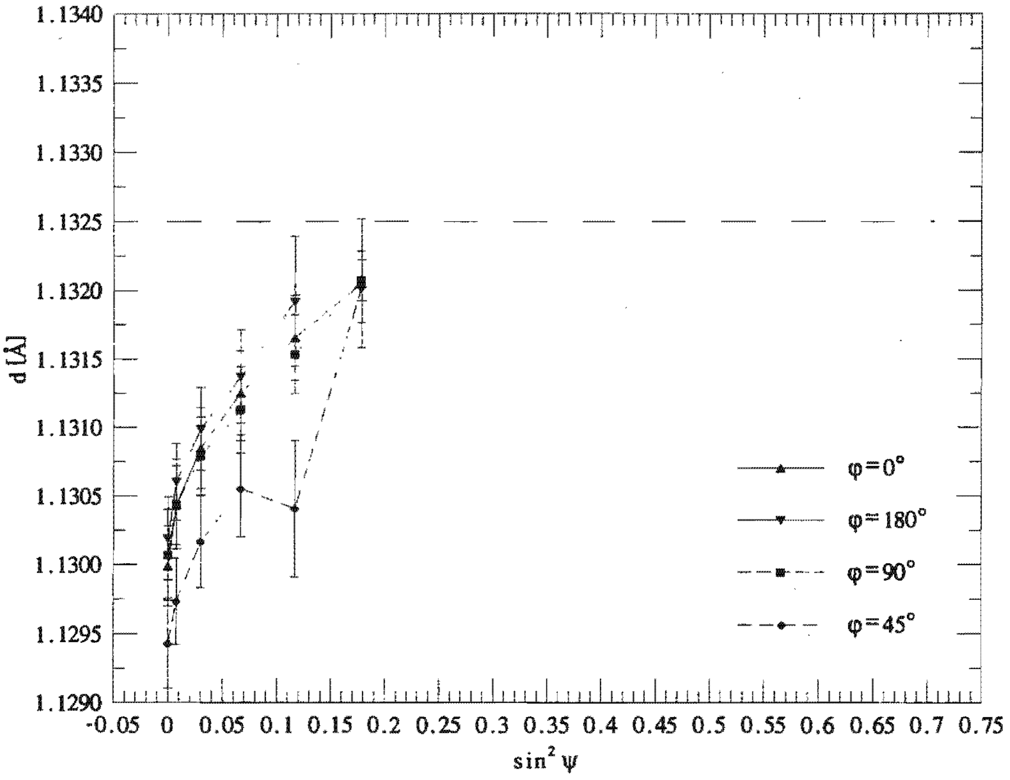

Fig. 7.1c: "d-$\sin^2\psi$" graph of the (222) reflection

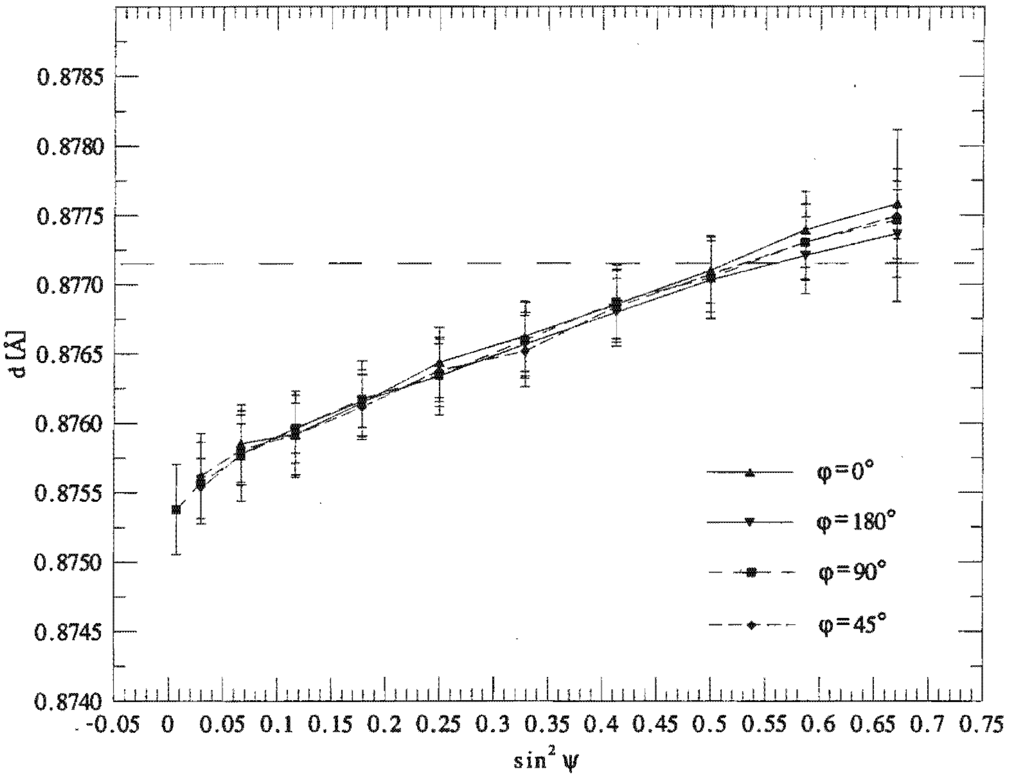

Fig. 7.1d: "*d-sin*$^2\psi$" graph of the (420) reflection

On the other hand the (220), (222) and (311) "*d-sin*$^2\psi$" graphs are not completely useless. It can be seen e.g. that there is almost no deviation for the measured lattice spacings at φ-rotations of 0° and 180°, which means that there is no "ψ-splitting" for negative and positive ψ-values. Hence, we know from chapter 1 that the σ_{X3} shear components are zero in this case.

Another interesting point is the graphs' curvature in fig. 7.1 a-c. We have also seen in chapter 1 that such a curvature is usually caused by a stress gradient within the penetration depth. The stress component that is most likely to change below the sample's surface is the σ_{33} component. Because of the stress equilibrium equations, the σ_{33} component must be zero at the surface, but it may grow rapidly with depth. In order to understand why this causes a curved "*d-sin*$^2\psi$" graph, we should have a look at the x-ray's penetration depth with respect to the Bragg-angle θ and the ψ-tilt. Fig. 7.2 shows a plot of the theoretical penetration depth versus the ψ-tilt for an Ω-goniometer, derived from equation (1.23). If we compare the penetration depths at small ψ-tilts for the various Bragg-reflections, we can see that they cover a range from 0.65 µm to 1.03 µm. Let us now look at the "*d-sin*$^2\psi$" graphs and examine the curves in order to find some relation between the curvature and the penetration depth. Indeed, we find that the curvature of the (220)-graph with the smallest penetration depth is very marked over a wide ψ-range. The (311)- and (222)-graphs with almost the same penetration depth look very similar: There is a strong curvature at ψ-angles up to 10°, but then the graphs straighten. The (420)-graph finally, with the greatest penetration depth, only shows a very weak curvature at small ψ-tilts. We can see in fig. 7.2 that the penetration depth for each reflection does not change much within a ψ-angle of 10°. The effect must therefore be based on different stress gradients at different depths: At regions with an almost constant stress component the measured lattice spacing would hardly differ if the penetration depth changes slightly, but at regions with a strong stress gradient a small change in the penetration depth can alter the measured lattice spacing significantly. Thus, in our case, the stress gradient is very weak deep inside the material and getting stronger closer to the sample's surface. We also know that the stress must be biaxial at the surface as mentioned above.

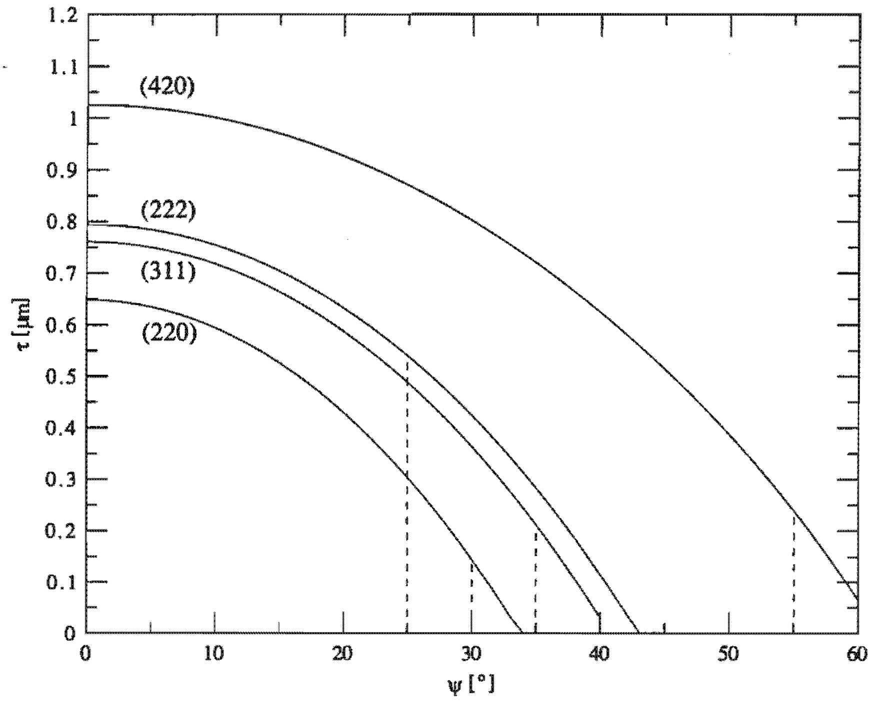

Fig. 7.2: Penetration depth of Cu-Kα radiation in platinum for an Ω-goniometer

In order to visualize the stress distribution, fig. 7.3 shows schematically the lattice planes of three different grains. The displayed stress gradient is negative, which means that the stress perpendicular to the surface is compressive. This assumption is based on two considerations: Firstly, we can see that the slopes in the "d-$\sin^2\psi$" graphs are positive, which means that the stress parallel to the surface is tensile. It then follows from the theory of elasticity [HAHN84] that the perpendicular stress must be compressive.

Secondly, the "d-$\sin^2\psi$" graphs show that the lattice spacing is growing rapidly with a smaller penetration depth, which means that the spacing must be bigger closer to the surface. Since the lattice spacing is unstressed at the surface it follows that a compressive stress is causing a decrease of the spacing with depth.

The compressive stress is also confirmed by a comparison of the literature unstressed lattice spacings with the measured lattice spacings at $\psi = 0°$. The literature values are represented by a dashed line in fig. 7.1. One can see, that the measured lattice spacings are always smaller than the literature values, except for the (220)-graph. One might draw the conclusion, that the compressed region starts somewhere at 0.7 µm, but since the absolute value of the lattice spacing can be influenced by misalignments of the goniometer, one must be very careful with such a statement. The obvious counter argument for an unstressed region down to 0.7 µm is the measured lattice spacing at $\psi = 0°$ in the (220)-graph which is larger than the theoretical one and which, telling from the curvature, is still growing. The only explanation for such a behaviour would be a tensile stress component perpendicular to the surface.

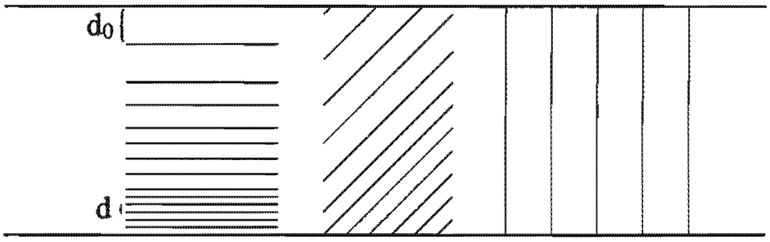

Fig. 7.3: Influence of a σ_{33} stress gradient on the lattice spacing of grains in various orientations

So far, we have explained the curvature in the "*d-sin*$^2\psi$" graphs at small ψ-tilts. The question of why the graphs straighten for bigger ψ-tilts or, in case of the (420)-graph, do not show any curvature at all at high ψ-angles, remains. Considering the development of the penetration depth for higher ψ-tilts as shown in fig. 7.2, we would expect an even stronger curvature at high ψ-angles, because of the greater change in the penetration depth. For a comparison of the penetration depth over the applied ψ-range, vertical, dashed lines were added to fig. 7.2 at the maximum ψ-tilt of the corresponding reflection. We can see now that the (420)-graph with the best linear behaviour covers the widest range of the penetration depth. This contradiction is solved if we keep in mind that with growing ψ-tilt the influence of the stress component perpendicular to the surface is weakening and the one parallel to the surface is gaining influence. Thus the stress gradient is vanishing in grains with a high ψ-tilt as shown in fig. 7.3.

7.2 The stress tensor

In the previous section we have seen that the stress tensor does not contain σ_{X3} shear stresses in our case. On the other hand the stress is not biaxial either and we must take the σ_{33} normal stress component into account. Hence, the stress tensor is given by

$$\begin{pmatrix} \sigma_{11} & \sigma_{12} & 0 \\ \sigma_{12} & \sigma_{22} & 0 \\ 0 & 0 & \sigma_{33} \end{pmatrix} \tag{7.1}$$

Since the curvature and the small ψ-range of the *"d-sin²ψ"* graphs make most of them useless for a meaningful stress determination, we must rely on the (420) reflection. Unfortunately the *"d-sin²ψ"* graph was only measured at three different φ-angles. In the biaxial case this would be sufficient to determine the stress tensor as we have seen in chapter 1, but especially the measurement of the (420) reflection, with the greatest penetration depth and thus the largest σ_{33} component, cannot be assumed biaxial. Hence we cannot use equation (1.19) for the determination of the stress tensor. The slope m_φ of the *"d-sin²ψ"* graph is now dependent on all four stress components:

$$m_\varphi = \frac{1}{2} S_2\, d_0\, (\sigma_{11} \cos^2\varphi + \sigma_{22} \sin^2\varphi - \sigma_{33} + \frac{1}{2} \sigma_{12} \sin 2\varphi) \tag{7.2}$$

This leaves us with the problem of four variables in three equations. But, considering equation (1.17), we can find another relationship between the *"d-sin²ψ"* graph and the stress components: The graphs intercept is given by the normal stresses. However, the big disadvantage of this relationship is, that the intercept is dependent on the absolute measurement of the lattice spacing, which is in return dependent on the absolute peak position, which is susceptible to misalignments. By using the intercept we therefore decrease the precision of the stress components.

With the following set of equations the calculation of the stress tensor as given in (7.1) is possible however:

$$m_{\varphi = 0^\circ} = \frac{1}{2} S_2 \, d_0 \, (\sigma_{11} - \sigma_{33}) \tag{7.3}$$

$$m_{\varphi = 45^\circ} = \frac{1}{2} S_2 \, d_0 \, (\frac{1}{2} \sigma_{11} + \frac{1}{2} \sigma_{22} - \sigma_{33} + \frac{1}{2} \sigma_{12}) \tag{7.4}$$

$$m_{\varphi = 90^\circ} = \frac{1}{2} S_2 \, d_0 \, (\sigma_{22} - \sigma_{33}) \tag{7.5}$$

$$I = \frac{1}{2} S_2 \, d_0 \sigma_{33} + S_1 \, d_0 (\sigma_{11} + \sigma_{22} + \sigma_{33}) + d_0 \tag{7.6}$$

m_φ stands for the slope of the corresponding "*d-sin*$^2\psi$" graph and I for the intercept, which should be independent of the φ-rotation. d_0 is the theoretical lattice spacing and S_1, $\frac{1}{2} S_2$ are the x-ray elastic constants of the {hkl} lattice plane.

For cubic metals S_1 and $\frac{1}{2} S_2$ can be calculated assuming the Reuss model as mentioned in chapter 1 [MÖLL39]:

$$S_1 = s_{12} + \Gamma (s_{11} - s_{12} - \frac{1}{2} s_{44}) \tag{7.7}$$

$$\frac{1}{2} S_2 = s_{11} - s_{12} - 3 \Gamma (s_{11} - s_{12} - \frac{1}{2} s_{44}) \tag{7.8}$$

with

$$\Gamma = \frac{h^2k^2 + k^2l^2 + l^2h^2}{(h^2 + k^2 + l^2)} \tag{7.9}$$

The single crystal elastic compliances s_{xy} for platinum are given in table 5.1. It must be mentioned however that equations (7.7) and (7.8) were derived for the isotropic case and are not necessarily valid for textured materials. The reason why they can be used in this case, is that the "*d-sin*$^2\psi$" curve does not show the oscillatory behaviour of a textured material. We therefore assume that the x-ray elastic constants are not dependent on ψ or φ and that equation (7.7) and (7.8) are valid.

In order to calculate the stress tensor's components the slopes of the "*d-sin*$^2\psi$" curves were calculated with the method of least-squares. Fig. 7.4 shows the "*d-sin*$^2\psi$" graphs of the (420) reflection again including the fitted straight line.

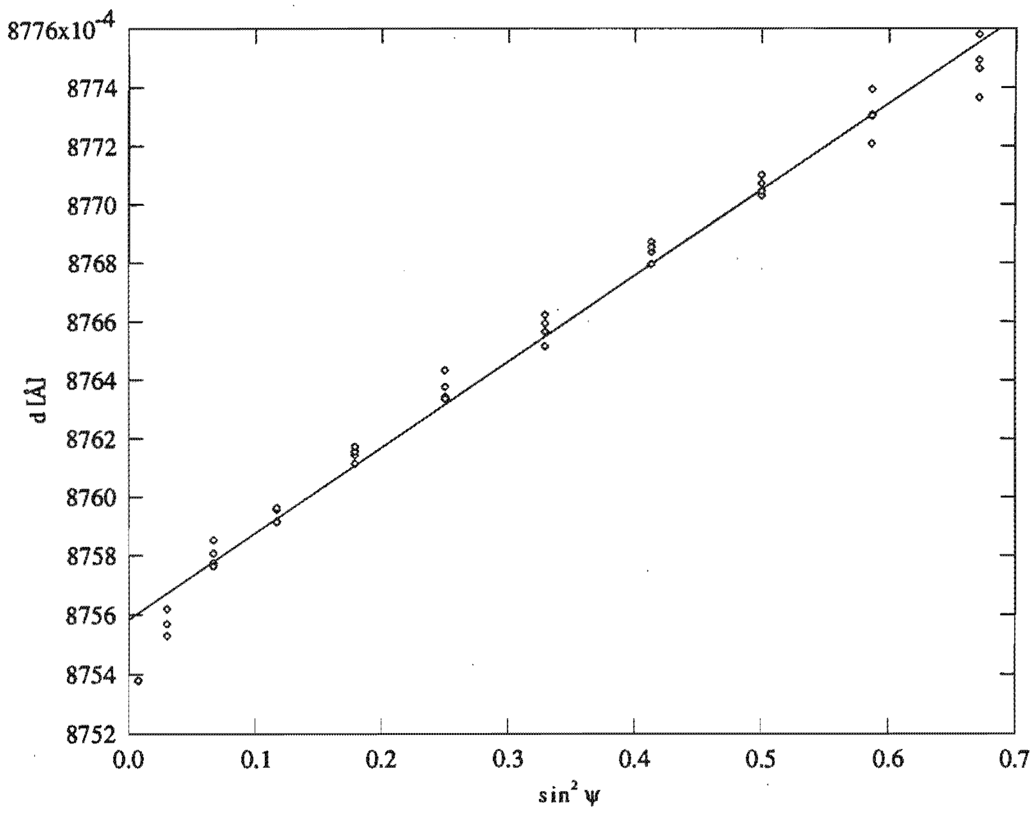

Fig. 7.4a: Combined data from all φ-rotations for intercept determination

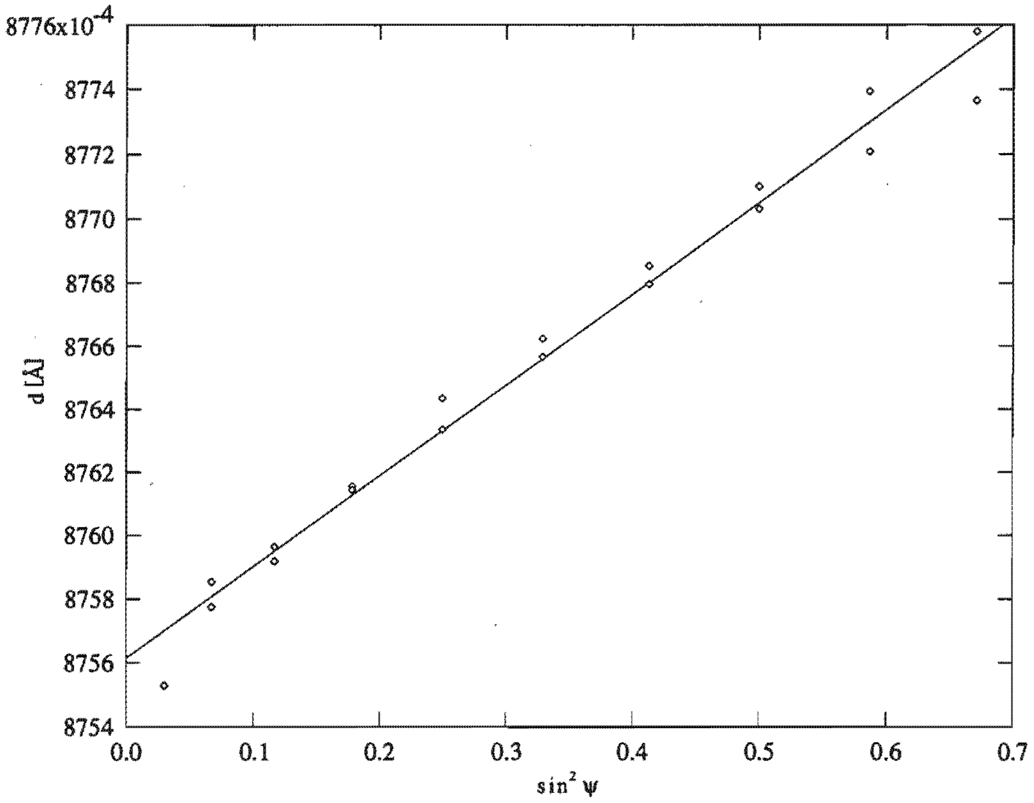

Fig. 7.4b: Least-square-fit for $\varphi = 0°$ and $\varphi = 180°$

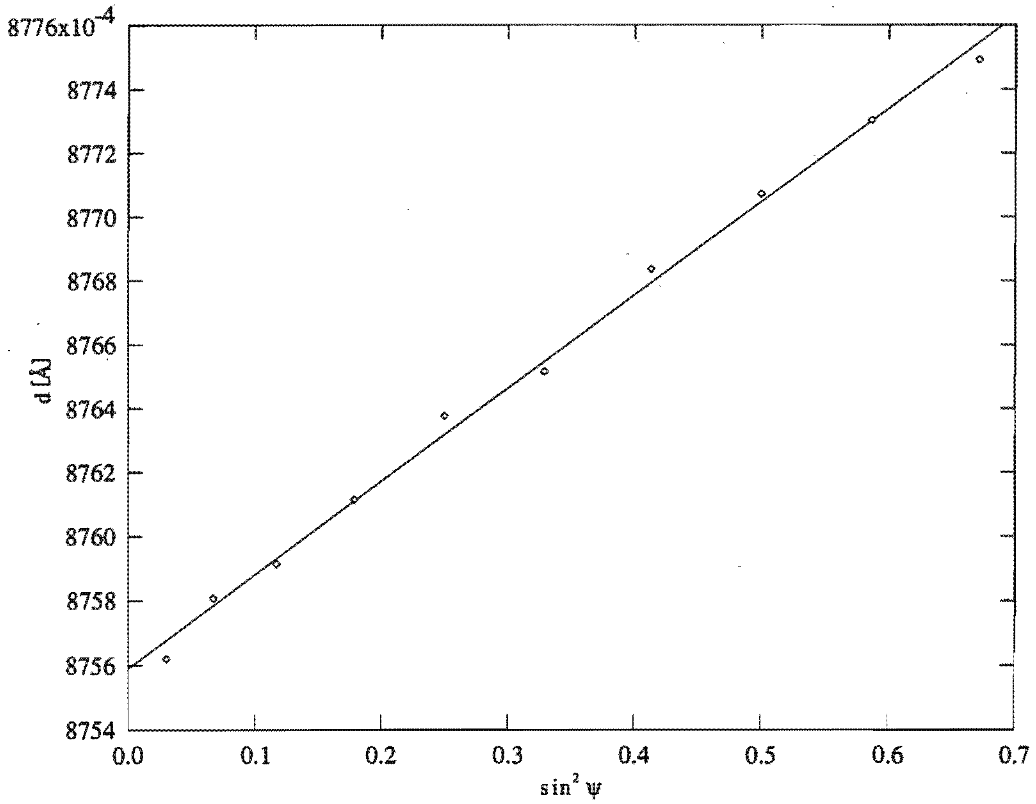

Fig. 7.4c: Least-square-fit for $\varphi = 45°$

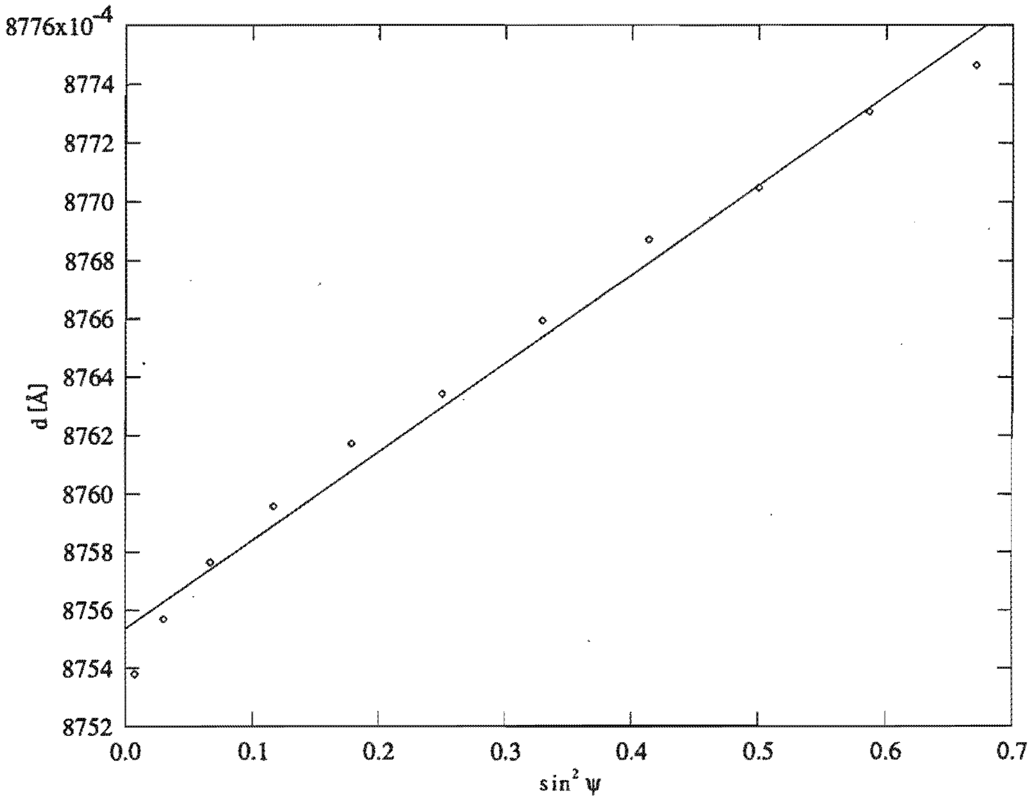

Fig. 7.4d: Least-square-fit for $\varphi = 90°$

Since the intercept I is independent of the φ-angle, its value was obtained by a least-square-fit of the combined data for all φ-rotations as shown in fig. 7.4a. The intercept and the calculated slopes from fig. 7.4b-d including their standard error are given below:

$$\begin{aligned} m_{\varphi = 0°} &= (0.002872 \pm 0.000087)\,\text{Å} \\ m_{\varphi = 45°} &= (0.002916 \pm 0.000062)\,\text{Å} \\ m_{\varphi = 90°} &= (0.00304 \pm 0.00012)\,\text{Å} \\ I &= (0.87558 \pm 0.00002)\,\text{Å} \end{aligned}$$

With the help of the following parameters, equations (7.3) - (7.6) can be solved:

$$\begin{aligned} S_1 &= -2.4592\,\frac{1}{\text{TPa}} \\ \frac{1}{2}S_2 &= 8.5676\,\frac{1}{\text{TPa}} \\ d_0 &= 0.8773\,\text{Å} \end{aligned}$$

Thus, the calculated stress components are:

$$\begin{aligned} \sigma_{11} &= (360 \pm 48)\text{ MPa} \\ \sigma_{22} &= (383 \pm 48)\text{ MPa} \\ \sigma_{33} &= (-22 \pm 46)\text{ MPa} \\ \sigma_{12} &= (-11 \pm 116)\text{ MPa} \end{aligned}$$

We can see that the σ_{11} and σ_{22} components are identical within the errors as one would naturally expect without a distinct direction for the tensile stress. Furthermore, the shear component σ_{12} is almost neglectible which indicates a homogenous expansion and contraction during the annealing cycle. The σ_{33} component on the other hand seems to be very small, if we consider that it could be positive within the standard error. Its value very much depends on the correct determination of the intercept I. As we have mentioned above the intercept is very susceptible to misalignments of the goniometer, because an absolute measurement of the peak position is necessary. Furthermore there is still a curvature at small ψ-tilts in the (420) reflection's *"d-sin²ψ"* graph as we can see in fig. 7.4a. If we assume that there is no stress gradient and therefore no curvature, the straight line would start at a smaller lattice spacing d. The consequence would be a smaller intercept at e.g. $d = 0.8754$ Å. If we do the calculation for the stress components with this new value again, we obtain an astonishing result:

$$\begin{aligned} \sigma_{11} &= (\ 188 \pm\ 48)\ \text{MPa} \\ \sigma_{22} &= (\ 210 \pm\ 48)\ \text{MPa} \\ \sigma_{33} &= (-194 \pm\ 46)\ \text{MPa} \\ \sigma_{12} &= (-\ 11 \pm 116)\ \text{MPa} \end{aligned}$$

The tensile components are still equal within the error, but much smaller compared to the former values. The σ_{33} component on the other hand has grown to the magnitude of the tensile stress components.

We can see that the very strong dependence on the correct intercept makes it very difficult to decide which result is correct and as long as there is a curvature in the "d-$\sin^2\psi$" graph it is actually impossible. The only hint we have is that the σ_{33} component in the first result seems to be too small and that therefore a smaller intercept seems more likely.

8 Outlook

We have seen in the previous chapter that the strong stress gradient perpendicular to the surface makes it very difficult to apply the "*d-*$sin^2\psi$" method. Consequently, the calculated stress components are not very precise. In addition to that, the stress tensor was measured as an avarage over the penetration depth and does not include information about the stress distibution inside the platinum layer. In order to obtain precise measurements it is therefore necessary to use another method for the stress determination. The non-destructive seminumerical method described in [HÄRT93] e.g. is capable of 3-dimensional stress state measurements with depth resolution and would therefore offer a chance to investigate the stress distribution and the stress at the sample's interface. Considering the fact that platinum resistance thermometers are used over a wide temperature range, the stresses at the interface can become critical and damage the layer. In order to prevent large total stresses it would therefore be desirable to keep the intrinsic stresses (see chapter 1) as small as possible . It was shown in [AGAM93] that the intrinsic stress in thin films is dependent on the film thickness and that the stress can vanish completely at a particular thickness. A resistance thermometer with such a thickness of the platinum layer would probably be more durable and could possibly be used over an even wider temperature range.

In conclusion we can say that stress measurements can contribute to improvements in thin layer Pt-Al_2O_3 systems.

References

[AGAM93] S.A. Agamy, *Kerntechnik 58*, 1993, **3**, 188

[AMER72] *American Institute of Physics Handbook*, 1972, 3rd edition, McGraw-Hill Book Company

[ARBL97] J.W. Arblaster, *Platinum Metals Rev.*, 1997, **41**, (1), 12-21

[BEDF96] R.E. Bedford, G. Bonnier, A. Maas and F. Pavese, *Metrologia*, 1996, **33**, 133

[BRAU] *Eigenschaften und Anwendungsmöglichkeiten eines ortsempfindlichen Proportionalzählrohres*, Braun detector manual

[BUNG89] H.J. Bunge and C. Esling (editors), *Advances and Applications of Quantitative Texture Analysis*, 1989, DGM Informationsgesellschaft Oberursel

[CONV92] F. Convert and B. Miege, *Journal of Applied Crystallography*, 1992, **25**, 384

[CULL56] B.D. Cullity, *Elements of X-Ray Diffraction*, 1956, Addisson-Wesley Publishing

[DIET73] H.D. Dietz, *Grundkurs in theoretischer Physik I*, 1973, Bertelsmann Universitätsverlag Düsseldorf

[DOIG81] P. Doig, D. Lansdale and P.E.J. Flewitt, *Journal of Applied Crystallography*, 1981, **14**, 124

[DÖLL76] H. Dölle and V. Hauk, *Härtereitechnische Mitteilungen*, 1976, **31**, 165-168

[DÖLL79] H. Dölle, *J. Appl. Cryst.*, 1979, **12**, 489-501

[EIGE95] B. Eigenmann and E. Macherauch, *Mat.-wiss. u. Werkstofftech.*, 1995, **26**, 199-216

[FANI76] G. Faninger, *Härtereitechnische Mitteilungen*, 1976, **31**, 16

[GMEL74] *Gmelin Handbuch der anorganischen Chemie*, 1974, Teil B1, 8. Auflage, Springer-Verlag Berlin

[HAHN84] H.-G. Hahn in *Elastizitätstheorie*, 1984, Teubner, Stuttgart

[HAND94] *Handbook of Chemistry and Physics*, 1994, 75th edition, The Chemical Rubber Co.

[HÄRT93] M. Härting and G. Fritsch, *Journal of Applied Physics D*, 1993, **26**, 1814

[HÄRT95] M. Härting and P. Willutzki, *Measurements, Sience and Technology*, 1995, **6**, 276

[HAUK82] V. Hauk in *Eigenspannungen und Lastspannungen*, 1982, Karl Hanser Verlag, Wien

[HOUT93] P. Van Houtte and L. De Buyser, *Acta metall. mater.*, 1993, **41**, (2), 323-336

[HUBE92] Huber monochromator manual, 1992

[JCPD97] Powder Diffraction File PCPDFWIN v. 1.30, JCPDS-International Centre for Diffraction Data, 1997

[KAYE66] G.W.C. Kaye and T.H. Laby in *Tables of Physical and Chemical Constants*, 1966, 13th edition, Longmans

[KLUG79] H.P. Klug and L.E. Alexander in *X-ray Diffraction Procedures*, 2nd edition, 1979, John Wiley & Sons, New York

[KRÖN58] E. Kröner, *Z. Phys.*, 1958, **151**, 504

[KUSS87] K.Kussmaul, W. Guth and R. Meyer, *Shot Peening, Science-Technology-Application*, 1987, DGM Informationsgesellschaft Oberursel, 335

[MACH58] E. Macherauch and P. Müller, *Arch. Eisenhüttenwesen*, 1958, **29**, 257-260

[MACH61] E. Macherauch and P. Müller, *Z. f. angew. Physik*, 1961, **13**, 305-312

[MACH87] E. Macherauch and K.H. Kloos in *Residual Stresses in Science and Technology (Proc. Int. Conf. on Residual Stresses, Garmisch Patenkirchen 1986)*, (edited by

E. Machereauch and V. Hauk), 1987, DGM Informationsgesellschaft Oberursel

[MARI75] R.H. Marion and J.B. Cohen, *Journal of Applied Crystallography*, 1975, **8**, 430

[MARI76] R.H. Marion and J.B. Cohen, *Advances in X-Ray Analysis*, 1976, **20**, 355-367

[MÖLL39] H. Möller and G. Martin, *Mitt. K.-Wilhelm-Inst. Eisenforsch.*, 1939, **21**, 261

[NOYA87] I.C. Noyan and J.B. Cohen, *Residual Stress*, 1987, Springer Verlag

[NOYA91] I.C. Noyan and C.C. Goldsmith, *Advances in X-Ray Analysis*, 1991, **34**, 587-600

[NYE57] J.F. Nye, *Physical Properties of Crystals*, 1957, Oxford University Press

[PREC88] U. Preckel, *Eigenspannungen, rechnergestützte Bestimmung in Umformteilen*, 1988, Verlag TÜV Rheinland, Köln

[REUS29] A. Reuss, *Z. angew. Math. Mech.*, 1929, **9**, 49

[SERR88] W. Serrugs, P. Van Houtte and E. Aernoudt, *Journal of Strain Analysis*, 1988, **23**, 155

[VOIG28] W. Voigt, *Lehrbuch der Kristallphysik*, 1928, Teubner Berlin

[WOLF76a] U. Wolfstieg and E. Macherauch, *Härtereitechnische Mitteilungen*, 1976, **31**, 2

[WOLF76b] U. Wolfstieg, *Härtereitechnische Mitteilungen*, 1976, **31**, 19

Appendix

(220)

$\varphi = 0°$

Parameters:

X-ray tube voltage: 40 kV

X-ray tube current: 25 mA

Detector voltage: 3.67 kV

Detector-gas pressure: 10 bar

$2\theta_{\text{theo}} = 67.4541°$ (Cu-Kα_1)

$2\theta_{\text{theo}} = 67.6443°$ (Cu-Kα_2)

Data for Cu-Kα_2 peak:

ψ-tilt [°]	Peak Position [°]	FWHM[1] [°]	elapsed measuring time
0	67.6127	0.1673	12h
5	67.5736	0.1643	6h
10	67.5259	0.2796	14.83h
15	67.4895	0.1615	4.25h
20	67.4530	0.1943	3h
26.26	67.4223	0.1631	2h
30	67.4075	0.1844	2h

---

[1] Full Width Half Maximum

(222)

$\varphi = 0°$

Parameters:

X-ray tube voltage: 40 kV X-ray tube current: 25 mA

Detector voltage: 3.67 kV Detector-gas pressure: 10 bar

$2\theta_{theo} = 85.7121°$ (Cu-Kα_1) $2\theta_{theo} = 85.9767°$ (Cu-Kα_2)

Data for Cu-Kα_2 peak:

ψ-tilt [°]	Peak Position [°]	FWHM [°]	elapsed measuring time
0	86.2139	0.1107	1h
5	86.1723	0.1090	1h
10	86.1328	0.1120	1h
15	86.0946	0.1165	1h
20	86.0565	0.1171	1h
25	86.0192	0.1760	6.5h

$\varphi = 180°$

Parameters:

X-ray tube voltage: 40 kV X-ray tube current: 25 mA

Detector voltage: 3.67 kV Detector-gas pressure: 10 bar

$2\theta_{theo} = 85.7121°$ (Cu-Kα_1) $2\theta_{theo} = 85.9767°$ (Cu-Kα_2)

Data for Cu-Kα_2 peak:

ψ-tilt [°]	Peak Position [°]	FWHM [°]	elapsed measuring time
0	86.1948	0.1148	1h
5	86.1562	0.1060	1h
10	86.1196	0.1146	1h
15	86.0833	0.1292	1h
20	86.0315	0.1781	1h
25	not measurable	----	8h

$\varphi = 90°$

Parameters:

X-ray tube voltage: 40 kV X-ray tube current: 25 mA

Detector voltage: 3.67 kV Detector-gas pressure: 9.8 bar

$2\theta_{\text{theo}} = 85.7121°$ (Cu-Kα_1) $2\theta_{\text{theo}} = 85.9767°$ (Cu-Kα_2)

Data for Cu-Kα_2 peak:

ψ-tilt [°]	Peak Position [°]	FWHM [°]	elapsed measuring time
0	86.2064	0.1252	2h
5	86.1715	0.1240	2h
10	86.1385	0.1086	2h
15	86.1064	0.1200	2h
20	86.0678	0.1085	10h
25	86.0169	0.0558	4.86h

$\varphi = 45°$

Parameters:

X-ray tube voltage: 40 kV X-ray tube current: 25 mA

Detector voltage: 3.67 kV Detector-gas pressure: 9.8 bar

$2\theta_{\text{theo}} = 85.7121°$ (Cu-Kα_1) $2\theta_{\text{theo}} = 85.9767°$ (Cu-Kα_2)

Data for Cu-Kα_2 peak:

ψ-tilt [°]	Peak Position [°]	FWHM [°]	elapsed measuring time
0	86.2675	0.1235	1h
5	86.2385	0.1177	1h
10	86.1974	0.1280	1h
15	86.1609	0.1329	0.5h
20	86.1748	0.1915	2h
25	86.0215	0.0984	14h

(311)

φ = 0°

Parameters:

X-ray tube voltage: 40 kV X-ray tube current: 25 mA

Detector voltage: 3.67 kV Detector-gas pressure: 10 bar

$2\theta_{\text{theo}} = 81.2861°$ (Cu-Kα_1) $2\theta_{\text{theo}} = 81.5309°$ (Cu-Kα_2)

Data for Cu-Kα_2 peak:

ψ-tilt [°]	Peak Position [°]	FWHM [°]	elapsed measuring time
0	81.7252	0.1125	14h
5	81.6908	0.1332	14.5h
10	81.6448	0.1405	12h
15	81.6104	0.1510	4h
20	81.5691	0.1430	3h
25	81.5241	0.1591	3h
30	81.4695	0.2192	4h
35	81.4534	0.1857	3h

φ = 180°

Parameters:

X-ray tube voltage: 40 kV X-ray tube current: 25 mA

Detector voltage: 3.67 kV Detector-gas pressure: 10 bar

$2\theta_{\text{theo}} = 81.2861°$ (Cu-Kα_1) $2\theta_{\text{theo}} = 81.5309°$ (Cu-Kα_2)

Data for Cu-Kα_2 peak:

ψ-tilt [°]	Peak Position [°]	FWHM [°]	elapsed measuring time
0	81.7273	0.1100	14h
5	81.6933	0.1264	4h
10	81.6486	0.1631	12h
15	81.6039	0.1259	4h
20	81.5745	0.1193	3h
25	81.5530	0.1774	2.7h
30	81.5081	0.1959	3h
35	81.4476	0.3102	3h

$\varphi = 90°$

Parameters:

X-ray tube voltage: 40 kV X-ray tube current: 25 mA

Detector voltage: 3.67 kV Detector-gas pressure: 10 bar

$2\theta_{theo} = 81.2861°$ (Cu-Kα_1) $2\theta_{theo} = 81.5309°$ (Cu-Kα_2)

Data for Cu-Kα_2 peak:

ψ-tilt [°]	Peak Position [°]	FWHM [°]	elapsed measuring time
0	81.7348	0.1493	11h
5	81.6955	0.1445	3.35h
10	81.6480	0.1504	2h
15	81.6155	0.1602	2h
20	81.5737	0.2016	2h
25	81.5297	0.2053	1.7h
30	81.4958	0.3749	2h
35	81.4565	0.2718	2h

$\varphi = 45°$

Parameters:

X-ray tube voltage: 40 kV X-ray tube current: 25 mA

Detector voltage: 3.67 kV Detector-gas pressure: 10 bar

$2\theta_{theo} = 81.2861°$ (Cu-Kα_1) $2\theta_{theo} = 81.5309°$ (Cu-Kα_2)

Data for Cu-Kα_2 peak:

ψ-tilt [°]	Peak Position [°]	FWHM [°]	elapsed measuring time
0	81.7596	0.1639	3h
5	81.7233	0.1362	3h
10	overlapping peak	----	12h
15	81.7148	0.1528	2h
20	81.5975	0.1957	1h
25	81.5641	0.1779	1h
30	81.5216	0.3130	1h
35	81.4955	0.3347	1h

(420)

φ = 0°

Parameters:

X-ray tube voltage: 40 kV
X-ray tube current: 25 mA
Detector voltage: 3.67 kV
Detector-gas pressure: 10 bar
$2\theta_{theo} = 122.8070°$ (Cu-Kα_1)
$2\theta_{theo} = 123.3318°$ (Cu-Kα_2)

Data for Cu-Kα_2 peak:

ψ-tilt [°]	Peak Position [°]	FWHM [°]	elapsed measuring time
10	overlapping peak	----	12h
15	123.684	0.2720	12h
20	123.668	0.3026	2h
25	123.613	0.2154	2h
30	123.542	0.2458	2h
35	123.496	0.2470	2h
40	123.440	0.2466	1h
45	123.380	0.2321	1h
50	123.309	0.2641	2h
55	123.264	0.2436	2h

φ = 180°

Parameters:

X-ray tube voltage: 40 kV
X-ray tube current: 25 mA
Detector voltage: 3.67 kV
Detector-gas pressure: 10 bar
$2\theta_{theo} = 122.8070°$ (Cu-Kα_1)
$2\theta_{theo} = 123.3318°$ (Cu-Kα_2)

Data for Cu-Kα_2 peak:

ψ-tilt [°]	Peak Position [°]	FWHM [°]	elapsed measuring time
10	123.763	0.2120	12h
15	123.703	0.2141	12h
20	123.657	0.1763	2h
25	123.610	0.1852	2h
30	123.566	0.2715	2h
35	123.510	0.2229	2h
40	123.454	0.2368	1h
45	123.397	0.2755	1h
50	123.354	0.2695	2h
55	123.316	0.3071	3h

$\varphi = 90°$

Parameters:

X-ray tube voltage: 40 kV X-ray tube current: 25 mA

Detector voltage: 3.67 kV Detector-gas pressure: 10 bar

$2\theta_{theo} = 122.8070°$ (Cu-Kα_1) $2\theta_{theo} = 123.3318°$ (Cu-Kα_2)

Data for Cu-Kα_2 peak:

ψ-tilt [°]	Peak Position [°]	FWHM [°]	elapsed measuring time
5	123.7998	0.3184	1h
10	123.7531	0.2873	12h
15	123.7056	0.3175	12h
20	123.6584	0.2392	2h
25	123.6059	0.2671	2h
30	123.5644	0.2203	2h
35	123.5031	0.2653	2h
40	123.4356	0.2578	2h
45	123.3931	0.2846	1h
50	123.3302	0.2604	1h
55	123.2920	0.2712	2h

$\varphi = 45°$

Parameters:

X-ray tube voltage: 40 kV X-ray tube current: 25 mA

Detector voltage: 3.67 kV Detector-gas pressure: 10 bar

$2\theta_{theo} = 122.8070°$ (Cu-Kα_1) $2\theta_{theo} = 123.3318°$ (Cu-Kα_2)

Data for Cu-Kα_2 peak:

ψ-tilt [°]	Peak Position [°]	FWHM [°]	elapsed measuring time
10	123.741	0.2997	11h
15	123.659	0.2471	11h
20	123.669	0.2804	2h
25	123.620	0.2280	10h
30	123.556	0.2191	1h
35	123.522	0.2498	1h
40	123.444	0.2509	1h
45	123.387	0.2673	1h
50	123.331	0.2687	1h
55	123.285	0.6016	2h

Acknowledgements

I wish to express my thanks to my supervisor Dr. M. Härting for providing the motivation for this thesis and for the continous assistance throughout the proceeding of the work.

I extend my gratitude to Dr. M. Hempel who was always helpful and gave a lot of intellectual support. It was a pleasure to work with her.

Many thanks also to Dr. D.T. Britton for plenty of fruitful discussions.